COORDINATED CONTROL OF RENEWABLE ENERGY POWER GENERATORS IN MICROGRIDS

JUN WEI CHAI

PhD

The Hong Kong Polytechnic University

2024

The Hong Kong Polytechnic University

Department of Electrical and Electronic Engineering

Coordinated Control of Renewable Energy Power Generators in Microgrids

Jun Wei Chai

A thesis submitted in partial fulfillment of the requirements for the degree of Doctor of Philosophy

May 2024

CERTIFICATE OF ORIGINALITY

I hereby declare that this thesis is my own work and that, to the best of my knowledge and belief, it reproduces no material previously published or written, nor material that has been accepted for the award of any other degree or diploma, except where due acknowledgment has been made in the text.

Signature: _________________________

Name of Student: _______ Jun Wei_Chai_______

Abstract

Microgrids, offering a feasible solution for assimilating a diverse array of renewable energies, obtain widespread implementation in recent decades. To guarantee the normal operation of microgrids, the elaborate control strategies are necessitated. Although the existing methods can yield good performance, some challenges (e.g., circulating currents among distributed generators (DGs) and the parallel converters) still exist and higher system performances (e.g., faster system dynamics and less communication burden among DGs) are widely anticipated. To solve the above issues, advanced decentralized and distributed control methods are investigated from the converter level and the microgrid level, respectively, in this thesis.

Firstly, the common ground circulating currents emerge when grounding faults occur in photovoltaic (PV) power plants, which undermine the system's stability. In response, utilizing the equivalent model of circulating currents (CCs), this thesis devises a decentralized strategy to diminish these CCs. Moreover, to preserve the stable currents and DC-link voltages during the transience of grounding faults, a delicate control scheme is introduced, utilizing a three-level PV interfacing converter to curb the surges in currents and voltages. Experiments validate the effectiveness of these methods.

Secondly, single-phase three-level neutral-point clamped inverters have been extensively used to interface the renewable energy and the grid. To accommodate high-power scenarios, multiple inverters are typically connected in parallel, which will cause circulating currents (CCs) when the hardware parameters are asymmetric, threatening the reliability of the system. Aiming at this problem, this thesis proposed a decentralized strategy for CC suppression, leveraging an enhanced 3LNPCI topology with expanded modulation freedoms. This strategy can concurrently address CC suppression and achieve the desired current sharing. The efficacy of this strategy is substantiated through experiments.

Thirdly, to meet the heightened performance criteria set for DC microgrids, a distributed fixed-time secondary control strategy is proposed to simultaneously regulate DC bus voltage and ensure proportional current distribution among DGs within a fixed time, demonstrating a fast dynamic response. Besides, only one variable needs to be transmitted in the proposed control strategy, significantly reducing the communication traffic. Moreover, this method can eliminate the need for bus voltage monitoring, which simplifies the system architecture and enhances reliability. Simulations tests validate the viability of this scheme.

Lastly, to further reduce data exchanges between DGs within DC microgrids, this thesis designs an event-triggered fixed-time secondary control strategy. Besides the ability to concurrently manage DC bus voltage and achieve proportional current distribution among DGs within a fixed time, by leveraging the event-triggered communication protocol, each DG is required to update its status to adjacent DGs only upon meeting predefined triggering conditions, thereby substantially reducing communication overhead. Experimental tests are carried out to verify the efficacy of this strategy.

In summary, this thesis proposes a series of control strategies to address some existing challenges in the large-scale application of renewable energy sources, and satisfactory results have been confirmed through both simulation and experimental verifications. This study lays the foundation to some extent for the efficient utilization of renewable energy sources and achieving decarbonization goals.

Key words: PV grounding faults, Circulating current suppression, DC microgrids, Fixed-time control, Event-triggered control, Renewable power generators.

Publications Arising from the Thesis

Journal Papers:

[1] J. Chai, M. Wang, Y. He, Z. Li, Z. Xu and S. Li, "Decentralized Suppression Strategy of Common Ground Circulating Current Caused by Grounding Fault in PV Modules in Single-Phase PV Grid-Connected Systems," *IEEE Journal on Emerging and Selected Topics in Circuits and Systems*, vol. 12, no. 1, pp. 220-231, March 2022.

[2] J. Chai, M. Wang, Z. Li and Z. Xu, "Improved Super-Twisting Sliding Mode Control for Single-Phase T-Type Three-Level Converters Based on Fixed-Time Extended State Observer," *IEEE Transactions on Transportation Electrification*, doi: 10.1109/TTE.2023.3325803. (Early access)

[3] J. Chai, M. Wang, Z. Xu and K. W. E. Cheng, "Suppression of Circulating Currents Among IPOP Single-Phase Three-Level Inverters," *IEEE Transactions on Industrial Electronics*, , vol. 71, no. 9, pp. 10533-10545, Sept. 2024.

[4] J. Chai, M. Wang and Z. Xu, "A Distributed Event-Triggered Fixed-Time Secondary Control for DC Microgrids Without Continuous Signal Transmission," *IEEE Journal of Emerging and Selected Topics in Power Electronics*, doi: 10.1109/JESTPE.2024.3435755. [Early access]

[5] J. Chai, M. Wang and Z. Xu, “A Two Stage Distributed Event-Triggered Fixed-Time Secondary Control for Renewable DC Microgrids with Inherent Actuator Fault Tolerant Capability”, *Journal of Modern Power Systems and Clean Energy*. [Under review]

Conference Papers:

[6] J. Chai, X. Lyu, M. Wang and Z. Xu, "Distributed Fixed-Time Secondary Control for DC Microgrid with Less Information Exchange," *2023 8th International Conference on Power and Renewable Energy (ICPRE)*, Shanghai, China, 2023, pp. 652-657. (Best Student Paper)

[7] J. Chai, M. Wang and Z. Xu, "Distributed Fixed-Time Secondary Control for DC Microgrids," *2024 IEEE Applied Power Electronics Conference and Exposition (APEC)*, Long Beach, CA, USA, 2024, pp. 1614-1618.

Acknowledgments

First, I would like to express my sincere appreciation to my supervisors, Prof. Zhao Xu and Dr. Minghao Wang. Prof. Xu's extensive expertise and fervent passion for research have left a lasting impression on me. His inventive mindset continually energizes me, and his unwavering dedication and an optimistic attitude propels me to surmount obstacles. His support and encouragement have been instrumental in expanding my research horizons and fostering a spirit of continual exploration. Dr. Wang has offered me a lot of help and support throughout my Ph.D. journey. His fervor for academic exploration and keen analytical mindset deeply influence me. He can always pinpoint central concerns and suggest novel approaches. Engaging in discussion with him is consistently thought-provoking and energizing. Prof. Xu and Dr. Wang generously impart their knowledge and perspectives on research, work, and life, providing me with lifelong benefits. I feel incredibly lucky and honored to undertake my Ph.D. studies under the supervision of Prof. Xu and Dr. Wang.

I would like to express sincere gratitude to my friends and peers for their encouragement, accompany and support. Thanks to the PolyU smart microgrid group members.

Last but not least, I would like to express my profound gratitude to my beloved parents for their most selfless and unconditional love. My deepest thanks go to my elder brother for his steadfast support throughout my study journey. I also extend my deep love to my dear wife, Dr. Mufang Xie. We have supported each other through difficult times, and experienced numerous delightful moments side by side. I will forever be grateful for their understanding, accompany and love in my life.

Table of Contents

Chapter 1 Introduction

1.1 Background and Motivation

The utilization of renewable energy, characterized by its limitless availability and non-polluting nature, presents a viable solution for addressing the dual challenges of environmental degradation and energy scarcity [1]–[3]. This has catalyzed a global surge in the adoption of renewable energy sources [4], [5]. Marking a significant phase in the energy sector, the 21st century has witnessed a rapid evolution in renewable energy-based power generation, leading to a notable increase in its contribution to the overall power mix, as illustrated in Fig. 1-1. Particularly, solar and wind energy have seen remarkable growth rates and has accounted for 58% of global renewable generation capacity at the end of 2022, as depicted in Fig. 1-2 and Fig. 1-3, respectively [6]. Projections indicate that by the mid-21st century, renewable sources could contribute approximately 80% to the global primary energy mix [7], signaling a profound shift from the conventional thermal power-dominated systems to ones heavily reliant on renewable energy sources [8].

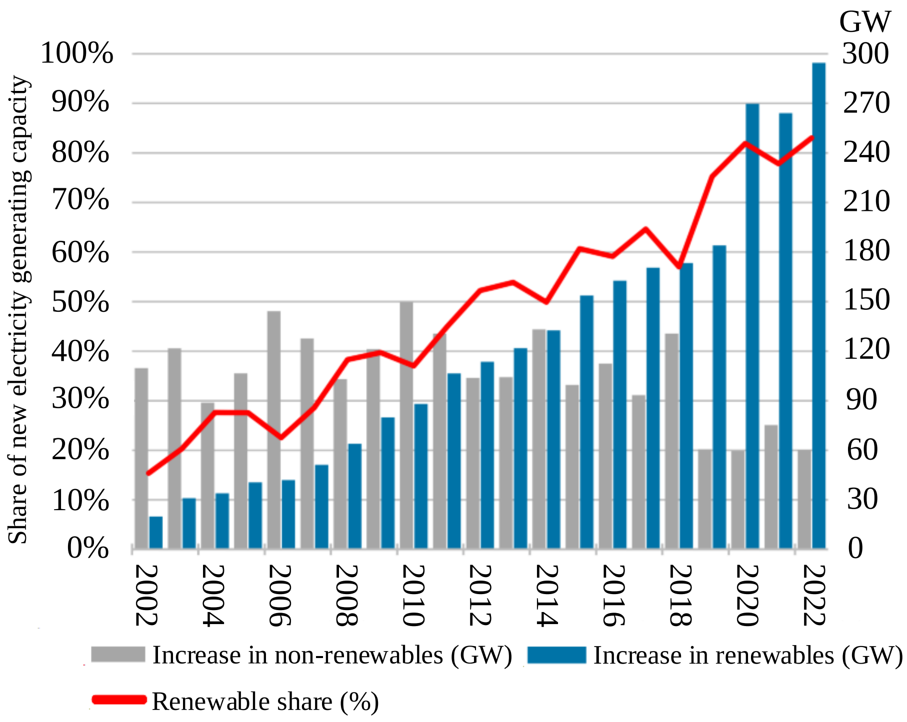

Fig. 1-1. Renewable share of annual power capacity expansion from 2002 to 2022 [6].

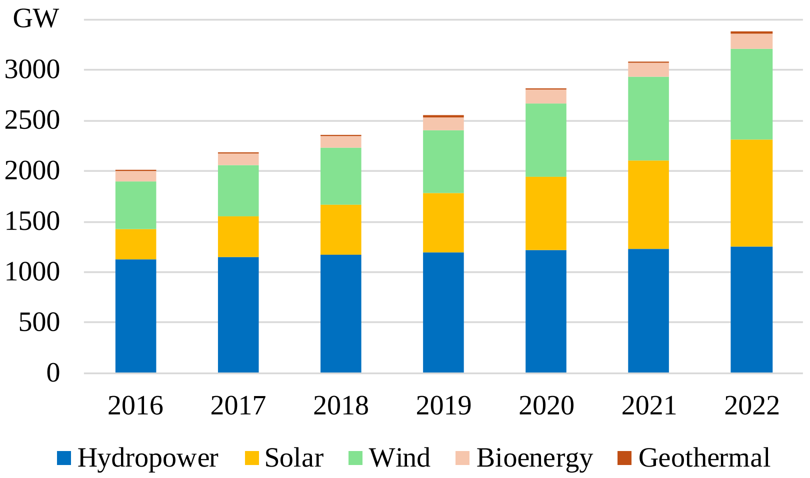

Fig. 1-2. Renewable power capacity growth during 2016-2022 [6].

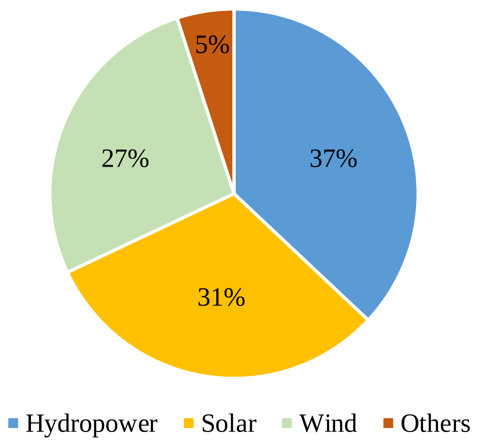

Fig. 1-3. Renewable generation capacity by energy source at the end of 2022 [6].

Due to the intermittent nature of renewable energy sources [9], their large-scale and disorderly integration can impact the power balance and stability of the system [10], [11], preventing the true realization of an environmentally friendly power system [12], [13]. In response to this, microgrids have been proposed and widely applied to accommodate the ever-increasing renewable energy [14], [15]. The microgrid system is a compact, localized energy infrastructure. It encompasses an array of renewable energy-based distributed generators (DGs), energy storage devices, and proximal loads. Microgrids essentially can operate autonomously from the traditional centralized grid [16] or in conjunction with it [17]. This configuration can not only facilitate the provision of clean energy but also enhance the overall dependability of the energy system [18], [19]. Consequently, microgrids have gained increasing attention in recent decades.

On the other hand, with the development of microgrids, a series of issues related to microgrids have also emerged. Firstly, the incorporation of a substantial proportion of renewable energy-based DGs makes the microgrid evolve into a complex and intricately organized system characterized by their distributed and modular nature [20], [21], leading to complicated power flows. As one of the representations of intricate power flows, circulating currents among DGs and parallel converters have significant detrimental effects, such as distorting output currents, reducing system efficiency and even resulting in system failure. Particularly considering the various faults in renewable energy sources (e.g., the PV grounding faults, etc.) and hardware manufacturing tolerances in DGs, large circulating currents will occur, which compromise the system stability. Secondly, numerous DGs adopt power converters as the output interfaces, the significant nonlinearity of these converters, coupled with the diverse dynamic responses of different DGs, complicates ensuring the stability and state convergence of the entire microgrid [22], [23]. These facts impose significant challenges for microgrids to achieve high energy efficiency and high reliability. Therefore, the investigation into novel control strategies for converters and microgrids, which are optimized for extensive integration of renewable energy sources and system safety and reliability, holds substantial importance. Traditionally, a hierarchical control method is applied to microgrid systems, which can be divided into three layers, i.e., primary, secondary and tertiary control. Although the reported methodologies yield satisfactory outcomes [24]–[27], challenges still exist. *Regarding the issue of circulating currents*, those caused by PV grounding faults and hardware manufacturing tolerances of converters have not been well addressed. *For the issue of microgrid stability*, strong robust stability and enhanced system performance of microgrids, including accelerated system dynamics and reduced communication overhead among DGs in the microgrids, still require further improvement. To address these issues and meeting these advanced performance criteria, this thesis puts forth innovative decentralized and distributed control strategies from the converter level and the microgrid level, respectively.

1.2 Literature Review

Focusing on the problems of circulating current suppression and the advanced microgrid performance requirements, cutting-edge literatures regarding the control of converters and microgrids are reviewed in this part.

1.2.1 The Circulating Currents Caused by Grounding Fault in PV Modules

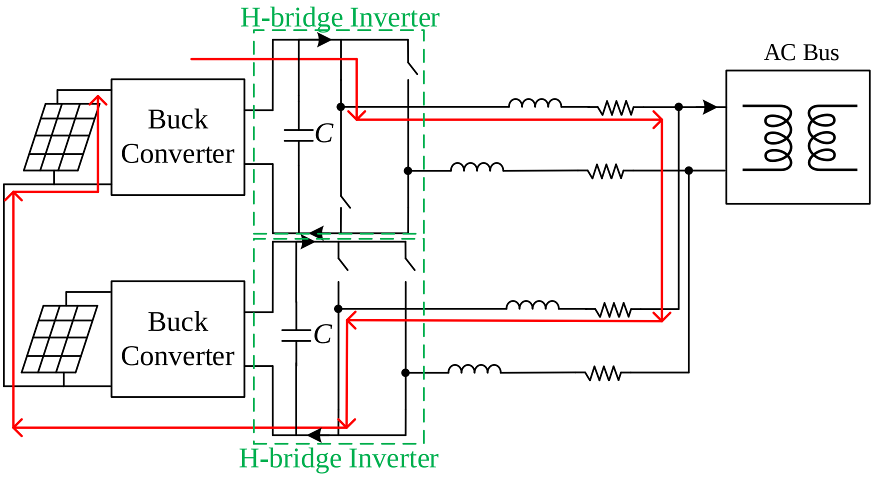

Fig. 1-4. The two-stage PV inverter configuration comprising a standard buck converter in the first stage and an H-bridge inverter in the second stage.

Solar energy, recognized for its environmental friendliness and substantial availability, has been undergoing significant growth and evolution in the realm of photovoltaic (PV) generation systems over recent years [28]–[30]. PV generation systems, particularly when integrated with the utility grid, play a crucial role in transitioning away from carbon-intensive energy sources [31], [32]. Among the various technologies employed in grid-connected PV systems, the cascaded two-stage PV inverter setup is particularly noteworthy [33], [34]. This configuration, favored for its adaptability and superior efficiency in tracking the maximum power point (MPPT) [35], [36], involves two stages: initially, a DC/DC PV converter functions in the first stage, followed by a DC/AC grid-tied inverter in the second stage. The initial stage often employs either buck, boost, or buck-boost converters, each offering distinct advantages in the energy conversion process [37]–[41]. For the second DC-AC conversion stage, the H-bridge inverter is usually employed. The examined single-phase PV system linked to the grid in the thesis, can be depicted in Fig. 1-4.

Many existing PV power systems are prone to a range of malfunctions, particularly within the PV arrays, electrical connections, and grid interfaces. These malfunctions encompass line-to-line faults [42]–[44], hot-spot faults [45], [46], arc faults [47]–[49], open-circuit faults [50], and grounding faults [51], [52], among others. The prevalence of grounding faults in PV modules is notably higher in vast solar farms due to the intricate configuration of series and parallel connections combined with the deterioration of insulation over time, posing significant risks in large-scale PV operations [53]. Such faults induce circulating currents across the common ground through low-resistance pathways and the electrical apparatus, leading to increased stress on switches, compromised grid power quality, and potential threats to overall system stability, thereby highlighting the necessity for preemptive measures.

Grounding faults exert profound adverse effects on the reliability of equipment and the stability of systems. Documented in [54], grounding faults within PV modules precipitate overvoltage and overcurrent conditions, detrimentally impacting electrical and electronic components and undermining safety measures. Furthermore, [55] highlights that overcurrent resulting from grounding faults can generate excessive heat, thereby deteriorating wire insulation and elevating the risk of fires. Additionally, research presented in [56] elucidates that grounding faults trigger substantial potential differences between compromised strings and their operational counterparts. This discrepancy necessitates the faulty string to elevate its output voltage to align with that of the functioning strings, inadvertently converting it into a passive load. This scenario amplifies power dissipation and disrupts the seamless operation of adjacent PV strings. A novel fault detection approach leveraging a fractional-order color relation classifier is introduced in [57], demonstrating notable efficacy in pinpointing defective components. This technique is distinguished by its real-time application suitability and adaptability in fault identification tasks. Furthermore, [58] advocates a robust and efficient methodology for fault localization, employing differential voltage measurement across PV modules in neighboring strings. Additionally, [59] presents a fault detection algorithm based on spread spectrum time-domain reflectometry (SSTDR), noteworthy for its operational viability independent of solar irradiation. Collectively, these methodologies primarily concentrate on identifying and segregating malfunctioning PV modules to safeguard system integrity [57]–[61]. Despite their contributions, these strategies exhibit certain limitations. Primarily, the precision of fault detection algorithms is compromised by parasitic elements and measurement inaccuracies within the PV framework, potentially leading to incomplete fault identification and jeopardizing system stability. Moreover, the mere isolation of faulty components escalates power losses, undermining both the economic and operational efficiency of the PV system.

Therefore, there is a critical need for a reliable and economical approach to tackle the issues facing grounding faults within single-phase PV grid-connected systems.

1.2.2 The Suppression of Circulating Currents among IPOP Single-Phase Three-level Inverters for Renewable Energy Power Generation Systems

For the better integration of distributed renewable power generators, single-phase inverters have been extensively utilized to accommodating DC renewables (e.g., PV) into the AC utility grids [62], [63]. Among them, single-phase three-level inverters are garnering significant interest due to their suitability for high-voltage applications, high efficiency, and low harmonic distortion [64]. The half-bridge configuration, particularly the neutral-point clamped (NPC) inverter, stands out for its ability to effectively mitigate common-mode currents, making it an attractive choice for PV systems [65], [66]. Typically, these inverters employ an input-parallel-output-parallel (IPOP) architecture to achieve both a high power rating and modularity. However, this configuration is prone to circulating currents (CCs) due to asymmetries in hardware parameters, such as manufacturing tolerances. These circulating currents can increase the stress on active components, distort output currents, diminish system efficiency, and, in severe cases, lead to system failure [67], [68].

With the escalating incorporation of distributed renewable energy into the grid and the adverse impacts of CCs, a lot of studies have been undertaken to mitigate these effects. Significant progress has been made in addressing CCs within IPOP three-phase level inverters (3LIs), with a particular focus on eradicating zero-sequence circulating currents (ZSCCs). These methodologies fall into two categories: modulation strategies and control strategies. In the realm of modulation techniques, a foundational model for analyzing ZSCCs in IPOP 3LIs is established in [69], facilitating the enhancement of the current waveform and the reduction of ZSCCs by modulating the duration of minor vectors in space vector modulation through a deadbeat control approach. Additionally, it is demonstrated in [70] that disparities in zero-sequence voltage (ZSV) among IPOP 3LIs are principal contributors to ZSCCs, prompting the proposal of an advanced modulation technique to lessen ZSV discrepancies and eradicate ZSCCs. Conversely, in the sphere of control strategies, a model predictive control (MPC) framework utilizing virtual voltage vectors is devised in [71] to diminish ZSCCs in IPOP 3LIs. An examination of ZSCCs pathways in these inverters yields an equivalent ZSCCs model in [72], paving the way for the application of a zero-sequence current control loop to suppress ZSCCs. Further, a novel ZSCCs equivalent model is introduced in [73], alongside a more feasible controller based on this model, enhancing hot-swap functionality. However, these control-oriented approaches require accurate and extensive parameters from multiple parallel inverters, which may impede system scalability and modular deployment.

While the modulation and control strategies previously outlined offer substantial reductions in CCs within IPOP three-phase 3LIs, their direct application to single-phase inverters is impeded by the intrinsic differences in the nature of CCs between these two types of inverters. The CCs encountered in IPOP three-phase 3LIs are distinct in origin and characteristics from those present in single-phase inverters, necessitating tailored approaches for effective mitigation in the latter.

In the domain of CC suppression for IPOP single-phase inverters, research has predominantly focused on two-level inverters. A simplified model for CCs in two IPOP single-phase converters is introduced [74], alongside a novel pulse width modulation (PWM) strategy-based control method for CC mitigation. This approach is further improved in subsequent studies [75], [76], where the impact of load variations is incorporated into the CC model, and a more sophisticated PWM technique is devised by simultaneously modulating two cascaded converters to eliminate CCs. However, the centralized nature of these control strategies [74]–[76] limits their applicability in modular systems. Further exploration into the optimal operational states of parallel inverters in [77] reveals the absence of CCs under uniform modulation conditions. Yet, achieving such uniformity is challenging in practical scenarios, particularly with the failure and subsequent replacement of converters. A detailed analysis of CCs leads to the categorization into common-mode and differential-mode CCs in [78], with centralized compensators designed for reduction. The paths and generation mechanisms of CCs among IPOP H-bridge inverters are delineated [79], proposing a simplified PWM method with switching constraints to mitigate CCs. These methods, primarily tailored for two-level inverters, encounter limitations when applied to IPOP single-phase three-level inverters due to topological constraints and the necessity for specific modulation schemes. Recent advancements in [80] in this area include the development of an accurate mathematical model for CCs among parallel inverters, incorporating the effects of asymmetric filter inductors. This model underpins the design of a deadbeat controller that suppresses CCs through voltage offset injection, representing a significant stride forward in addressing CCs in IPOP single-phase 3LIs.

However, the control techniques previously discussed are specifically tailored for parallel single-phase full-bridge inverters, which inherently possess ample control flexibility to mitigate circulating currents through the development of suitable control strategies. This inherent flexibility allows for effective CC suppression by simply crafting the appropriate control methodologies. Conversely, the single-phase half-bridge three-level neutral-point-clamped inverters (3LNPCIs) present a unique challenge due to their limited control freedom, with only one degree of control freedom available. This constraint makes it unfeasible to suppress CCs solely through control method adjustments, rendering the aforementioned strategies inapplicable to IPOP single-phase half-bridge 3LNPCIs.

Consequently, there is a pressing need for innovative CC suppression approaches that go beyond conventional control strategies for IPOP single-phase half-bridge 3LNPCIs.

1.2.3 Distributed Fixed-Time Secondary Control for DC Microgrid

The efficient utilization of distributed renewable energy sources is pivotal in advancing the global agenda towards decarbonization. In this context, microgrids emerge as a versatile and efficient framework for assimilating a diverse array of renewable energies, garnering substantial interest in recent decades due to their potential in fostering a sustainable energy landscape [81], [82]. A typical microgrid configuration encompasses distributed generators (DGs), such as solar panels, wind turbines, and other renewable energy sources, alongside energy storage systems like batteries, and various loads that the microgrid is designed to serve. The unique composition of microgrids allows for a tailored approach to energy generation, storage, and consumption, reflecting the specific needs and resources of their respective environments. DC microgrids stand out for their streamlined system architecture and simplified control mechanisms, compared with AC counterparts. The inherent compatibility of DC microgrids with the increasingly prevalent DC-based renewable energy sources (e.g., PV) and loads (e.g., LED lighting, electronic devices) minimizes the need for frequent energy conversions, thereby reducing energy losses and enhancing overall efficiency. This characteristic, coupled with the reduced complexity in system design and operation, positions DC microgrids as a promising solution for the next generation of green energy distribution networks [83].

In the context of DC microgrids, the optimization of current distribution among DGs is pivotal for enhancing both economic efficiency and power dispatch reliability [84]. This objective has led to the development of various control strategies, which are primarily categorized into decentralized, distributed, and centralized approaches. Among these, decentralized control, exemplified by droop control techniques, has garnered significant attention and has been widely implemented within DC microgrid systems [85]. However, this approach presents a fundamental trade-off: achieving precise current sharing often comes at the expense of voltage deviation within the system. On the other hand, centralized control mechanisms offer the advantage of simultaneous current sharing and voltage regulation at the DC bus. Despite these benefits, the centralized approach is marred by its vulnerability to single-point failures, rendering it less suitable for expansive DC microgrid applications. This delineation of control methodologies underscores the inherent challenges in balancing system reliability, efficiency, and scalability within DC microgrid management.

To adapt to the large-scale application and mitigate the risk of single-point failures within DC microgrids, the concept of distributed secondary control has emerged as a promising solution, garnering considerable interest within the field. This control paradigm is characterized by its distributed nature, where each DG communicates only with its immediate neighbors, eliminating the need for a centralized control entity. This approach significantly enhances the robustness and flexibility of the microgrid, making it more resilient to failures and adaptable to expansion.

A notable implementation of distributed secondary control is the consensus algorithms-based control scheme, as suggested in [86], which is designed to ensure DC bus voltage regulation and achieve proportional power sharing among DGs within islanded DC microgrids. This scheme leverages the principles of consensus algorithms to enable coordinated control among the DGs based on local interactions, ensuring that all units collectively maintain the desired operational parameters. Further advancements in distributed secondary control include the adoption of pinning control strategies, as reported in [87]. This innovative approach allows the system to maintain stable and efficient operation even when only a single DG has access to the DC bus voltage measurement, showcasing the potential for enhanced system resilience. Additionally, a novel control framework inspired by the concept of 'virtual voltage drop' has been introduced in [88], offering a unique solution for voltage regulation and power sharing without direct reliance on DC bus voltage information. This method employs a virtual representation of voltage drops across the microgrid to guide the control actions, ensuring accurate voltage control and equitable power distribution among the DGs needless of DC bus voltage measurement, thereby further bolstering system reliability. These developments in distributed secondary control for DC microgrids represent significant strides towards realizing robust, efficient, and scalable renewable energy systems.

Although the distributed secondary control methods previously discussed have been effective in achieving asymptotical stability within DC microgrids, they typically suffer from slow convergence rates. To address this limitation and enhance the dynamic response of the system, recent research has introduced a distributed finite-time secondary control approach [89], [90], designed to not only ensure stability but also to significantly expedite the system's convergence rate by imposing an upper bound on the settling time. Despite these advancements, the reliance of the finite-time control's convergence on the initial system states poses challenges, as these states are intricately linked to the overall stability of the system and difficult to obtain. In an effort to overcome the limitations associated with initial state dependency, a novel approach has been explored through the development of a distributed fixed-time secondary control method [91]. This method employs fixed-time consensus theory to ensure both rapid voltage recovery and accurate power sharing within typical DC microgrids, independent of the initial system states. Further extending the concept, a newly reported iteration of distributed fixed-time secondary control [92] integrates the 'virtual voltage drop' concept [88] with average consensus theory, aiming to enhance control efficiency in DC microgrids. However, this approach necessitates the transmission of two variables among neighboring DGs, complicating implementation and increasing the communication load, potentially leading to network congestion.

Therefore, to facilitate the control implementation and reduce communication burden, a novel secondary control strategy is urgently needed.

1.2.4 Distributed Event-Triggered Fixed-Time Secondary Control for DC Microgrids Without Continuous Signal Transmission

Notably, the distributed secondary control strategies mentioned in Section 1.2.3 require the periodic communication, where signals are sent at regular, short intervals, poses scalability challenges in expanding microgrid systems. As the number of components in the system increases, so does the volume of communication traffic, potentially leading to network congestion and packet loss. This issue is particularly pertinent in larger or more complex microgrid configurations, where efficient communication is crucial for maintaining system stability and performance.

To mitigate these challenges, the adoption of event-triggered communication has emerged as a promising solution. Event-triggered strategies deviate from the traditional periodic communication model by initiating data transmission only when certain predefined conditions or 'events' are met, rather than at fixed time intervals. This approach offers several key advantages for microgrid control systems:

1. Reduced Communication Frequency: By transmitting data only when necessary, event-triggered communication significantly reduces the overall number of transmissions. This reduction in communication frequency directly translates to lower network traffic, mitigating the risk of congestion and packet loss.

2. Enhanced System Scalability: The decreased communication load makes the control strategy more scalable, allowing for the integration of additional DGs or loads without a proportional increase in communication burden. This scalability is essential for the future expansion and flexibility of microgrid systems.

3. Improved Efficiency: Event-triggered communication can lead to more efficient use of network resources, as bandwidth and processing power are conserved by eliminating unnecessary data transmissions. This efficiency is particularly beneficial in systems with limited communication infrastructure.

The exploration of event-triggered communication within the distributed secondary control framework represents an innovative step towards addressing the inherent communication challenges in microgrid management. Research and developments in this area, as indicated in references [93]–[97], are paving the way for more resilient, efficient, and scalable microgrid systems, capable of accommodating the dynamic demands of modern energy distribution networks.

An important research trend in event-triggered based distributed secondary control is achieving faster convergence speeds. This evolution has progressed from ensuring asymptotic stability to achieving finite-time and then fixed-time stability, with each advancement aimed at enhancing system response times.

Asymptotic to Finite-Time Stability: Initial event-triggered control strategies focused on achieving asymptotic stability, ensuring system stability over an indefinite period without necessarily optimizing for convergence speed. The work in [93] introduces a distributed event-triggered H_∞ consensus control that addresses uncertainties and achieves proportional current sharing, but the steady-state voltage deviations in the DC bus cannot be completely eliminated. Advancements in this domain, such as the distributed event-triggered secondary control proposed in [94], have improved upon this by ensuring precise DC bus voltage regulation and accurate current sharing, significantly reducing the frequency of communications required for control. Furthermore, the event-triggered communication version of [88] is presented in [95]. This method outperforms the one reported in [94] with the equivalent control functions and needless bus voltage data, benefiting the reduced use of voltage sensors and the enhanced system robustness. To address the need for faster system response, research in [96] introduced a distributed event-triggered finite-time secondary control for islanded AC microgrids, focusing on rapid frequency restoration and voltage recovery while ensuring the desired power distribution among DGs. However, the transient settling times in this approach are influenced by the system's initial states, linking control performance closely with system stability.

Transition to Fixed-Time Stability: The progression towards fixed-time stability aims to overcome the limitations associated with initial state dependency. Yet, existing methods like the one in [97] for AC microgrids still rely on continuous communication to determine triggering instants, which contradicts the fundamental principle of event-triggered communication.

Up to now, there is a paucity of research on the distributed event-triggered fixed-time secondary control without any continuous communication for achieving fast dynamics with a reduced requirement for signal transmissions in DC microgrids. Coupled with this, the issue of stability in the event-triggered fixed-time secondary control technique for DC microgrids has not been explored yet.

To bridge this research gap and tackle the previously mentioned control challenges, a fast-converging distributed secondary control strategy without any continuous communication is worth studying and is imperatively needed for islanded DC microgrids.

1.3 Contributions and thesis Layout

1.3.1 Major Contributions

Arising from these research gaps, the principal findings of this thesis are itemed as follows:

Firstly, to deal with the common ground circulating currents caused by PV grounding faults, an elaborate decentralized control approach has been proposed. Initially, this thesis delves into the impact of PV grounding faults on system stability. Utilizing the equivalent representation of circulating currents, a tailored control mechanism is developed to curtail the common ground circulating currents. In addition, to maintain current stability and DC-link voltage levels during grounding fault transients, a supplementary control strategy is employed. This strategy enables the operation of a three-level PV interfacing converter to minimize the surges in currents and DC-link voltages. The integration of the dual controllers and the three-level converter ensures the effective eradication of circulating currents under both steady and transient conditions. Notably, the decentralized nature of the proposed control methodologies significantly enhances the system's stability and scalability. The efficacy of the proposed strategies is corroborated through real-time hardware-in-the-loop (HIL) testing.

Secondly, to suppress the circulating currents among the IPOP half-bridge 3LNPCIs, this thesis has proposed a novel decentralized CC suppression strategy leveraging an enhanced 3LNPCI topology. Initially, a comprehensive mathematical model detailing the currents within the IPOP 3LNPCIs is formulated. This model facilitates a thorough analysis of various factors affecting the currents in IPOP 3LNPCIs. The analysis underscores that the optimizing IPOP 3LNPCI operation encompasses a complex multi-objective control task, aiming for both proportional current distribution across 3LNPCIs and effective CC mitigation. Subsequently, this thesis critiques the inherent constraints of the traditional half-bridge 3LNPCI configuration, demonstrating its limited modulation freedom, which, while sufficient for proportional current distribution, falls short in CC attenuation. To overcome the limitations of the traditional design, an advanced 3LNPCI topology is introduced, offering increased modulation flexibility. This revised topology underpins the development of a cutting-edge decentralized control technique, tailored to both suppress CCs and achieve the desired current sharing precision. The practical viability and performance of this innovative approach are substantiated through rigorous hardware-based experimental evaluations.

Thirdly, to fulfill the requirement that achieves rapid dynamic response with fewer signal exchanges in DC microgrids, this thesis has introduced an innovative fixed-time secondary control strategy, meticulously crafted to concurrently regulate DC bus voltage and facilitate proportional current distribution among DGs within a fixed timeframe. A distinctive feature of this strategy is its reliance on broadcasting a single variable to adjacent DGs, substantially decreasing communication burden and simplifying implementation relative to the latest reported approaches with two variables transmitted. Additionally, the strategy obviates the need for DC bus voltage measurement, thereby enhancing system dependability. The stability and robustness of the proposed framework are thoroughly scrutinized through theoretical analysis. Simulation test results are presented to corroborate the efficacy and practical applicability of the strategy.

Fourthly, to further reduce the signal transmission, a distributed event-triggered fixed-time secondary controller has been proposed. In this control scheme, an event-triggered communication protocol is developed, wherein each DG is required to transmit only the most recent variable value to its neighbors upon meeting certain event-triggering criteria, significantly diminishing the need for frequent communication. This approach can also obviate bus voltage measurement, thereby streamlining implementation and bolstering system dependability. The stability of the proposed control strategy is meticulously validated, with assurances provided against the occurrence of Zeno behavior. A series of simulations and experimental validations are conducted to demonstrate the practicality and effectiveness of the proposed strategy.

1.3.2 Thesis Layout

The structural composition of this thesis is depicted in Fig. 1-5.

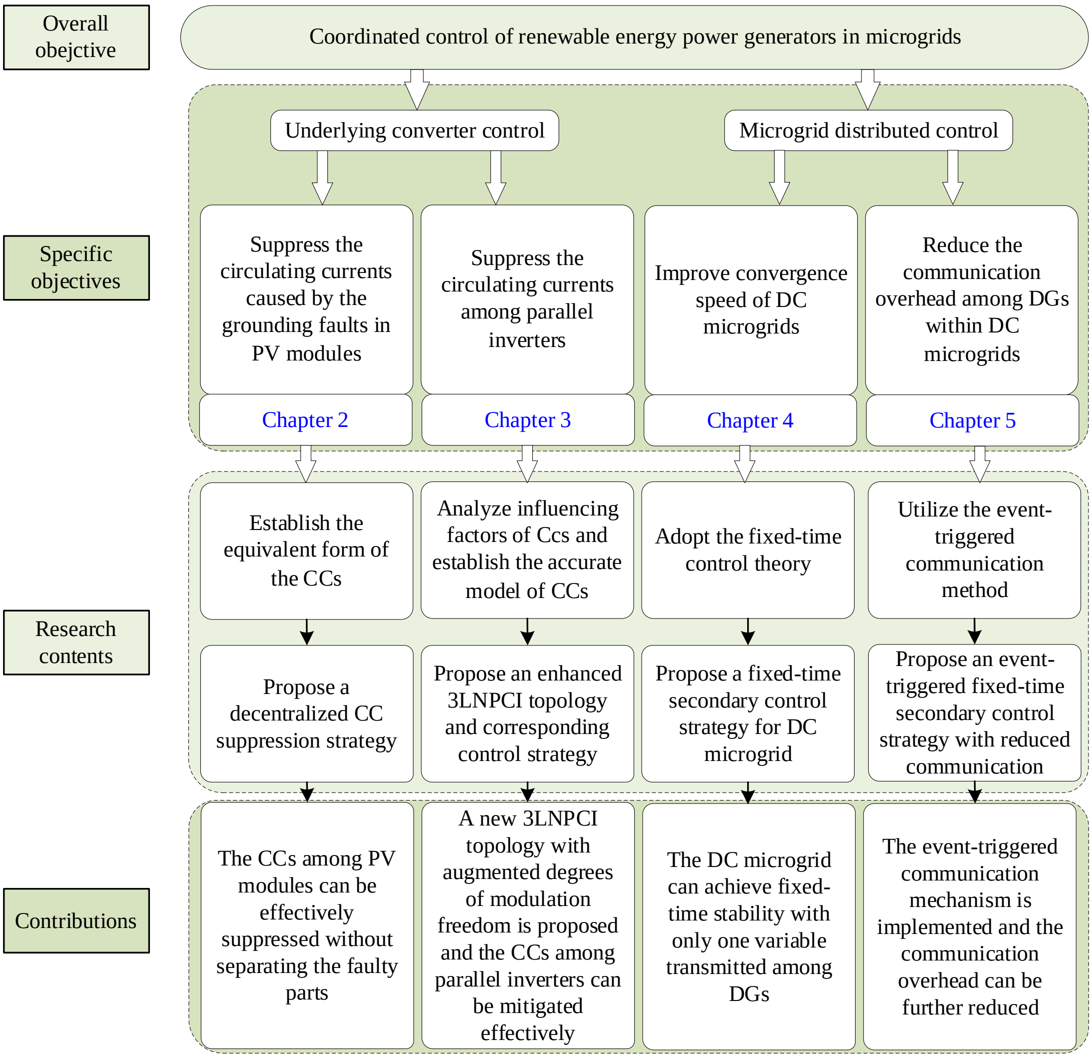

Fig. 1-5. Thesis structure.

This thesis is mainly structured based on the different control hierarchies of microgrids (i.e., primary control of converters, and secondary control of microgrids). In Chapter 2, a comprehensive control scheme is proposed to suppress the circulating currents caused by the grounding faults in PV modules. In Chapter 3, a circulating currents suppression strategies based on the modified 3LNPCI topology is detailed for

IPOP inverters in AC microgrids. In Chapter 4, a fixed-time secondary control is proposed for DC microgrid to accelerate the convergence of system states. Then, in Chapter 5, an event-triggered fixed-time control strategy for DC microgrids is demonstrated to further reduce the communication overhead. Finally, Chapter 6 encapsulates the thesis and prospects the future research endeavors.

Chapter 2 Decentralized Suppression Strategy of Common Ground Circulating Current Caused by Grounding Fault in PV Modules in Single-Phase PV Grid-Connected Systems

2.1 Introduction

The ground faults in PV modules will generate circulating currents among the equipment, and these circulating currents exacerbate the current strain on switches, compromise the quality of grid power, and pose risks to system stability, necessitating the development of preventive measures. However, the reported methods usually detect the faulty parts and then simply isolate the faulty components. These methods can lead to elevated power dissipation, undermine economic efficiency, and jeopardize the stability of PV systems.

Prompted by this issue, a dependable and cost-effective strategy to address the challenges imposed by grounding faults in single-phase PV grid-connected systems is designed [98] in this chapter. The core achievements and contributions of this part are outlined as:

1) The impact of PV grounding faults is delved into, with a particular focus on elucidating the genesis of common ground circulating currents (CGCC). Additionally, it addresses how inaccuracies in measuring DC-link voltages lead to system instability.

2) The equivalent representation of the faulty circulating current is established as the disparity between the positive and negative currents in the single-phase inverter. Building upon this foundation, a novel decentralized inverter control strategy employing an innovative modulation technique is proposed for the AC side, aimed at mitigating the circulating current during steady-state operation.

3) In an effort to diminish the surges in currents and DC-link voltages during transient grounding faults, this chapter incorporates a three-level buck converter in the first DC/DC conversion stage. This three-level buck converter, in comparison to its conventional counterpart, offers enhanced modulation flexibility, contributing to the further reduction of circulating currents and the consequent attenuation of transient

overshoots. Additionally, a decentralized control approach is tailored for this converter on the DC side, enabling the three-level buck converter to effectively mitigate overshoots during transient conditions.

4) The strategies put forward are decentralized and operate independently of communication devices, thereby enhancing reliability, flexibility and scalability while also minimizing costs.

Specifically, the effects of grounding faults on the system are examined in Section 2.2 to be used as the foundation of the controller design. The put forward decentralized inverter control strategy for the AC side is detailed in Section 2.3 to mitigate the circulating currents in the AC side, and the topology of the three-level buck converter is introduced and its associated control strategy on the DC side is also elaborated in Section 2.4 to suppress the current and voltage overshoots. Comparative experiments between the proposed three-level buck converter and the traditional buck converter, serving as the first stage DC/DC converter, are conducted on the RT-LAB experimental platform in Section 2.5, and these experiments validate the effectiveness of the proposed approach. Finally, the summary of this chapter is presented in Section 2.6.

2.2 The Influence of the Grounding Fault in PV Modules on System Stability

The circuit layout for the two-stage PV inverter is illustrated in Fig. 2-1. Within this configuration, a traditional buck converter functions as the first DC/DC conversion stage, while an H-bridge inverter is utilized for the subsequent DC/AC inversion phase. It's important to highlight that the insights gained from analyzing grounding faults in this two-stage setup are equally relevant to alternative two-stage configurations employing different first-stage DC/DC converters, such as buck-boost converters. For the sake of clarity, the grounding fault analysis is conducted on two PV generation systems, yet the findings and conclusions are extendable to systems comprising N ($N > 2$) PV arrays.

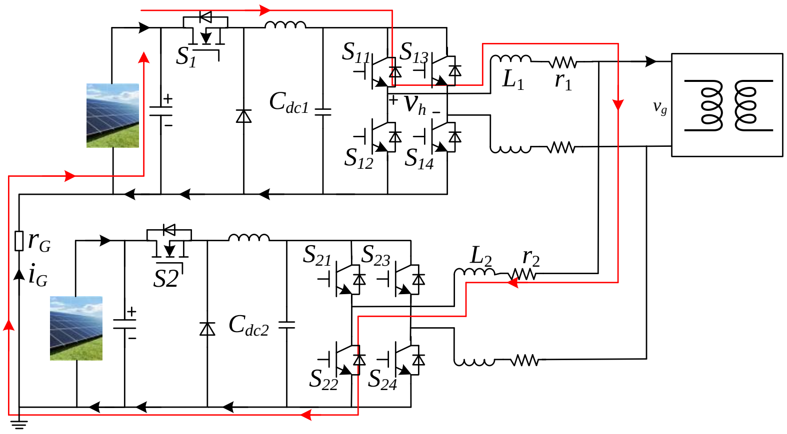

Fig. 2-1. The circuit schematics for the two-stage PV inverter studied in this Chapter.

As depicted in Fig. 2-1, the occurrence of a PV grounding fault leads to the formation of an auxiliary ground path. The diverse switching states of the two inverters introduce additional routes for the CGCC, i_G. Specifically, simultaneous activation of switches S_{11} and S_{22} enables the circulating current to traverse the path highlighted in red in Fig. 2-1. This unintended current flow poses risks of damaging the switches, inducing inductor saturation, reducing equipment longevity, and potentially precipitating a complete system failure.

Fig. 2-1 illustrates the topology of the single-phase H-bridge inverter, where L denotes the filter inductor, r represents the inductor's parasitic resistance, i_L is the current through inductor L, v_g is the AC bus voltage, and v_h is the AC output voltage from the H-bridge. The mathematical model of the H-bridge inverter, within a stationary reference frame, can be formulated as follows:

$$L\frac{di_L}{dt} = v_h - ri_L - v_g \,. \tag{2-1}$$

To analyze the faulty circulating current more effectively, the AC state variables of the H-bridge inverter (within the stationary reference frame) are transformed into DC state variables in the d-q rotating reference frame. The conversion process is detailed below. Initially, the AC state variables (i_L, v_g, v_h) are each delayed by 90 degrees to acquire their respective virtual orthogonal counterparts (i_{Ls}, v_{gs}, v_{hs}), as depicted in Fig. 2-2. Subsequently, the transformation is executed as follows:

$$\begin{bmatrix} i_d \\ i_q \end{bmatrix} = T\begin{bmatrix} i_L \\ i_{Ls} \end{bmatrix},\ \begin{bmatrix} v_{gd} \\ v_{gq} \end{bmatrix} = T\begin{bmatrix} v_g \\ v_{gs} \end{bmatrix},\ \begin{bmatrix} v_{hd} \\ v_{hq} \end{bmatrix} = T\begin{bmatrix} v_h \\ v_{hs} \end{bmatrix}, \tag{2-2}$$

where T is the transformation matrix described as:

$$T = \begin{bmatrix} \cos\theta & sin\theta \\ -sin\theta & cos\theta \end{bmatrix}, \tag{2-3}$$

where θ is the rotation angle, as presented in Fig. 2-2.

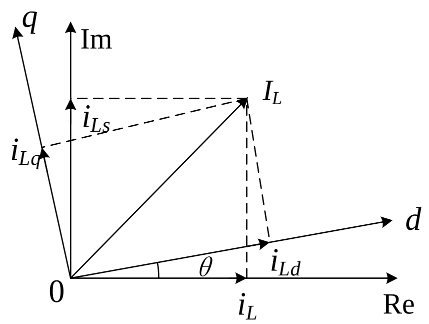

Fig. 2-2. The sketch of virtual vectors and coordinate transformation.

Upon integrating equation (2-3) into equation (2-2), the resultant expression delineates the average model for the filter inductor current within the *d*-*q* rotating frame as follows:

$$\begin{cases} L\dfrac{di_{Ld}}{dt} = v_{hd} - ri_{Ld} + \omega L i_{Lq} - V_g \\ L\dfrac{di_{Lq}}{dt} = v_{hq} - ri_{Lq} - \omega L i_{Ld} \end{cases} \tag{2-4}$$

where V_g represents the amplitude of the AC bus voltage v_g, and ω denotes the angular frequency associated with the voltage v_g.

The state equations for the faulty loop, derived in accordance with Kirchhoff's Voltage Law, are presented as follows:

$$\begin{cases} r_G i_{Gd} - v_{dc1}d_{d1} + L_1\dfrac{di_{Ld1}}{dt} + r_1 i_{Ld1} - r_2 i_{Ld2} - L_2\dfrac{di_{Ld2}}{dt} + v_{dc2}d_{d2} = 0 \\ r_G i_{Gq} - v_{dc1}d_{q1} + L_1\dfrac{di_{Lq1}}{dt} + r_1 i_{Lq1} - r_2 i_{Lq2} - L_2\dfrac{di_{Lq2}}{dt} + v_{dc2}d_{q2} = 0 \end{cases} \tag{2-5}$$

where the subscripts 1 and 2 denote two distinct inverters, v_{dc1} and v_{dc2} correspond to the DC-link voltages of these inverters, respectively, d_{d1}, d_{q1}, d_{d2}, d_{q2} are the duty-cycle of two inverters in the *d*-*q* rotating frame, and i_{Gd} and i_{Gq} represent the decomposition values of i_G on the *d*-axis and *q*-axis, respectively.

The steady-state value of the CGCC is determined by making the differential components in equation (2-5) equal zero. Consequently, the CGCC in the steady state is derived as follows:

$$\begin{cases} i_{Gd} = \dfrac{-1}{r_G}(-v_{dc1}d_{d1} + r_1 i_{Ld1} - r_2 i_{Ld2} + v_{dc2}d_{d2}) \\ i_{Gq} = \dfrac{-1}{r_G}(-v_{dc1}d_{q1} + r_1 i_{Lq1} - r_2 i_{Lq2} + v_{dc2}d_{q2}) \end{cases}. \tag{2-6}$$

Due to the typically negligible magnitude of ground resistance r_G in large PV installations, implemented to safeguard personnel within the solar farm vicinity and protect electrical devices [99], the right-hand side of equation (2-6) may yield a considerably large value, even with a minor value enclosed within parentheses, thereby indicating a substantial circulating current.

Initially, owing to the varying output power of individual PV modules, the delivered currents from inverters diverge, denoted as $i_{dc1} \neq i_{dc2}$, resulting in $r_1 i_{Ld1} \neq r_2 i_{Ld2}$. Consequently, the circulating current i_G will occur. Moreover, in single-phase systems, v_{dc1} and v_{dc2} are not purely DC values and inherently encompass double-frequency components. As per equation (2-6), i_G encompasses intricate AC current components.

Furthermore, discrepancies in the sensing network and DC voltage regulation can induce minor yet significant voltage disparities between v_{dc1} and v_{dc2}. Under normal circumstances without grounding faults, such differences do not disrupt system operation. However, during grounding fault occurrences, this voltage incongruity poses a threat to system integrity. For instance, if the actual value of v_{dc2} surpasses that of v_{dc1}, equation (2-6) predicts the generation of a common ground current. Compounding this issue is the altered circuit topology resulting from the ground fault: the negative terminals of C_{dc1} and C_{dc2} are shorted together, while their positive terminals are linked through switches and inductors. In detail, when the upper switches of inverter 1 and inverter 2 are simultaneously activated, a pathway is established connecting the positive terminals of C_{dc1} and C_{dc2}, essentially connecting them in parallel. Given that v_{dc2} exceeds v_{dc1}, C_{dc2} discharges while C_{dc1} charges in this scenario, leading to a rise in v_{dc1} and a drop in v_{dc2}. Concurrently, the controller of inverter 1 seeks to regulate v_{dc1} to its reference value, causing the duty cycle of the switches to escalate continuously. Ultimately, the system spirals out of control. This underscores how even minor discrepancies between the actual values of v_{dc1} and v_{dc2} can jeopardize normal system operation.

The aforementioned analysis regarding the CGCC and the loss of system stability during grounding fault conditions will be substantiated through experimental tests obtained from RT-LAB tests, as detailed in Section 2.5.

Given that the circulating current exacerbates stress on switches and undermines equipment reliability, addressing these issues is of paramount importance. Sections 2.3 and 2.4 will introduce the proposed strategies aimed at mitigating these challenges.

2.3 Circulating Current Suppression Strategy in AC Side

2.3.1 Equivalent Form of CGCC

In the absence of grounding faults in PV modules, Kirchhoff's current law dictates that the positive and negative currents of each inverter are equal, as represented by $i_{L1}^{+} - i_{L1}^{-} = 0$ (see cut set 1) and $i_{L2}^{+} - i_{L2}^{-} = 0$ (see cut set 2) as depicted in Fig. 2-3. Both inverters function independently and operate normally. However, in the event of a grounding fault, the input ports of the two inverters become interconnected, altering the circuit topology. Referring to Fig. 2-3, it follows that:

$$\begin{cases} i_{L1}^{+} - i_{L1}^{-} = i_G \\ i_{L2}^{+} - i_{L2}^{-} = -i_G \end{cases} . \tag{2-7}$$

This implies that the circulating current traverses both inverters, resulting in unequal positive and negative currents for each. Consequently, the CGCC can be regarded as the disparity between the positive and negative currents of each inverter.

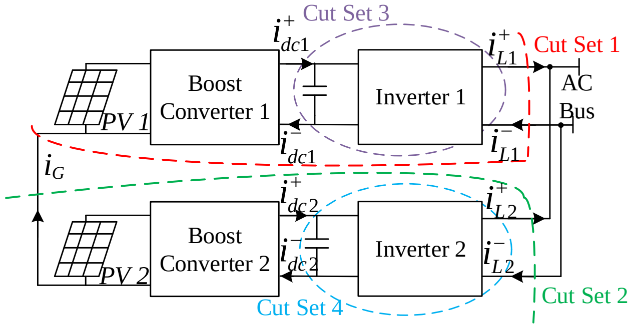

Fig. 2-3. Sketch of two PV inverter system with the grounding fault condition.

Furthermore, based on the cut set 3 and 4, we have

$$\begin{cases} i_{dc1}^{+} - i_{dc1}^{-} = i_{L1}^{+} - i_{L1}^{-} \\ i_{dc2}^{+} - i_{dc2}^{-} = i_{L2}^{+} - i_{L2}^{-} \end{cases}. \tag{2-8}$$

Note that $i_{L1}^{+} \neq i_{L1}^{-}$, i_{dc1}^{+} and i_{dc1}^{-} will also not be equal. As a consequence, the first stage DC/DC converters are susceptible to imbalanced positive and negative currents. This imbalance not only exacerbates the current burden on the semiconductor switching elements but also precipitates the risk of magnetic saturation within the inductors. Such conditions, if not adequately addressed, have the potential to compromise the operational integrity of the power conversion apparatus, culminating in possible equipment failures.

2.3.2 Circulating Current Mitigation

In alignment with the findings delineated above, it becomes evident that the phenomenon of common ground circulating current manifests as a discrepancy between the positive and negative currents within a singular inverter unit. It follows, therefore, that equalizing these current components across the inverter spectrum stands as a viable approach to mitigating the incidence of common ground circulating currents.

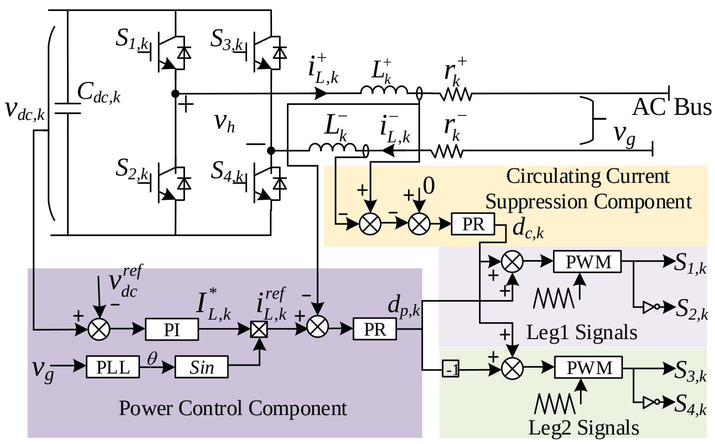

Fig. 2-4. Proposed circulating current suppression strategy for the *k*th inverter.

This section introduces an innovative control paradigm, predicated on a distinct modulation technique, aimed at curbing common ground circulating currents through independent modulation of dual legs within a single inverter. This strategy is characterized by its decentralized nature, obviating the need for inter-inverter communication and relying solely on inverter-specific data.

Fig. 2-4 elucidates the control architecture for an individual single-phase inverter, encapsulating both power regulation and circulating current mitigation mechanisms. The power regulation mechanism employs a Proportional-Integral (PI) controller within the external voltage loop to maintain the DC-link capacitor voltage at its setpoint. The resultant signal then informs the amplitude setpoint for the internal current loop. Within this loop, a Proportional-Resonance (PR) controller is tasked with adhering to a sinusoidal setpoint, thereby generating the $d_{p,k}$ component of power control. This component plays a pivotal role in stabilizing the DC voltage, v_{dc}, in alignment with its reference value.

To ensure parity between the positive and negative currents within the kth inverter, an additional component dedicated to the suppression of circulating currents is incorporated. This involves sampling the positive and negative currents ($i_{L,k}^{+}$ and $i_{L,k}^{-}$) of the kth inverter and leveraging a PR controller to minimize their differential, aiming for a zero reference value. This process yields the circulating current suppression component $d_{c,k}$. Then, it is amalgamated with the power control component $d_{p,k}$ to culminate in the generation of definitive modulation signals for the inverter's two legs.

The modulation duty ratios for these legs are articulated as per equation (2-9), with k=1,2 denoting distinct inverter units.

$$\begin{cases} leg1: d_{c,k} + d_{p,k} \\ leg2: d_{c,k} - d_{p,k} \end{cases}. \tag{2-9}$$

The operational essence of this circulating current mitigation approach is as follows: In the absence of grounding faults, the system functions optimally, maintaining an equilibrium between the positive and negative currents within the inverter, i.e., $i_{L,k}^{+} - i_{L,k}^{-} = 0$, rendering $d_{c,k}$ zero and rendering $d_{p,k}$ the sole modulation signal for both legs. Conversely, in the event of a grounding fault, the resultant circulating current i_G introduces a disparity between the positive and negative currents as per equation (2-7), necessitating the activation of $d_{c,k}$ to counteract the circulating current. For example, should the negative current i_{L1}^{-} in inverter 1 exceed its positive counterpart i_{L1}^{+}, the opposite scenario unfolds in inverter 2, prompting a compensatory response from $d_{c,k}$. Specifically, since $i_{L1}^{+} - i_{L1}^{-} < 0$, $d_{c,k}$ will be positive, and the modulation signal d_p will be offset upward. This adjustment is visually represented in Fig. 2-5, which contrasts the modulation signals and Pulse Width Modulation (PWM) pulses both with and without the dc offset. The dotted red and green lines depict the baseline modulation signals d_p for both legs absent an offset, whereas the solid lines illustrate the modulation signals post-adjustment with a positive d_c offset.

On the one hand, analyzing the impact of modulation signal offsets on switching states reveals that the upward adjustment of modulation signals in inverter1 prolongs the ON-state durations for switches S_1 and S_3. Analogously, in inverter2, switches S_2 and S_4 experience extended ON-states. Consequently, the prevalence of the specific state depicted in Fig. 2-6 escalates, a condition conducive to augmenting the positive current and diminishing the negative current in inverter1. In parallel, this state inversely affects inverter2 by reducing its positive current while amplifying the negative current. The intervention of the dc component ensures a gradual equalization of the positive and negative currents in inverter1, with inverter2 undergoing a reciprocal adjustment. This dynamic equilibrium effectively mitigates the circulating current i_G, as articulated in equation (2-7).

Furthermore, from a modulation standpoint, and considering a constant modulation signal within a single switching cycle, Fig. 2-5 illustrates that the aggregate pulse width of PWM signals, post-positive offset, equals that observed in the absence of such an offset. This observation underscores the fact that the modulation signal shift induced by the circulating current suppression component d_c exerts negligible influence on power regulation. Consequently, this delineates a decoupling between circulating current suppression and power control mechanisms, significantly streamlining the controller design process.

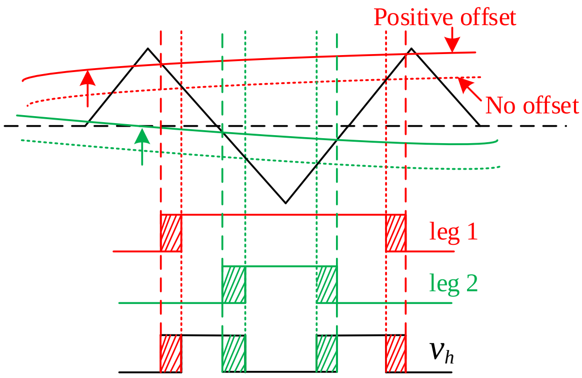

Fig. 2-5. The schematic diagram of modulation signals without offset and with a positive offset and the corresponding PWM pulses.

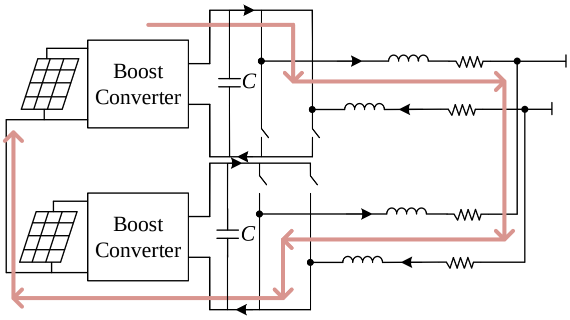

Fig. 2-6. The state with S_1 and S_3 of inverter1 ON and S_2 and S_4 of inverter2 ON.

2.3.3 Controller Design Guideline for the Inverter

The controllers and models' schematic representations are depicted in Fig. 2-7, illustrating the decoupling of d_p (power regulation signal) from d_c (circulating current mitigation signal). This decoupling facilitates the independent design of the power regulation and circulating current curtailment controllers, enhancing the design process's efficiency and effectiveness.

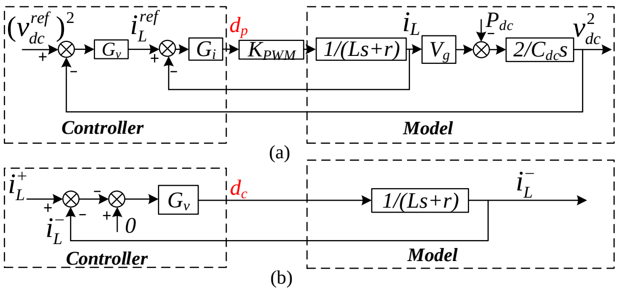

Fig. 2-7. Model and the corresponding controller of (a) power regulation signal d_p, and (b) circulating current suppression signal d_c.

With respect to the power controller, it contains the voltage outer-loop controller

$G_v = k_{vp} + k_{vi} / s$ and the current inner-loop controller $G_i = k_{iP} + k_{iR} / (s^2 + \omega^2)$ to achieve voltage regulation and stabilization of the DC-link capacitor voltage. On the other hand, the circulating current suppression controller is designed as $G_c = k_{cP} + k_{cR} / (s^2 + \omega^2)$ to minimize the discrepancy between positive and negative currents, thereby mitigating circulating currents.

Fig. 2-7 also indicates the application of classical control theory techniques, such as the root locus method and Bode plot analysis, can ascertain optimal values for these controller parameters. The root locus method provides insights into the system's stability and dynamic response by varying the controller parameters, while the Bode plot method aids in understanding the frequency response, allowing for the fine-tuning of the controller parameters to achieve desired performance criteria such as bandwidth, phase margin, and gain margin. These analytical tools are instrumental in ensuring that the controllers not only operate effectively within their respective domains but also contribute to the overall system's robustness and reliability. Eventually, the controller parameters are selected as $k_{vp} = 0.8$, $k_{vi} = 40$, $k_{iP} = 0.01$, $k_{iR} = 1$, $k_{cP} = 0.01$, $k_{cR} = 0.8$.

2.4 Circulating Current Suppression Strategy Based on Three-Level Buck Converter in DC Side

In the AC side inverter control framework delineated in Section 2.3, circulating currents under steady-state conditions are effectively mitigated. Nevertheless, grounding fault scenarios precipitate a topology shift, resulting in the parallel coupling of two dc-link capacitors via activated switches and inductors. This transition triggers significant surges in both currents and DC-link voltages during the PV grounding fault transient phase, posing a substantial risk to the switching apparatus and compromising AC side power quality due to voltage overshoots. To address these transient overshoots instigated by grounding faults, a strategy focusing on the DC side is introduced, aiming to stabilize currents and DC-link voltages during such transients.

The traditional buck DC/DC converter, characterized by its singular switch architecture, offers limited modulation flexibility—restricting control to either output voltage or current without the capability to manage circulating currents.

This section advocates for the adoption of an three-level buck converter in the preliminary DC/DC conversion phase. The dual-switch configuration of the three-level buck converter can not only facilitate enhanced modulation freedom but also have the ability to curtail circulating currents and their associated transient surges in both currents and DC-link voltages, thereby augmenting system resilience and operational stability.

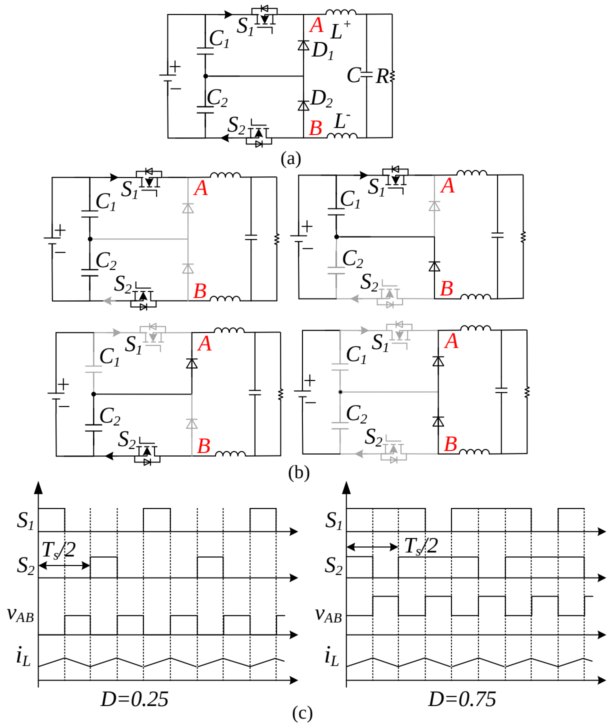

Fig. 2-8. The TL buck converter. (a) The schematic diagram of the circuit topology. (b) Four switching states. (c) The relevant operating waveforms.

2.4.1 Description of Three-Level Buck Converter

The three-level buck converter's architecture is presented in Fig. 2-8. It consists of two switches with low voltage rating S_1, S_2, two diodes D_1, D_2, one positive port inductor L^+, one negative port inductor L^-, two input capacitors C_1, C_2 and one output capacitor C. S_1 and S_2 have the same duty cycle D, and S_2 lags S_1 by half a switching cycle. T_s is the switching cycle. Therefore, four switching states will be generated, as shown in Fig. 2-8 (b). Different duty cycles D will lead to different switching states. To illustrate this, the switching signals of S_1, S_2, waveforms of inductor current and the voltage v_{AB} between point A and point B in two typical cases, that is D=0.25 and D=0.75, are given in Fig. 2-8 (c). As for any other duty cycle, a similar analysis can be conducted.

The three-level buck converter for the initial DC/DC conversion phase offers the advantages: the dual-switch configuration of the three-level buck converter introduces additional modulation flexibility. By deploying suitable control strategies, the three-level buck converter can effectively curtail circulating currents, significantly mitigating the surge in currents and DC-link voltages during PV grounding fault transients, thereby enhancing system robustness and reliability.

2.4.2 Control Strategy of Three-Level Buck Converter

Echoing the AC side analysis, achieving equilibrium between the positive and negative currents in the three-level buck converter is pivotal for minimizing circulating currents, thereby mitigating the surges in currents and DC-link voltages.

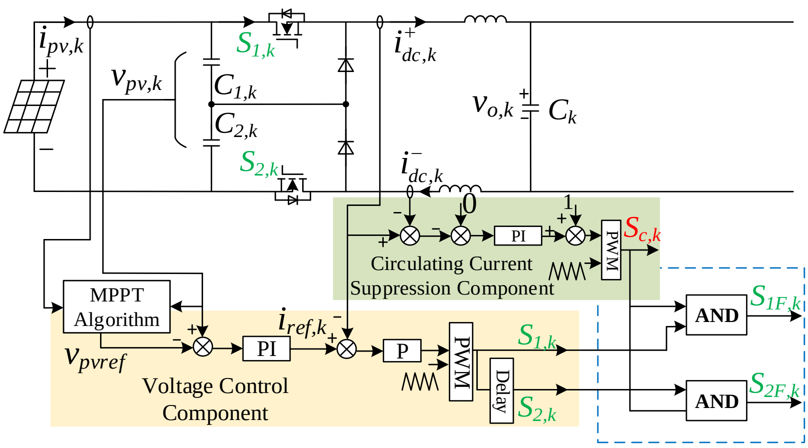

Fig. 2-9. Proposed circulating current mitigation strategy for the kth three-level buck converter.

Fig. 2-9 presents the comprehensive control schematic for the kth improved three-level buck converter, integrating both voltage regulation and circulating current suppression mechanisms. Voltage regulation is achieved through a dual-loop control strategy, where a PI controller $G_v = k_{vp} + k_{vi} / s$ within the outer loop adjusts the voltage across the PV capacitors to their optimal value, harnessing the maximum power from the PV modules. The output from this loop is used as the reference signal for the inner current control loop, which employs a proportional controller $G_i = k_{ip}$ to ensure the stability of the PV capacitor voltage at v_{pvref}.

To further curtail the circulating currents and consequent transient surges, it is essential to equalize the positive and negative currents of the *k*th converter. This is accomplished by introducing a circulating current mitigation signal, which employs a PI controller $G_c = k_{cp} + k_{ci} / s$ to minimize the discrepancy between the positive and negative currents ($i_{dc,k}^{+}$ and $i_{dc,k}^{-}$), aiming for a zero reference value. The resultant circulating current curtailment signal, when combined with the voltage control component through logic AND, yields the definitive control signals for the converter's switches $S_{c,k}$. This strategic integration of control components ensures the effective suppression of circulating currents and stabilization of the system during transient disturbances.

The operational principle behind the mitigation of circulating currents in the three-level buck converter can be explained as follows: Under normal conditions, this equilibrium $i_{dc,k}^{+} - i_{dc,k}^{-} = 0$ ensures the circulating current suppression controller's output remains constant at a value of 1, leading to the maintenance of $S_{c,k}$ at 1 as well. Consequently, the final modulation signals for the converter's switches equal to those generated by the voltage control component, maintaining system stability. However, the onset of a grounding fault introduces a disparity between the positive and negative currents ($i_{dc,k}^{+}$ and $i_{dc,k}^{-}$) due to the emergence of common ground circulating currents. For instance, if the negative current $i_{dc,k}^{-}$ exceeds the positive current $i_{dc,k}^{+}$, the condition $i_{dc,k}^{+} - i_{dc,k}^{-} < 0$ prevails. This imbalance prompts the PI controller to generate a negative output, thereby reducing the circulating current suppression controller's output below 1, and consequently, $S_{c,k}$ will not consistently remain at 1. A critical response is triggered when $S_{c,k}$ drops to zero, leading to the deactivation of switch $S_{c,k}$. This action effectively serially links the negative and positive pole lines through the freewheeling diodes, compelling the negative current $i^{-}_{dc,k}$ to align with the positive current $i^{+}_{dc,k}$. This adjustment expels excess current from the negatively polarized line to other converters where the positive current exceeds the negative, thereby attenuating the CGCCs. Through this dynamic process, not only are circulating currents significantly diminished, but associated transient overshoots in both currents and DC-link voltages are also effectively mitigated, thereby enhancing the overall stability and efficiency of the system during grounding fault conditions.

2.5 Experimental Results

This section delineates a series of experimental validations conducted to substantiate the theoretical analyses presented earlier, particularly those in Section II. The experimental framework is structured into distinct cases, each designed to address specific aspects of the system and the proposed methodologies:

Case 1: Focuses on affirming the analytical insights of Section 2.2, employing the system configuration illustrated in Fig. 2-1. This case serves as a foundational verification step, ensuring the base assumptions and analyses hold true under experimental conditions.

Case 2: Dedicated to evaluating the efficacy of the proposed AC side circulating current suppression technique under steady-state conditions. This is pivotal in demonstrating the practical utility of the method in maintaining system stability and efficiency.

Case 3: Aiming at showcasing the advantages of the three-level buck converter over traditional buck converters in mitigating transient overshoots in currents and DC-link voltages.

Case 4 and Case 5: Aimed at examining the scalability of the proposed methods, these cases increment the number of PV modules within the system to three (PV1, PV2, and PV3), thereby providing insights into the adaptability and robustness of the approaches in larger-scale implementations. The power outputs for PV1, PV2, and PV3 are set at 56 kW, 64 kW, and 69 kW, respectively, offering a diverse range of conditions for evaluation.

Table 2-1 System Parameters

	Electrical Parameters	Values
Improved Buck Converter	v_{dc}, C_{dc}, r_G v_{pvref}, L, C_{pv1}, C_{pv2}	650V, 5mF, 0.01Ω 1200V, 2mH, 1mF,1mF
H-bridge Inverter	L, r, V_g	1mH, 0.01Ω, 311V
	Control Parameters	**Values**
Improved Buck Converter	Voltage and current controller	k_{vp} = 20, k_{vi} = 80 k_{ip} =0.01
	Circulating current suppression controller	k_{cp} = 0.01, k_{ci} =1
H-bridge Inverter	Voltage and current controller	k_{vp} = 0.8, k_{vi} = 40 k_{iP} = 0.01, k_{iR} = 1
	Circulating Current Controller	k_{cp} = 0.01, k_{cR} = 0.8

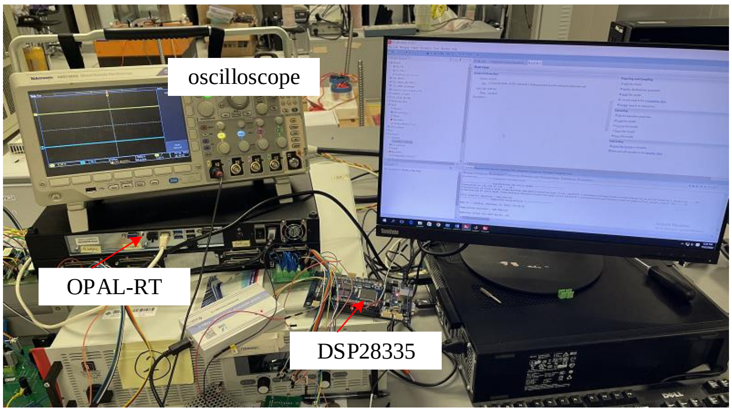

Fig. 2-10. RT-LAB-based experimental platform.

The experimental apparatus encompasses a Hardware-in-Loop (HIL) setup, leveraging RT-LAB and DSP28335 platforms, as depicted in Fig. 2-10. This setup is critical in simulating real-world operational scenarios, enabling an in-depth assessment of the proposed solutions' performance across various system configurations and states. System parameters and configurations pertinent to the experiments are meticulously compiled in Table 2-1, providing a comprehensive reference framework to ensure clarity and reproducibility of the experimental procedures and outcomes.

2.5.1 Case 1 (Two PV Modules, Conventional Buck Converter, No Circulating Current Suppression Strategy)

In this experimental scenario, due to the constraints imposed by the limited number of channels on the oscilloscope, the monitoring scope is narrowed to specific currents: the positive and negative currents of inverter1 i_{L1}^{+} and i_{L1}^{-}, their differential $i_{L1}^{+}-i_{L1}^{-}$, and the negative current of inverter2 i_{L2}^{-}. Similarly, for the buck converters, the positive and negative currents of buck converter1 i_{dc1}^{+} and i_{dc1}^{-}, their differential $i_{dc1}^{+}-i_{dc1}^{-}$, and the negative current of buck converter2 i_{dc2}^{-} are under surveillance. These measured currents facilitate the extrapolation of other relevant currents within the system.

Fig. 2-11 delineates the system's response, as portrayed in Fig. 2-1, under both normal operating conditions and in the event of a grounding fault. During stage I, absent a grounding fault, the system operates optimally with no additional grounding paths. This operational mode is characterized by an equilibrium between the positive and negative currents across each inverter and buck converter, as depicted in Fig. 2-11 (a) and (b), respectively, resulting in a null CGCC. Concurrently, the DC-link voltages of both inverters adeptly track the predefined voltage value of 650V, as illustrated in Fig. 2-11 (c).

Upon the advent of a grounding fault in stage II, an additional circulating current pathway materializes, equating the actual DC-link voltages at 650V. From the DC perspective, while positive currents remain stable, negative currents exhibit erratic fluctuations due to the interconnection of the negative poles of the PV generators via the grounding path, leading to complex unbalanced currents and the genesis of a CGCC, with an amplitude of approximately 25A. Analogously, the AC side witnesses a disparity between the positive and negative currents, commensurate with the circulating current i_G.

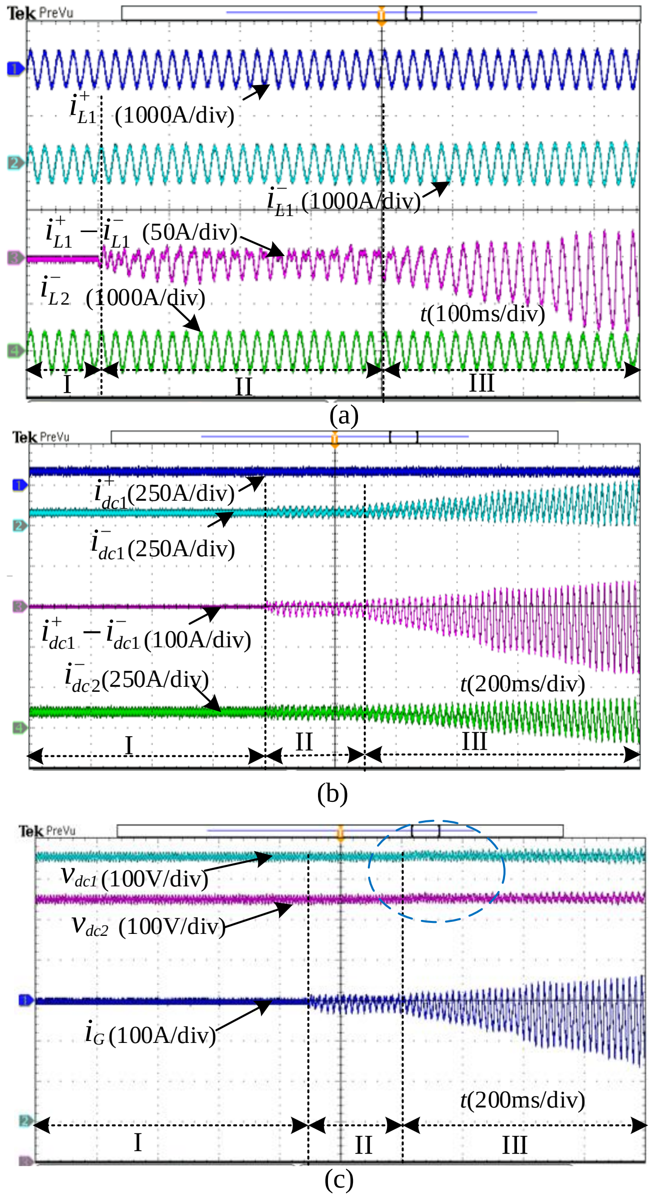

Fig. 2-11. Experiment results of the two-PV system without circulating current control strategy (Case 1). (a) AC side currents. (b) DC side currents. (c) CGCC, DC-link voltages of inverter1 and inverter2.

Transitioning to stage III, an intentional variation is introduced by adjusting the DC-link voltage reference for inverter2 to 655V, maintaining inverter1's reference at 650V. Under the voltage loop controller's influence, v_{dc2} incrementally ascends, as highlighted within the blue ellipse in Fig. 2-11 (c), prompting a continuous charge of C_{dc1} and a subsequent rise in v_{dc1}. However, the inverter1 controller endeavors to revert v_{dc1} to its reference value, thereby necessitating an increase in the duty ratio signals for its switches. This adjustment escalates the discrepancies between the positive and negative currents of the inverters, the CGCC i_G, and other pertinent currents, potentially leading to systemic instability. This scenario underscores the vulnerability of the system to grounding faults, particularly when discrepancies exist between the actual DC-link voltages, corroborating the analyses presented in Section 2.2.

In the following Case 2~5, each one includes two phases. During phase I, the grounding faults is absent, while during phase II, the grounding faults is active.

2.5.2 Case 2 (Two PV Modules, Conventional Buck Converter, Only the Control Strategy in AC Side Is Applied, v_{dc1} is 650V, v_{dc2} is 655V)

Fig. 2-12 illustrates the experimental waveforms for the system outlined in Fig. 2-1, focusing solely on the implementation of the AC side control strategy. The experiment is divided into two stages to assess the system's behavior under normal conditions and during a grounding fault.

Stage I: This initial stage demonstrates the system's operation in the absence of a grounding fault. The system exhibits stable and normal functioning with no evidence of common ground circulating currents, indicating that the AC side control strategy effectively maintains system equilibrium under standard operational conditions.

Stage II: The onset of a grounding fault marks this stage, introducing a significant test for the control strategy. Despite the grounding fault, the experimental results showcased in Fig. 2-12 reveal that the AC side control strategy successfully equalizes the negative and positive currents of the inverters, effectively suppressing circulating currents under steady-state conditions. Moreover, despite the presence of a voltage disparity between the two DC-link voltages, their stability is swiftly regained after a brief transitional phase. However, the transient state induced by the grounding fault precipitates considerable surges in both currents and DC-link voltages, with i_G peaking at approximately 95A and v_{dc1} and v_{dc2} experiencing surges of around 80V. Such pronounced overshoots pose a threat to the switches, potentially compromising their integrity and reducing the overall lifespan of the system components. Furthermore, the voltage overshoots could detrimentally impact the power quality delivered to the AC grid.

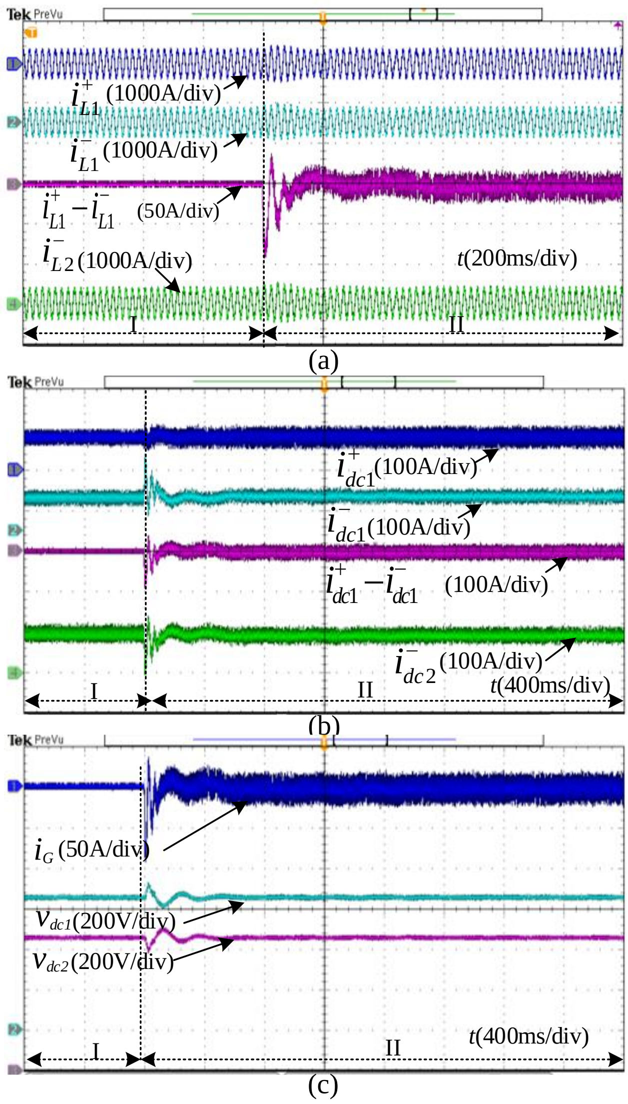

Fig. 2-12. Experimental results based on the proposed control strategy for inverters (Case 2). (a) AC side currents. (b) DC side currents. (c) CGCC, dc-link voltages of inverter1 and inverter2.

To address these transient overshoots, particularly the detrimental effects on currents and DC-link voltages, Cases 3 introduces the three-level buck converter as a replacement for the conventional buck converter in the first stage DC/DC conversion process with the relevant control strategy. The adoption of the improved converter is predicated on its superior capability to mitigate the adverse impacts of transient overshoots, thereby enhancing system resilience and ensuring the protection of critical components while maintaining high-quality power output to the AC grid. This comparative analysis aims to highlight the three-level buck converter's advantages in managing and suppressing undesirable transient effects, underscoring its potential as a robust solution in systems vulnerable to grounding faults.

2.5.3 Case 3 (Two PV Modules, Three-Level Buck Converter, the Control Strategy in Both AC Side and DC Side Are Applied, v_{dc1} is 650V, v_{dc2} is 655V)

Fig. 2-13 showcases the system's response over two stages, emphasizing the performance during normal operation and under a grounding fault condition, particularly highlighting the efficacy of the TL buck converter integrated with the proposed control strategies.

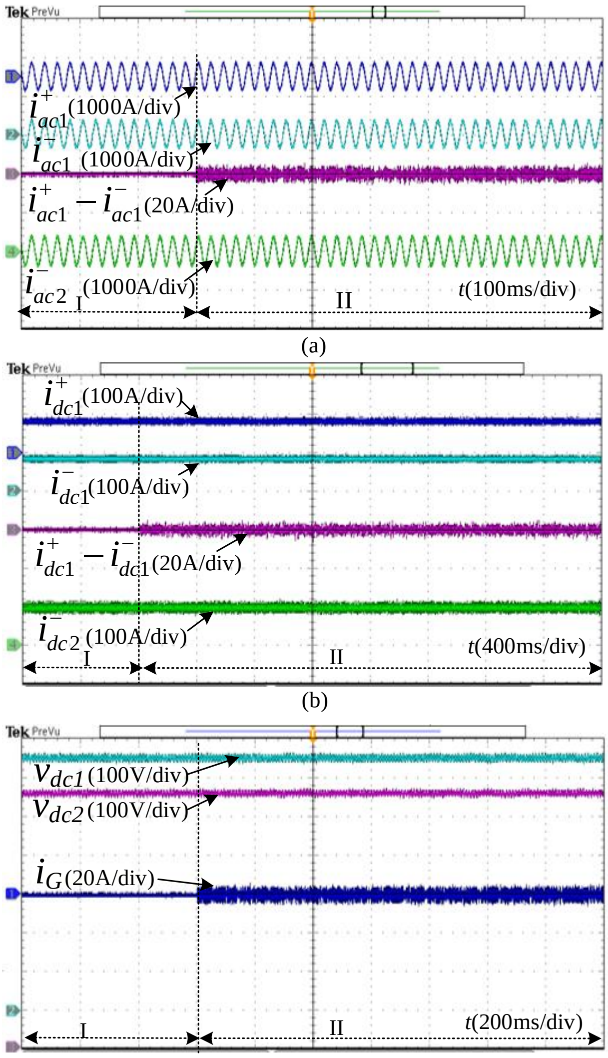

Fig. 2-13. Experimental results with the three-level buck converter as the first stage and the control schemes for inverters and three-level buck converters are activated (Case 3). (a) AC side currents. (b) DC side currents. (c) CGCC, DC-link voltages of inverter1 and inverter2.

Stage I: This initial stage demonstrates the system's operation in the absence of a grounding fault, where the two-stage PV inverters function optimally. The absence of common ground circulating currents and the DC-link voltages' ability to accurately track their reference values indicate a stable and efficient system under normal conditions.

Stage II: The emergence of a grounding fault in this stage presents a critical test for the system's resilience and the effectiveness of the control mechanisms in place. The observations from Fig. 2-13 reveal a significant improvement in the system's ability to manage transient disturbances, with a notable reduction in surges of currents and DC-link voltages when compared to the outcomes in Cases 2. The CGCC is effectively neutralized, maintaining the system's currents and voltages close to their nominal values despite the grounding fault in the PV modules.

These results affirm the superior performance of the three-level buck converter, in conjunction with the tailored control strategies, in mitigating transient overshoots and stabilizing the system under fault conditions.

2.5.4 Case 4 (Three PV Subsystems, Conventional Buck Converter, Only the Control Strategy in AC Side Is Applied, v_{dc1} is 650V, v_{dc2} is 655V, v_{dc3} is 660V)

The experimental exploration extends to a system configuration incorporating three PV modules to assess the scalability and effectiveness of the proposed methods under more complex conditions. This analysis, depicted in Fig. 2-14, is segmented into two operational stages, mirroring the processes employed in previous cases.

Stage I: This stage signifies the system's operation devoid of any grounding faults within the PV modules. The absence of common ground circulating currents during this phase indicates that the system maintains its operational integrity and efficiency, with all components performing within expected parameters.

Stage II: The onset of a grounding fault among the three PV modules introduces a new layer of complexity, generating multiple paths for common ground circulating currents: i_{G12} from PV2 to PV1, i_{G13} from PV3 to PV1, and i_{G23} from PV3 to PV2. Despite these challenging conditions, the results depicted in Fig. 2-14 demonstrate the system's capability to effectively suppress these circulating currents, ensuring that the

DC-link voltages of all three modules remain stable and aligned with their reference values in a steady-state regime. However, similar to previous observations in two-module configurations, the transient state induced by the grounding fault precipitates significant overshoots in both currents and DC-link voltages, highlighting a persistent challenge in managing transient disturbances.

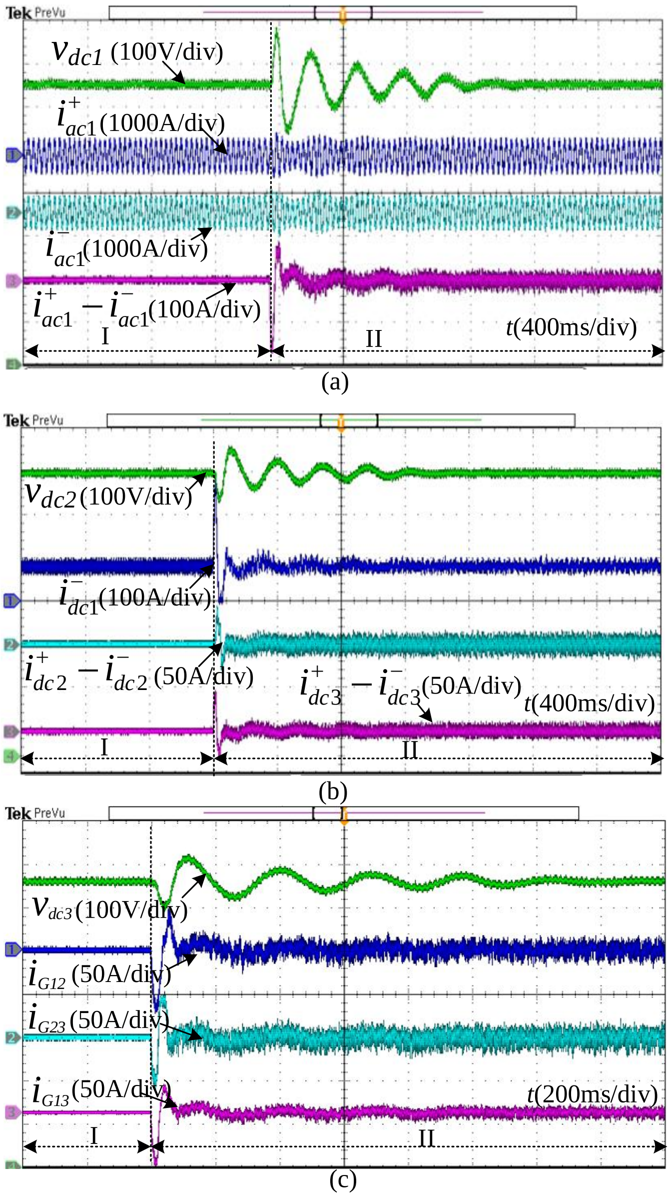

Fig. 2-14. Experimental results of three PV modules with the proposed control scheme for inverters enabled (Case 4). (a) AC currents and DC-link voltage of inverter1. (b) i^-_{dc1}, v_{dc2}, $i^+_{dc2}-i^-_{dc2}$, $i^+_{dc3}-i^-_{dc3}$.

(c) The CGCCs i_{G12}, i_{G23}, and i_{G13}, and v_{dc3}.

To address these transient overshoots and further validate the benefits of the three-level buck converter in a more complex system setup, Cases 5 will introduce the three-level buck converter in the first stage DC/DC conversion for each of the three PV modules. The anticipation is that the three-level buck converter, with its advanced modulation capabilities and additional control freedoms, will offer a more nuanced and effective suppression of transient overshoots, even in the context of a three-module system.

2.5.5 Case 5 (Three PV Subsystems, Three-Level Buck Converter, and the Control Strategies in Both AC Side and DC Side Are Applied, v_{dc1} is 650V, v_{dc2} is 655V, v_{dc3} is 660V)

Fig. 2-15 showcases the experimental outcomes following the integration of the three-level buck converter alongside the newly proposed control strategy within the system containing three PV modules. These results highlight the effectiveness of this combined approach in managing and significantly mitigating transient overshoots that occur due to grounding faults. The key advantages of this method are proved.

In summary, the various results demonstrate that grounding faults in PV systems induce not only common ground circulating currents but also potential system failures due to discrepancies in DC-link voltage measurements. The introduction of an AC-side control strategy effectively mitigates these circulating currents under steady conditions, whereas the implementation of a three-level buck converter on the DC side curtails current and voltage surges during transient events. Remarkably, the system maintains stability and operational integrity, even in the presence of grounding faults, without the need for isolating defective components. Furthermore, scenarios 4 and 5 validate the scalability and applicability of the proposed autonomous control strategies to larger systems comprising more than two PV modules. Moreover, the elimination of communication lines in the proposed method enhances system reliability.

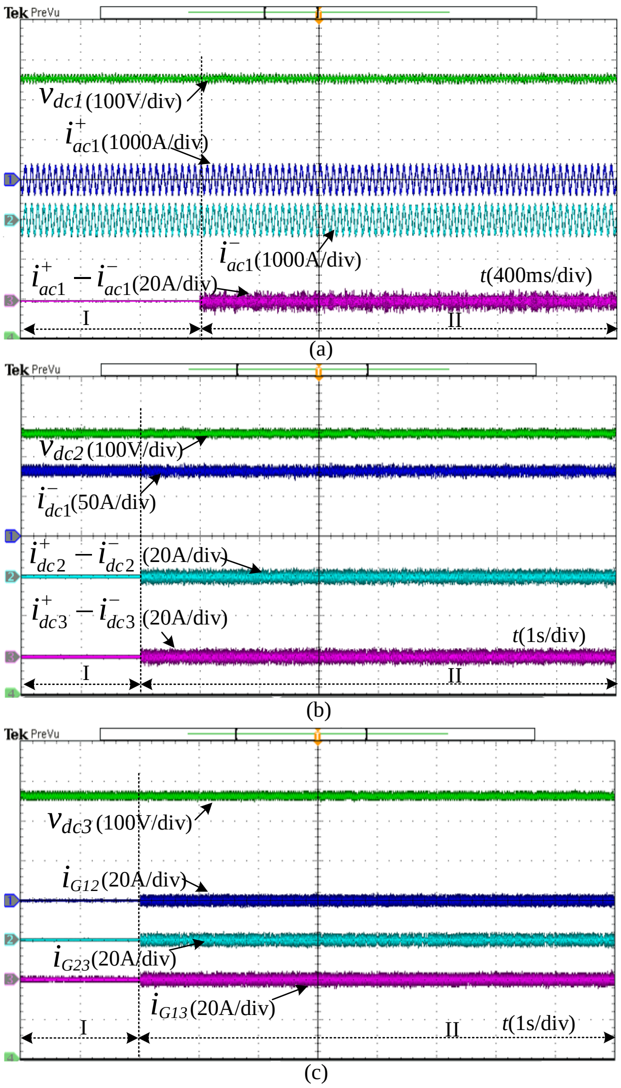

Fig. 2-15. Experimental results of three PV modules with the proposed control schemes for inverters and converters enabled (Case 5). (a) AC currents and DC-link voltage of inverter1. (b) i_{dc1}^{-}, v_{dc2}, $i_{dc2}^{+}-i_{dc2}^{-}$, $i_{dc3}^{+}-i_{dc3}^{-}$. (c) The CGCCs i_{G12}, i_{G23}, and i_{G13}, and v_{dc3}.

2.6 Conclusion

This chapter delves into the challenges imposed by grounding faults in PV modules, notably CGCCs and system instability. A novel, decentralized approach is introduced to resolve these issues. The strategy commences with an AC-side control mechanism devised from an equivalent model of the circulating current, effectively stabilizing these currents under steady states. Additionally, a three-level buck converter, functioning as the primary DC/DC stage, is integrated to attenuate current and voltage surges during fault transients. This converter outperforms traditional buck converters by providing superior transient response and minimizing overshoots. The comprehensive strategy ensures system resilience to PV grounding faults, allowing continuous operation without isolating affected segments. The decentralized nature of the proposed solution enhances scalability, making it suitable for PV systems with multiple modules (N > 2). Experimental validation is provided through real-time Hardware-in-the-Loop testing, corroborating the theoretical framework.

Chapter 3 Suppression of Circulating Currents among IPOP Single-Phase Three-level Inverters for Renewable Energy Power Generation Systems

3.1 Introduction

In renewable energy grid integration systems, single-phase inverters are key devices connecting renewable energy sources to the grid. For the grid integration of large-capacity renewable energy, multiple inverters need to operate in parallel, forming an input-parallel-output-parallel (IPOP) structure. In non-isolated interconnected inverters, the IPOP configuration is prone to various complex circulating currents (CCs) due to the asymmetric hardware parameters, significantly heightening the current stress on the switches, compromising system efficiency and impacting the stable operation of the system. Given its proficiency in mitigating common-mode current, the half-bridge topology, such as the neutral-point clamped (NPC) inverter, stands out as a particularly suitable choice for PV applications, making it an attractive option in the field. When the single-phase half-bridge three-level NPC inverters (3LNPCIs) are adopted as the interfaces between the renewable energy sources and the grid, the circulating current suppression becomes more complicated due to the inherent deficient modulation freedom of the topology.

To address this challenge, a two-pronged approach is necessitated: a revision of the conventional topology of 3LNPCI to introduce additional control freedoms and the formulation of novel control methods tailored to this modified topology. This comprehensive strategy aims to equip 3LNPCIs with the necessary tools to effectively manage and mitigate CCs, highlighting the need for advancements in both inverter design and control technique development.

Until now, limited research has been dedicated to mitigating CCs in IPOP single-phase half-bridge 3LNPCIs. This chapter represents a pioneering effort in devising a decentralized strategy for CC suppression within this specific inverter configuration [100]. The following contributions have been made in this chapter:

1). A comprehensive mathematical model encapsulating the currents in IPOP half-bridge single-phase 3LNPCIs, inclusive of filter and line impedances, has been developed. This model facilitates an in-depth understanding of current dynamics within the IPOP system, laying the groundwork for precise current behavior analysis.

2). Employing the established model, a thorough quantitative examination of various factors affecting the currents has been conducted. It has been discovered that impedance asymmetries on the AC side predominantly induce fundamental-frequency CCs, while those on the DC side can result in significant DC and double-frequency CCs. The operation of IPOP 3LNPCIs is identified as a complex multi-objective control challenge, encompassing both CC suppression and equitable current distribution among multiple units. This complexity is further compounded by the conventional 3LNPCI topology, which offers limited modulation flexibility and falls short in addressing the multi-objective control requirements.

3). To surmount the limitations inherent to the traditional topology, a novel 3LNPCI configuration with enhanced modulation capabilities has been proposed. A novel decentralized control scheme, featuring dual control degrees of freedom, is introduced to concurrently address CC suppression and facilitate proportional current sharing among the IPOP 3LNPCIs. This method stands out for its decentralized nature, making it an ideal fit for modular systems. Importantly, the methodologies developed herein hold potential applicability to other IPOP half-bridge inverter designs, broadening the scope of this research's impact.

3.2 Modeling and Analysis of IPOP Conventional 3LNPCIs

For illustrative purposes, this study employs two IPOP single-phase half-bridge 3LNPCIs as a foundational example to elucidate the associated challenges and solutions. It's important to emphasize that while only two 3LNPCIs are used for demonstration, the CC mitigation techniques and the derived insights presented in this chapter possess a broader applicability. The methodologies and conclusions drawn from this analysis are universally relevant and can be extrapolated to scenarios involving a greater number of IPOP single-phase 3LNPCIs, extending beyond the two-inverter case to systems with N (N > 2) inverters. This generalizability ensures that the proposed solutions can be effectively applied to larger and more complex IPOP configurations, thereby enhancing their practical utility in a wide array of applications.

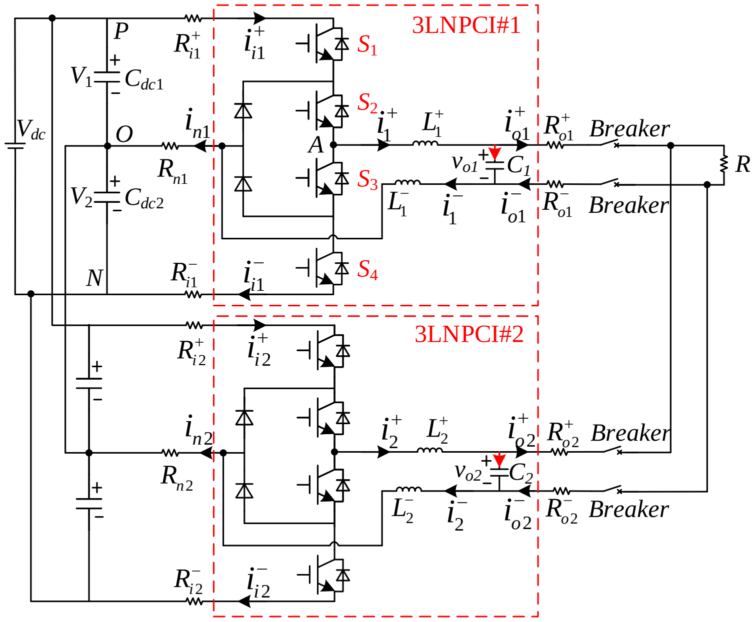

Fig. 3-1. Schematic diagram of two IPOP 3LNPCIs.

3.2.1 Modeling

Fig. 3-1 demonstrates the schematics of two IPOP 3LNPCIs. They provide power to the load R in collaboration. The LC filters of them consist of the inductances of L_1^+, L_1^- and L_2^+, L_2^+, and capacitances of C_1 and C_2, respectively. The positive and negative line resistances in the AC side of 3LNPCI1 and 3LNPCI2 are denoted as R_{o1}^+ , R_{o1}^- and R_{o2}^+, R_{o2}^-, respectively. The DC side resistances of positive, neutral and negative lines are R_{i1}^+, R_{n1}, R_{i1}^- and R_{i2}^+, R_{n2}, R_{i2}^-, respectively. C_{dc1} and C_{dc2} are DC-link capacitors. The red arrow denotes the forward direction of the current flowing through the capacitor.

To elucidate the characteristics of IPOP 3LNPCIs, the fundamental cut sets of these inverters are illustrated in Fig. 3-2 (a). It can be obtained that $i_{o1}^+ - i_{o1}^- = i_{i1}^+ - i_{i1}^- - i_{n1}$ (cut set 1), $\sum_{k=1}^{n} i_{o,k}^{+} - i_{o,k}^{-} = 0$ (cut set 2) and $\sum_{k=2}^{n} (i_{i,k}^{+} - i_{i,k}^{-} - i_{n,k}) = -(i_{o1}^{+} - i_{o1}^{-})$ (cut set 3) based on Kirchhoff's current laws. However, these equations cannot guarantee $i_{o1}^{+} - i_{o1}^{-} = 0$. This phenomenon indicates that there is a disparity between the positive and negative currents of each inverter unit. Contrarily, for the case where only one inverter is used as shown in Fig. 3-2 (b), the positive current and negative current are always equal, i.e., $i_{o1}^{+} = i_{o1}^{-}$. Making a comparison of these two cases, the equal positive and negative currents in single 3LNPCI is no longer guaranteed in IPOP ones. This phenomenon is distinct in IPOP inverters, which indicates that CCs will occur in the single 3LNPCI as shown by the green arrows as presented in Fig. 3-2. The CC in the kth single inverter is expressed as: $i_{kc} = i_{ok}^{+} - i_{ok}^{-}$.

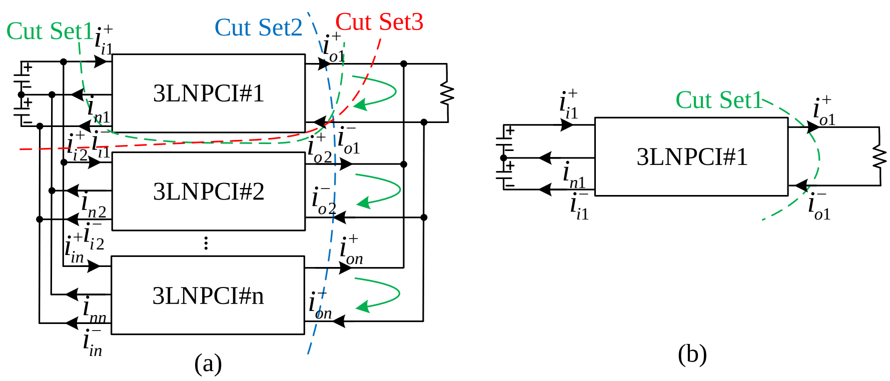

Fig. 3-2. Cut sets of single-phase 3LNPCI. (a) n IPOP 3LNPCIs. (b) One 3LNPCI.

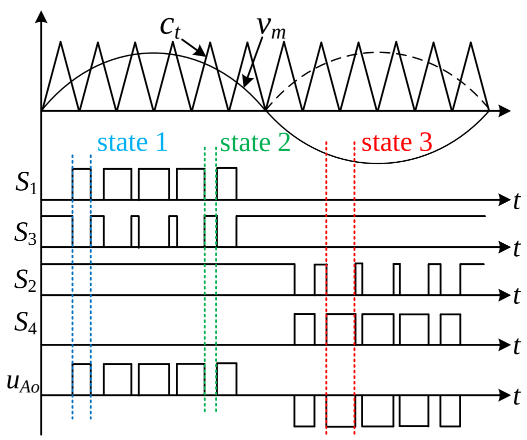

Fig. 3-3. Modulation scheme of 3LNPCI.

The commonly used modulation approach for 3LNPCIs is depicted in Fig. 3-3. In this scheme, switches S_1 and S_2, as well as S_3 and S_4, operate in a complementary fashion, meaning that when S_1 is on, S_2 is off, and similarly, when S_3 is on, S_4 is off, and vice versa. Leveraging this switching arrangement enables the generation of three distinct switching states for the 3LNPCI.

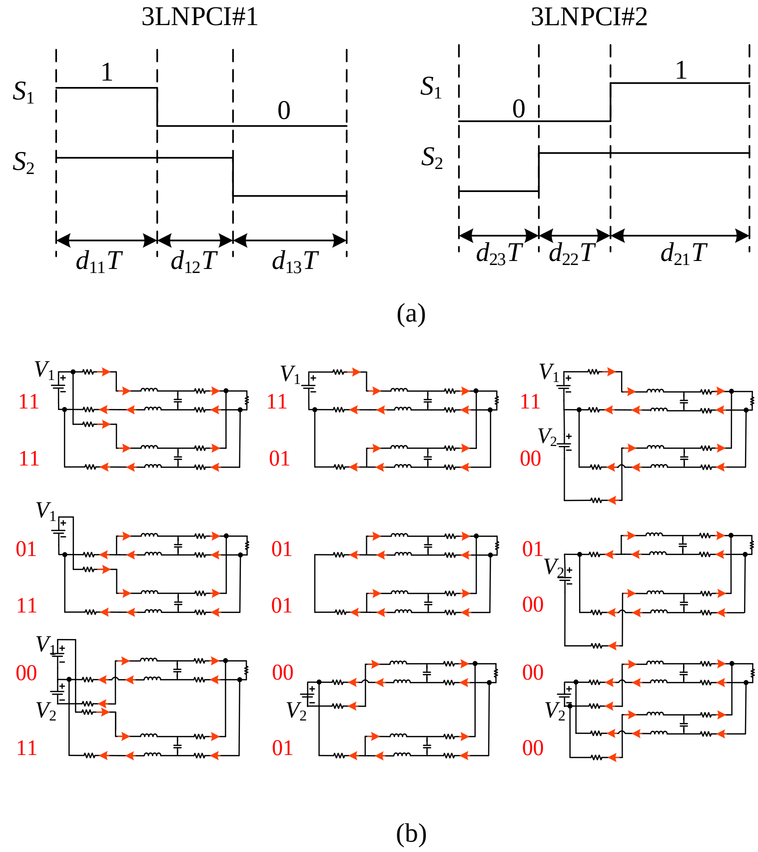

Fig. 3-4. Description of two IPOP 3LNPCIs' switching states. (a) Sketches of duty ratios. (b) Equivalent schematic diagrams correspond to different switching combination.

When considering two IPOP 3LNPCIs, the interaction between their respective three states leads to a total of nine possible switching states, as depicted in Fig. 3-4 (b). Fig. 3-4 (a) provides an overview of the duty cycle representations for 3LNPCI1 and 3LNPCI2, where a "1" indicates the 'ON' state of the switches, and a "0" signifies the 'OFF' state. The different switching states and their corresponding circuit configurations are detailed in Fig. 3-4 (b), with each two-digit combination representing the states of switches S_1 and S_2—'1' for ON and '0' for OFF. It's important to note the parallel arrangement of the DC-link capacitors in the two 3LNPCIs, which results in identical voltages across C_{dc1} and C_{dc2}. For simplification in the schematic representations, these capacitor sets are combined into a single entity. By analyzing all potential switching states depicted in Fig. 3-4 over a single switching cycle, an averaged model for the two IPOP 3LNPCIs can be established, represented by equation (3-1). In this equation, $d_{k,1}$, $d_{k,2}$, $d_{k,3}$ (for k = 1, 2, as shown in Fig. 3-4 (a)) denote the duty ratios for the various switching states, with the notation (*)′ signifying the time derivative of (*).

The model derived in (3-1) highlights the complexity inherent in the IPOP 3LNPCIs system. A notable aspect of this model is the inclusion of an extra constraint equation (6) in (3-1), stemming from the fixed electric potentials at both the DC input and AC output sides of the two 3LNPCIs due to the IPOP configuration. Moreover, the discrepancy between positive and negative currents necessitates separate modeling for the filters and line resistances associated with each pole, further adding to the model's intricacy.

$$
\begin{cases}
(d_{11}R_{i1}^{+} + d_{13}R_{i1}^{-})i_1^{+} + L_1^{+}(i_1^{+})' + L_1^{-}(i_1^{-})' + (d_{11} + d_{13})R_{n1}i_1^{-} \\
\quad + v_{o1} = d_{11}V_1 - d_{13}V_2 & (1) \\
(i_1^{+} - C_1(v_{o1})')R_{o1}^{+} + (i_1^{-} - C_1(v_{o1})')R_{o1}^{-} + (i_1^{+} - C_1(v_{o1})' \\
\quad + i_2^{+} - C_2(v_{o2})')R = v_{o1} & (2) \\
(d_{21}R_{i2}^{+} + d_{23}R_{i2}^{-})i_2^{+} + L_2^{+}(i_2^{+})' + L_2^{-}(i_2^{-})' + (d_{21} + d_{23})R_{n2}i_2^{-} \\
\quad + v_{o2} = d_{21}V_1 - d_{23}V_2 & (3) \\
(i_2^{+} - C_2(v_{o2})')R_{o2}^{+} + (i_2^{-} - C_2(v_{o2})')R_{o2}^{-} + (i_1^{+} - C_1(v_{o1})' \\
\quad + i_2^{+} - C_2(v_{o2})')R = v_{o2} & (4) \\
i_1^{+} + i_2^{+} = i_1^{-} + i_2^{-} & (5) \\
(d_{11}R_{i1}^{+} + d_{12}R_{n1} + d_{13}R_{i1}^{-})i_1^{+} - d_{12}R_{n1}i_1^{-} + L_1^{+}(i_1^{+})' + (i_1^{+} - C_1(v_{o1})')R_{o1}^{+} \\
\quad = (d_{21}R_{i2}^{+} + d_{22}R_{n2} + d_{23}R_{i2}^{-})i_2^{+} - d_{22}R_{n2}i_2^{-} + L_2^{+}(i_2^{+})' \\
\quad + (i_2^{+} - C_2(v_{o2})')R_{o2}^{+} + d_{11}(d_{22} + d_{23})V_1 + d_{23}(d_{11} + d_{12})V_2 \\
\quad - [d_{21}(d_{12} + d_{13})V_1 + d_{13}(d_{21} + d_{22})V_2] & (6)
\end{cases}
\tag{3-1}
$$

3.2.2 Analysis

Building upon the model established in Subsection 3.2.1, this segment delves into a quantitative exploration of the currents within IPOP 3LNPCIs. Employing open-loop control for the IPOP 3LNPCIs enables a detailed examination of various factors affecting the currents. To facilitate a numerical analysis, system parameters are set as per the specifications listed in Table 3-1.

For a clear illustration of how impedances on the DC and AC sides influence the currents, it's assumed that the duty ratios for both 3LNPCIs are identical. This assumption simplifies the analysis by eliminating variations in switching behavior as a factor, allowing for a focused investigation into the impact of impedance disparities. This approach aids in isolating and understanding the specific effects of DC and AC side impedances on the CCs within the IPOP 3LNPCI configuration, providing valuable insights into the operational characteristics of these systems.

Table 3-1 Rated system parameters of two IPOP 3LNPCIs

Parameters	Rated Value
V_{dc}	2000 V
C_{dc1}, C_{dc2}	10 mF
R	5 Ω
D	0.3
ω	100π rad/s
R_{i1}^{+}, R_{i1}^{-}, R_{n1}, R_{i2}^{+}, R_{i2}^{-}, R_{n2}	0.01Ω, 0.01Ω, 0.02Ω, 0.01Ω, 0.01Ω, 0.02Ω
L_1^{+}, L_1^{-}, L_2^{+}, L_2^{-}	1 mH, 1 mH, 1 mH, 1 mH
C_1, C_2	4 mF, 4 mF
R_{o1}^{+}, R_{o1}^{-}, R_{o2}^{+}, R_{o2}^{-}	0.01Ω, 0.01Ω, 0.01Ω, 0.01Ω

Taking into account that the modulation signal approaches a sinusoidal waveform in steady-state conditions, the configuration of the modulation signals can be established as follows: $d_{11}= d_{21}=D\sin\omega t$, $d_{12}= d_{22}=1\text{-}D\sin\omega t$, $d_{13}= d_{23}=0$ for the positive half line cycle; on the other hand, for the negative half line cycle, $d_{13}= d_{23}=D(\sin\omega t+\pi) = -D\sin\omega t$, $d_{12}= d_{22}=1+D\sin\omega t$ and $d_{11}=d_{21}=0$.

Maintaining the essence of generality, one may posit that, $i_k^{+}=I_k^{+s}\sin\omega t+I_k^{+c}\cos\omega t$, $i_k^{-}=I_k^{-s}\sin\omega t+I_k^{-c}\cos\omega t$, $v_{o,k} = V_{o,k}^{s}\sin\omega t +V_{o,k}^{c}\cos\omega t$ (k = 1, 2) in the steady state.

Consequently, the steady equations for both the positive and negative half cycles can be formulated and amalgamated to derive the comprehensive steady-state equations for the entire cycle, denoted as (3-2) - (3-5). Specifically, (3-2) can be derived from (1) and (3) in (3-1), (3-3) from (2) and (4) in (3-1), (3-4) from (5) in (3-1), (3-5) from (6) in (3-1).

$$
\begin{aligned}
&(\omega L_k^+ I_k^{+s} + \omega L_k^- I_k^{-s} + V_{o,k}^c)\cos\omega t - (\omega L_k^+ I_k^{+c} + \omega L_k^- I_k^{-c} - V_{o,k}^s + DV_k)\sin\omega t \\
&\quad + D(R_{ik}^+ - R_{ik}^-) I_k^{+s} \sin^2 \omega t + D(R_{ik}^+ - R_{ik}^-) I_k^{+c} \sin\omega t \cdot \cos\omega t = 0
\end{aligned}
\tag{3-2}
$$

$$
\begin{aligned}
&[(I_k^{+c} - \omega C_k V_{o,k}^s) R_{o,k}^+ + (I_k^{-c} - \omega C_k V_{o,k}^s) R_{o,k}^- + (I_1^{+c} - \omega C_1 V_{o,1}^s + I_2^{+c} - \omega C_2 V_{o,2}^s) R - V_{o,1}^c]\cos\omega t \\
&\quad + [I_k^{+s} + \omega C_k V_{o,k}^c] R_{o,k}^+ + (I_k^{-s} + \omega C_k V_{o,k}^c) R_{o,k}^- \\
&\quad + (I_1^{+s} + \omega C_1 V_{o,1}^c + I_2^{+s} + \omega C_2 V_{o,2}^c) R - V_{o,1}^s]\sin\omega t = 0
\end{aligned}
\tag{3-3}
$$

$$
(I_1^{+c} + I_2^{+c} - I_1^{-c} - I_2^{-c})\cos\omega t + (I_1^{+s} + I_2^{+s} - I_1^{-s} - I_2^{-s})\sin\omega t = 0 \tag{3-4}
$$

$$
\begin{aligned}
&[\omega L_1^+ I_1^{+s} + R_{o,1}^+ I_1^{+c} - \omega C_1 R_{o,1}^+ V_{o,1}^s + R_{n1}(I_1^{+c} - I_1^{-c}) \\
&\quad - \omega L_2^+ I_2^{+s} - R_{o,2}^+ I_2^{+c} + \omega C_2 R_{o,2}^+ V_{o,2}^s - R_{n2}(I_2^{+c} - I_2^{-c})]\cos\omega t \\
&\quad + [-\omega L_1^+ I_1^{+c} + R_{o,1}^+ I_1^{+s} + \omega C_1 R_{o,1}^+ V_{o,1}^c + R_{n1}(I_1^{+s} - I_1^{-s}) \\
&\quad + \omega L_2^+ I_2^{+c} - R_{o,2}^+ I_2^{+s} - \omega C_2 R_{o,2}^+ V_{o,2}^c - R_{n2}(I_2^{+s} - I_2^{-s})]\sin\omega t \\
&\quad + D[(R_{i1}^+ - R_{i1}^-) I_1^{+s} + (R_{i2}^+ - R_{i2}^-) I_2^{+s}]\sin^2 \omega t \\
&\quad + D[(R_{i1}^+ - R_{i1}^-) I_1^{+c} + (R_{i2}^+ - R_{i2}^-) I_2^{+c}]\sin\omega t \cdot \cos\omega t = 0
\end{aligned}
\tag{3-5}
$$

To ensure the validity of (3-2) – (3-5) at any given time *t*, it's essential that the coefficients of the trigonometric functions within these equations equate to zero. By setting these coefficients to zero, the system of equations becomes solvable for the unknown variables I_k^{+s}, I_k^{+c}, I_k^{-s}, I_k^{-c}, $V_{o,k}^s$ and $V_{o,k}^c$. Moreover, the output currents can be calculated through:

$$
i_{o,k}^+ = i_k^+ - C_k \frac{dv_{o,k}}{dt}, \quad i_{o,k}^- = i_k^- - C_k \frac{dv_{o,k}}{dt}. \tag{3-6}
$$

Based on (3-2) – (3-6), the particular currents during steady states, as affected by variations in impedances on both the AC and DC sides, can be thoroughly computed and scrutinized.

1) The Influence of Asymmetric Impedances in the AC Side on Currents:

This part studies the influence of inequality of two poles' impedances in the AC side. In this situation, one may posit that the resistances in the DC side are equal, i.e., $R_{i1}^+ = R_{i1}^-$, $R_{i2}^+ = R_{i2}^-$ and $R_{n1} = R_{n2}$. Building on the proposed assumption, the quadratic terms in (3-2) (i.e., the last line) and (3-5) (i.e., the last two lines) can be eliminated. Consequently, the unknown variables can be solved out by setting the coefficients of trigonometric functions in (3-2)-(3-5) as zero as delineated in (3-7). As a result, the currents in steady scenarios can be solved out after some calculations.

In the context of (3-7), a set of twelve independent constraints emerges with k = 1, 2, providing a foundational basis for subsequent analyses, and there are 12 unknown variables (I_k^{+s}, I_k^{+c}, I_k^{-s}, I_k^{-c}, $V_{o,k}^s$, $V_{o,k}^c$ | k = 1, 2), hence, a unique solution to this equation set is ascertainable, affirming the efficacy of the underlying assumption. Therefore, it can be said that i_k^+, i_k^-, $v_{o,k}$ (k = 1, 2) merely consist of fundamental-frequency elements. Furthermore, the specific values of currents can be obtained utilizing (3-6) and (3-7).

$$\begin{cases}
\omega L_k^+ I_k^{+s} + \omega L_k^- I_k^{-s} + V_{o,k}^c = 0 & (1) \\
\omega L_k^+ I_k^{+c} + \omega L_k^- I_k^{-c} - V_{o,k}^s + DV_1 = 0 & (2) \\
(I_k^{+c} - \omega C_k V_{o,k}^s) R_{o,k}^+ + (I_k^{-c} - \omega C_k V_{o,k}^s) R_{o,k}^- & \\
\quad + (I_1^{+c} - \omega C_1 V_{o,1}^s + I_2^{+c} - \omega C_2 V_{o,2}^s) R - V_{o,k}^c = 0 & (3) \\
(I_k^{+s} + \omega C_k V_{o,k}^c) R_{o,k}^+ + (I_k^{-s} + \omega C_k V_{o,k}^c) R_{o,k}^- & \\
\quad + (I_1^{+s} + \omega C_1 V_{o,1}^c + I_2^{+s} + \omega C_2 V_{o,2}^c) R - V_{o,k}^s = 0 & (4) \\
I_1^{+c} + I_2^{+c} - I_1^{-c} - I_2^{-c} = 0 & (5) \\
I_1^{+s} + I_2^{+s} - I_1^{-s} - I_2^{-s} = 0 & (6) \\
\omega L_1^+ I_1^{+s} + R_{o,1}^+ I_1^{+c} - \omega C_1 R_{o,1}^+ V_{o,1}^s + R_{n1}(I_1^{+c} - I_1^{-c}) - \omega L_2^+ I_2^{+s} & \\
\quad - R_{o,2}^+ I_2^{+c} + \omega C_2 R_{o,2}^+ V_{o,2}^s - R_{n2}(I_2^{+c} - I_2^{-c}) = 0 & (7) \\
-\omega L_1^+ I_1^{+c} + R_{o,1}^+ I_1^{+s} + \omega C_1 R_{o,1}^+ V_{o,1}^c + R_{n1}(I_1^{+s} - I_1^{-s}) + \omega L_2^+ I_2^{+c} & \\
\quad - R_{o,2}^+ I_2^{+s} - \omega C_2 R_{o,2}^+ V_{o,2}^c - R_{n2}(I_2^{+s} - I_2^{-s}) = 0 & (8)
\end{cases} \tag{3-7}$$

Moreover, the variations in CCs within a single 3LNPCI, along with the discrepancies in current sharing ($i_{o1}^+ - i_{o2}^+$, $i_{o1}^- - i_{o2}^-$) in response to alterations in the inductances of 3LNPCI#1, are illustrated in Fig. 3-5 (a). Here, L_1^++L_1^-=2 mH, but their ratio L_1^-/L_1^+ varies from 0.4 to 1, and the other settings are summarized in Table 3-1. As observed from the results, as the asymmetry between two pole's inductances on the AC side intensifies, both the CCs and discrepancies in current sharing will escalate, despite their aggregate remaining equivalent to that of 3LNPCI#2. For Fig. 3-5 (b), a similar conclusion can be reached. Moreover, the outcomes suggest that the control strategy for IPOP 3LNPCIs encompasses two components: the eradication of CCs within an individual 3LNPCI and the precise proportional distribution of current among different 3LNPCIs, thereby adding complexity to the associated control method.

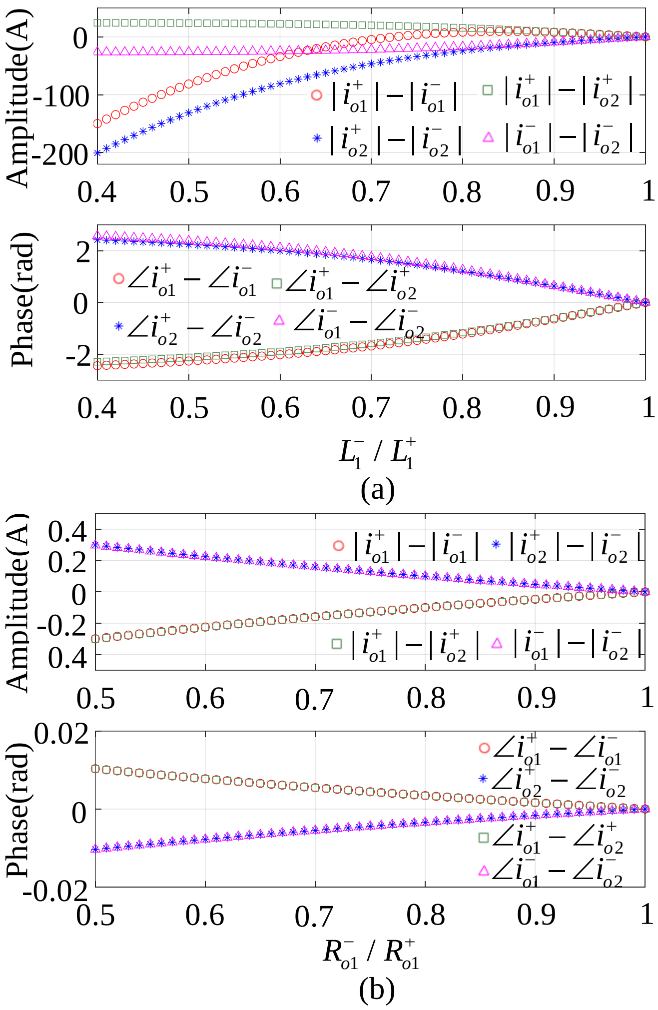

Fig. 3-5. Theoretical calculating results of currents accompanied by variations in line impedances. (a) L_1^++L_1^-=2 mH but L_1^-/L_1^+ varies from 0.4 to 1. (b) R_{o1}^++R_{o1}^-= 0.02 Ω but R_{o1}^-/R_{o1}^+ varies from 0.5 to 1.

2) The Influence of Asymmetric Resistances in the DC Side on Currents:

In this segment, the effects stemming from asymmetric resistances on the DC side are examined, with the premise that two poles' impedances on the AC side remain equal. That is, $L_1^+ = L_1^-$, $L_2^+ = L_2^-$, and $R_{o1}^+ = R_{o1}^-$, $R_{o2}^+ = R_{o2}^-$.

Firstly, if $R_{i1}^+ \neq R_{i1}^-$, $R_{i2}^+ \neq R_{i2}^-$, the bold quadratic terms in (3-2) and (3-5) cannot be eradicated and can be converted into (8) and (9):

$$\begin{aligned}&-(R_{ik}^{+}-R_{ik}^{-})I_{k}^{+s}+(R_{ik}^{+}-R_{ik}^{-})I_{k}^{+s}\cos 2\omega t\\&\qquad+(R_{ik}^{+}-R_{ik}^{-})I_{k}^{+c}\sin 2\omega t=0,\end{aligned}\tag{3-8}$$

$$\begin{aligned}&-[(R_{i1}^{+}-R_{i1}^{-})I_{1}^{+s}+(R_{i2}^{+}-R_{i2}^{-})I_{2}^{+s}]+\\&[(R_{i1}^{+}-R_{i1}^{-})I_{1}^{+s}+(R_{i2}^{+}-R_{i2}^{-})I_{2}^{+s}]\cos 2\omega t\\&+[(R_{i1}^{+}-R_{i1}^{-})I_{1}^{+c}+(R_{i2}^{+}-R_{i2}^{-})I_{2}^{+c}]\sin 2\omega t=0,\end{aligned}\tag{3-9}$$

which will generate new constraint equations. Combining (3-7), there will be 21 constraint equations but only 12 independent variables, making this set of equations no solutions. That is, the assumption that $i_k^{+}=I_k^{+s}\sin\omega t+I_k^{+c}\cos\omega t$, $i_k^{-}=I_k^{-s}\sin\omega t+I_k^{-c}\cos\omega t$, $v_{o,k}=V_{o,k}^{s}\sin\omega t+V_{o,k}^{c}\cos\omega t$ is invalid, and i_k^{+}, i_k^{-}, v_{ok} (k = 1, 2) include extra frequency components in addition to the fundamental-frequency element. It is only under these conditions that equations (3-2)-(3-5) are valid. Referring to (3-8) and (3-9), it becomes evident that the asymmetry between positive and negative resistances on the DC side primarily contributes to the DC and double-frequency values within the CCs and current sharing discrepancies.

Moreover, the impact of neutral line resistance R_{n1} and R_{n2} can be scrutinized by equations in sub-equations (7) and (8) in (3-7). If $R_{n1}\neq R_{n2}$, the fundamental-frequency current will be predominantly generated in CCs and current sharing discrepancies. Consequently, under typical circumstances, the CCs and current sharing discrepancies resulting from the asymmetry in DC side resistances will encompass DC, fundamental-frequency, and double-frequency elements.

To validate the accuracy of the preceding analytical examination, simulation outcomes are showcased in Fig. 3-6. These simulation results elucidate that the CCs and discrepancies in current sharing, attributable to the uneven distribution of resistances on the DC side, comprise components at DC, fundamental frequency, and double frequency. The waveforms generated from these simulations align with the theoretical predictions made earlier, affirming the reliability of the analytical model and its interpretations. This concordance between theoretical analysis and simulation outcomes is crucial for establishing the credibility of the findings and ensuring that the proposed models accurately reflect the real-world behavior of the IPOP 3LNPCIs under the influence of impedance asymmetries.

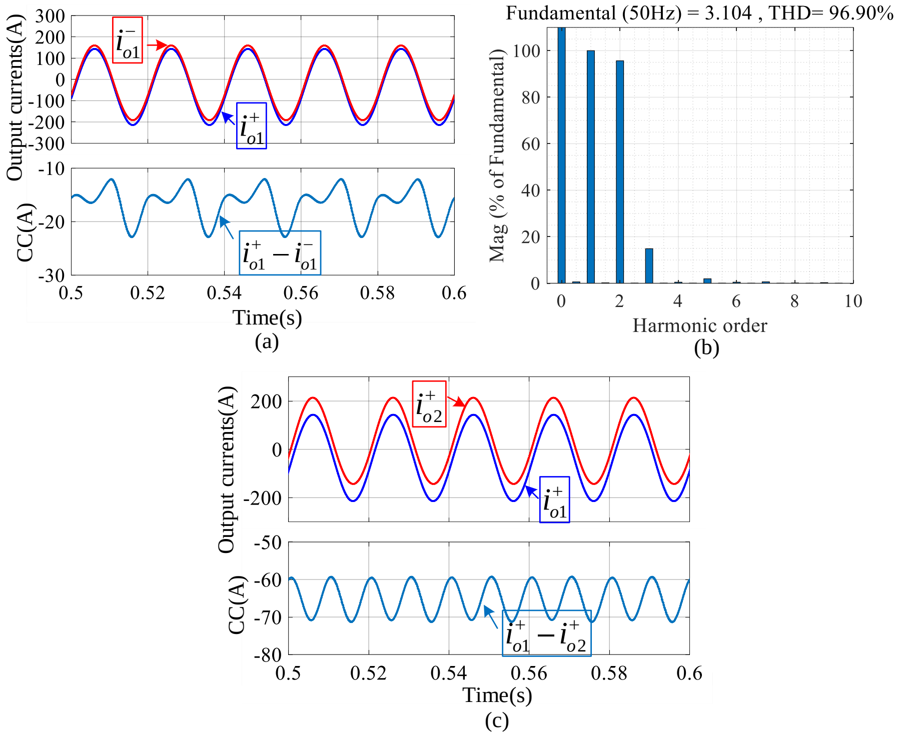

Fig. 3-6. Simulation waveforms when R_{i1}^{+}=18 mΩ, R_{i1}^{-}=2 mΩ, R_{n1}=22 mΩ and R_{n2}=18 mΩ. (a) i_{o1}^{+}, i_{o1}^{-} and their difference i_{o1}^{+}- i_{o1}^{-}. (b) Harmonic components of i_{o1}^{+}- i_{o1}^{-}. (c) i_{o1}^{+}, i_{o2}^{+} and their difference i_{o1}^{+}- i_{o2}^{+}.

C) Limitations in Suppressing CCs and Achieving Proportional Currents Sharing of the Conventional Topology

In this section, the constraints of the traditional 3LNPCI in addressing multi-objective control challenges are scrutinized through a proof by contradiction. This method involves assuming that the conventional 3LNPCI can simultaneously accomplish CC suppression and current sharing control. The analysis then seeks to demonstrate that this assumption leads to a contradiction, thereby proving it false.

In a steady-state scenario, it is presumed that there are duty ratios capable of simultaneously fulfilling both control objectives and let $i_1^+ = i_1^- = i_2^+ = i_2^- = I^s \sin\omega t + I^c \cos\omega t$, $v_{o1} = v_{o2} = V^s \sin\omega t + V^c \cos\omega t$. Adhering to the modulation scheme of the 3LNPCI, the steady-state equations for the positive half-line cycle can be deduced from equation (3-1) and are presented as

$$
\begin{cases}
(L_1^+ + L_1^-)[\omega I^s \cos\omega t - \omega I^c \sin\omega t] + V_o^s \sin\omega t + V_o^c \cos\omega t \\
\quad + d_{11}(R_{i1}^+ + R_{n1})(I^s \sin\omega t + I^c \cos\omega t) = d_{11}V_1 \\
(L_2^+ + L_2^-)[\omega I^s \cos\omega t - \omega I^c \sin\omega t] + V_o^s \sin\omega t + V_o^c \cos\omega t \\
\quad + d_{21}(R_{i2}^+ + R_{n2})(I^s \sin\omega t + I^c \cos\omega t) = d_{21}V_1 \\
L_1^+(\omega I^s \cos\omega t - \omega I^c \sin\omega t) + (d_{11}R_{i1}^+ + R_{o1}^+)(I^s \sin\omega t + I^c \cos\omega t) \\
\quad - R_{o1}^+ C_1(\omega V^s \cos\omega t - \omega V^c \sin\omega t) = \\
L_2^+(\omega I^s \cos\omega t - \omega I^c \sin\omega t) + (d_{21}R_{i2}^+ + R_{o2}^+)(I^s \sin\omega t + I^c \cos\omega t) \\
\quad - R_{o2}^+ C_2(\omega V^s \cos\omega t - \omega V^c \sin\omega t) + d_{11}(1-d_{21})V_1 - d_{21}(1-d_{11})V_1
\end{cases}
\tag{3-10}
$$

The analysis of (3-10) reveals a fundamental limitation in the control capabilities of the conventional 3LNPCI. Specifically, (3-10) presents a scenario with only two independent unknown variables, d_{11} and d_{21}, against the backdrop of three constraint equations. This discrepancy indicates that it is not feasible to find numerical solutions for the duty ratios that would satisfy all constraints under general conditions, where line impedances and the current I are arbitrary. This limitation holds true for both the positive and negative half-cycles of the line current. The conclusion drawn from this analysis invalidates the initial assumption that the conventional 3LNPCI can simultaneously manage CC suppression and current sharing among inverters.

The root of this limitation lies in the inherent design of the conventional 3LNPCIs, which, as depicted in Fig. 3-3, possess only a single degree of modulation freedom. This singular degree of freedom is insufficient for addressing the dual objectives of CC suppression and equitable current sharing, underscoring a significant constraint in the design and operational strategy of traditional 3LNPCIs.

This finding highlights the need for innovative approaches in inverter design and control strategies that can offer additional degrees of freedom, thereby enabling the simultaneous achievement of these critical control objectives in power electronics systems.

3.3 The Modified Topology and Proposed Control Strategy for IPOP 3LNPCIs

To address the inherent constraints of the conventional 3LNPCIs, this chapter introduces an enhanced topology for the 3LNPCI that expands its modulation freedom. This modification is pivotal in overcoming the previously identified limitations, particularly the inability to simultaneously achieve CC suppression and appropriate current sharing among inverters. Alongside the introduction of this modified topology, a novel control method tailored to this enhanced design is also presented within this chapter. This control strategy is specifically developed to leverage the additional modulation capabilities introduced by the modified topology, ensuring that both CC suppression and current sharing can be effectively managed.

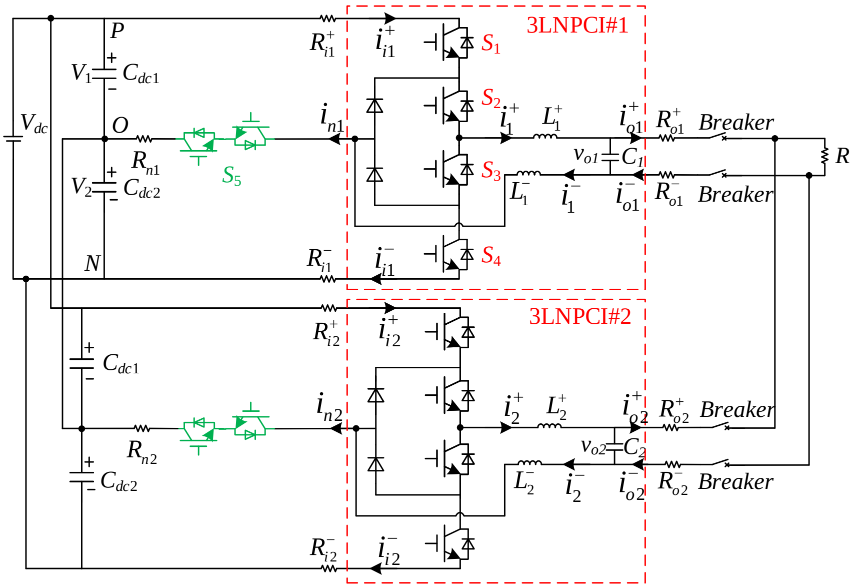

Fig. 3-7. The modified topology of 3LNPCIs connected in IPOP form.

3.3.1 Description of Modified Topology of 3LNPCI

Fig. 3-7 illustrates the enhanced topology of the 3LNPCI, which introduces a notable alteration to the conventional design depicted in Fig. 3-1. The key modification involves the incorporation of a bidirectional switch, labeled S_5, into the neutral line on the DC side of the inverter. This addition fundamentally expands the inverter's operational capabilities, as outlined by the following basic modulation principles:

With S_5 Activated (ON): In this state, the modified 3LNPCI functions identically to its conventional counterpart, adhering to the standard modulation strategies previously established for the traditional 3LNPCI design.

With S_5 Deactivated (OFF): This condition initiates a distinct operational mode where switches S_1 and S_4 are concurrently turned OFF, while S_2 and S_3 are engaged (turned ON) simultaneously.

The introduction of S_5 effectively augments the modulation flexibility of the 3LNPCI, offering an additional degree of control. This enhancement is crucial as it enables the simultaneous realization of dual control objectives: the suppression of CCs and the maintenance of balanced current sharing among parallel inverters. The strategic inclusion of the bidirectional switch S_5 not only diversifies the possible switching states but also paves the way for more sophisticated control algorithms capable of exploiting this increased modulation freedom to address complex control challenges within power electronics systems.

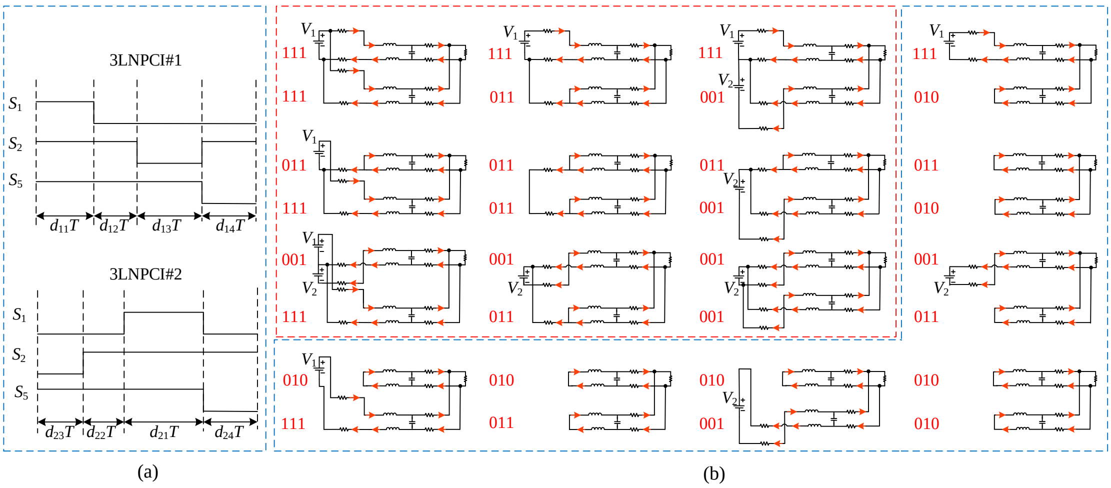

Fig. 3-8. Switching states of two IPOP modified 3LNPCIs. (a) Sketches of duty ratios. (b) Equivalent schematic diagrams under different switching combinations.

With the introduction of the modified topology in the 3LNPCIs, the operational dynamics of two IPOP modified 3LNPCIs become significantly more complex. This complexity is evidenced by an increase in the total number of operating states to 16, as detailed in Fig. 3-8. The depiction of circuits under various switching states, as illustrated in Fig. 3-8 (b), employs a three-digit notation corresponding to the states of switches S_1, S_2, and the newly added S_5, where "1" indicates the ON state and "0" the OFF state. The addition of switch S_5 introduces seven new switching states, which are highlighted within a blue dashed box in Fig. 3-8 (b). These states augment the inverter's operational flexibility, allowing for more nuanced control strategies that can address the dual objectives of CC suppression and current sharing more effectively. In contrast, the original nine switching states, associated with the conventional IPOP 3LNPCIs configuration, are encompassed within a red dashed box, underscoring the retained operational modes from the traditional setup. The comprehensive inclusion of all 16 operating states enables the derivation of an averaged model for the switch cycle, represented as (3-11), where d_{k1}, d_{k2}, d_{k3} and d_{k4} (k = 1, 2, see Fig. 3-8 (a)) are the duty ratios of the relevant switching states, and (*)′ demotes the derivative of (*). This model encapsulates the intricate dynamics of the modified IPOP 3LNPCIs system, offering a foundational framework for analyzing and optimizing the inverter's performance in light of the increased modulation freedom provided by the modified topology.

$$\begin{cases} (d_{k1}R_{k1}^{+} + d_{k3}R_{k1}^{-})i_k^{+} + L_k^{+}(i_k^{+})' + L_k^{-}(i_k^{-})' \\ \quad + (d_{k1} + d_{k3})R_{nk}i_k^{-} + v_{ok} = d_{k1}V_1 - d_{k3}V_2 \\ (i_k^{+} - C_k(v_{ok})')R_{ok}^{+} + (i_k^{-} - C_k(v_{ok})')R_{ok}^{-} \\ \quad + (i_1^{+} - C_1(v_{o1})' + i_2^{+} - C_2(v_{o2})')R = v_{ok} \\ i_1^{+} + i_2^{+} = i_1^{-} + i_2^{-} \\ [d_{11}R_{i1}^{+} + d_{12}(1-d_{24})R_{n1} + d_{13}R_{i1}^{-}]i_1^{+} + [d_{11}d_{24} \\ \quad + d_{12}(1-d_{24}) + d_{13}d_{24}]R_{n1}i_1^{-} + [L_1^{+}(i_1^{+})' + (i_1^{+} - C_1(v_{o1})')R_{o1}^{+}] \\ \quad + [d_{24}(1-d_{14}) + d_{14}][L_1^{-}(i_1^{-})' + (i_1^{-} - C_1(v_{o1})')R_{o1}^{-}] = \\ \quad [d_{21}R_{i2}^{+} + d_{22}(1-d_{14})R_{n2} + d_{23}R_{i2}^{-}]i_2^{+} + [d_{14}d_{21} - d_{22}(1-d_{14}) \\ \quad + d_{14}d_{23}]R_{n2}i_2^{-} + [L_2^{+}(i_2^{+})' + (i_2^{+} - C_2(v_{o2})')R_{o2}^{+}] \\ \quad + [d_{24}(1-d_{14}) + d_{14}][L_2^{-}(i_2^{-})' + (i_2^{-} - C_2(v_{o2})')R_{o2}^{-}] + \\ \quad d_{11}(1-d_{21})V_1 - d_{21}(1-d_{11})V_1 - d_{13}(1-d_{23})V_2 + d_{23}(1-d_{13})V_2 \end{cases} \tag{3-11}$$

Likewise, in the steady-state condition, it is assumed that there are existing duty ratios capable of concurrently meeting the two specified control objectives and letting $i_1^{+} = i_1^{-} = i_2^{+} = i_2^{-} = I^s\sin\omega t + I^c\cos\omega t$, $v_{o1} = v_{o2} = V^s\sin\omega t + V^c\cos\omega t$, the steady-state equations can be derived as (3-12) from (3-11) for the positive half line cycle.

$$
\begin{cases}
(L_1^+ + L_1^-)[\omega I^s \cos\omega t - \omega I^c \sin\omega t] \\
\quad + d_{11}(R_{i1}^+ + R_{n1})(I^s \sin\omega t + I^c \cos\omega t) + V_o^s \sin\omega t + V_o^c \cos\omega t = d_{11}V_1 \\
(L_2^+ + L_2^-)[\omega I^s \cos\omega t - \omega I^c \sin\omega t] \\
\quad + d_{21}(R_{i2}^+ + R_{n2})(I^s \sin\omega t + I^c \cos\omega t) + V_o^s \sin\omega t + V_o^c \cos\omega t = d_{21}V_1 \\
\{d_{11}R_{i1}^+ + [2d_{12}(1-d_{24}) + d_{11}d_{24}]R_{n1}\}(I^s \sin\omega t + I^c \cos\omega t) + \\
\quad \{L_1^+ + [d_{24}(1-d_{14}) + d_{14}]L_1^-\}(\omega I^s \cos\omega t - \omega I^c \sin\omega t) + \\
\quad \{R_{o1}^+ + [d_{24}(1-d_{14}) + d_{14}]R_{o1}^-\}(I^s \sin\omega t + I^c \cos\omega t - \omega C_1 V^s \cos\omega t \\
\quad + \omega C_1 V^c \sin\omega t) = [d_{21}R_{i2}^+ + d_{14}d_{21}R_{n2}](I^s \sin\omega t + I^c \cos\omega t) + \\
\quad \{L_2^+ + [d_{24}(1-d_{14}) + d_{14}]L_2^-\}(\omega I^s \cos\omega t - \omega I^c \sin\omega t) + \\
\quad \{R_{o2}^+ + [d_{24}(1-d_{14}) + d_{14}]R_{o2}^-\}(I^s \sin\omega t + I^c \cos\omega t - \omega C_2 V^s \cos\omega t \\
\quad + \omega C_2 V^c \sin\omega t) + d_{11}(1-d_{21})V_1 - d_{21}(1-d_{11})V_1 \\
\quad - d_{13}(1-d_{23})V_2 + d_{23}(1-d_{13})V_2
\end{cases}
\tag{3-12}
$$

Equation (3-12) highlights a significant advantage of the modified 3LNPCI topology over its conventional counterpart. The equation reveals that in the current system configuration, the count of independent variables not yet determined surpasses the quantity of available constraints. This condition is not only applicable for the positive half of the line cycle but also remains true for the negative half, indicating a consistent increase in the system's degrees of freedom across the entire operation range. This surplus of independent variables relative to constraints is a clear indication that the modified 3LNPCI topology is inherently more flexible and adaptable than the traditional design. This increased modulation freedom is crucial as it opens up the possibility of simultaneously achieving two pivotal control objectives. The ability of (3-12) to hold under any given set of line impedances and current I signifies that the modified 3LNPCI can be effectively tuned to meet specific operational requirements, irrespective of the external electrical environment or the demands placed on the system. This adaptability makes the modified 3LNPCI a promising solution for achieving two control objectives simultaneously.

3.3.2 Proposed Control Scheme of the Modified 3LNPCI

The control strategy for the modified 3LNPCI is meticulously designed to simultaneously address CC suppression and ensure proportional current sharing among inverters. Fig. 3-9 delineates the comprehensive control scheme, which is fundamentally anchored on two distinct degrees of control freedom.

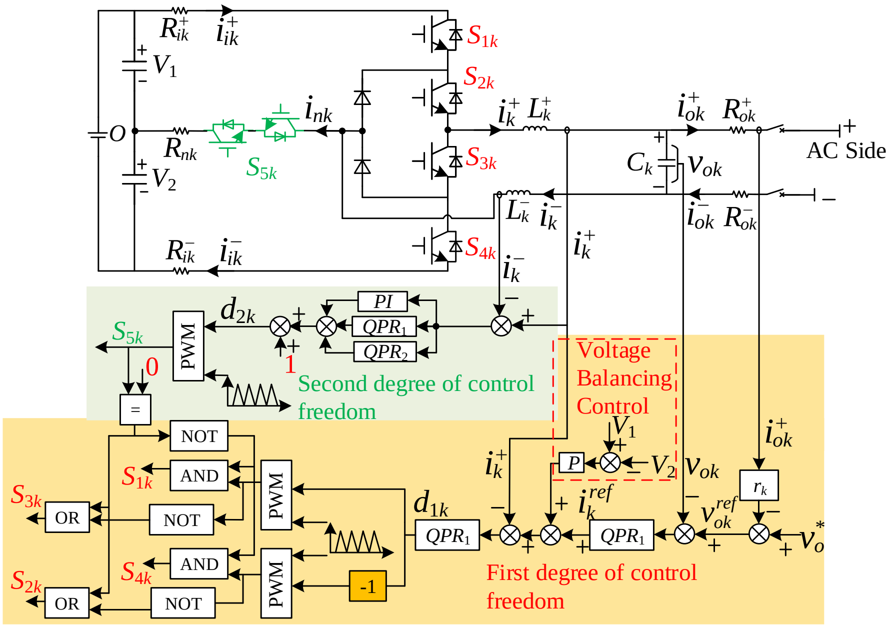

Fig. 3-9. The whole control method of the modified 3LNPCI.

The first degree of control leverages a droop-based approach, focusing on the modulation of duty ratios for the active switches (S_1-S_4). This aspect of the control scheme is pivotal for achieving appropriate current distribution across multiple 3LNPCIs in accordance with predetermined proportions. The droop-based control is structured in two hierarchical layers:

Outer Loop (Droop Control): This layer employs conventional droop control techniques to facilitate current sharing among the various 3LNPCIs. Droop control, by adjusting the voltage in response to changes in load current, indirectly influences current distribution, ensuring that each inverter carries its fair share of the total load. This is crucial for maintaining system stability and preventing overloading of individual inverters.

Inner Loop (Dual-Loop Control): At this level, a more refined control mechanism is implemented, often referred to as dual-loop control. This involves a fast inner loop for current control, complemented by a slower outer loop typically focused on voltage regulation. The inner loop's primary function is to ensure accurate current tracking, allowing the inverter to respond swiftly to changes in the load or other system parameters, thereby enhancing the precision and responsiveness of the overall control strategy.

The outer loop is designed as

$$v_{o,k}^{ref} = v_o^* - r_k \cdot i_{o,k}^+, \tag{3-13}$$

where k = 1, 2 represents two 3LNPCIs, $v_{o,k}^{\mathrm{ref}}$ represents the reference voltage value for the inner control loop, v_o^* is the defined AC output voltage magnitude. r_k is the droop gain, $i_{o,k}^+$ is the positive output current of the H-bridge inverter.

The inner control loop is based on the fundamental-frequency quasi-PR controller, namely QPR1 and its control functions are designed as,

$$\begin{cases} i_k^{ref} = (k_{VP1} + \dfrac{2k_{VR1}\omega_c s}{s^2 + 2\omega_c s + \omega_0^2})(v_{o,k}^{ref} - v_{o,k}) \\ d_{1,k} = (k_{CP1} + \dfrac{2k_{CR1}\omega_c s}{s^2 + 2\omega_c s + \omega_0^2})(i_k^{ref} - i_k^+) \end{cases}, \tag{3-14}$$

where $d_{1,k}$ is the modulation signal of S_1-S_4, k_{VP1}, k_{VR1} and k_{CP1}, k_{CR1} serve as the proportional and resonant parameters for the voltage and current controllers, respectively, and ω_0 denotes the base frequency, while ω_c represents the cut-frequency.

Furthermore, a voltage balancing controller is integrated into the system. This additional component is crucial for maintaining equilibrium between the voltages V_1 and V_2, which are essential for the stable operation of the inverter and the quality of its output. The voltage balancing controller operates by introducing an offset voltage to correct any imbalances between V_1 and V_2. The generation of this offset signal is accomplished using a proportional controller, a straightforward yet effective control mechanism that adjusts the offset voltage in direct proportion to the voltage imbalance. The proportional controller's simplicity ensures fast response times and ease of implementation, making it a suitable choice for real-time voltage balancing in power electronics applications.

Building upon the first degree of control freedom, which enables proportional load power sharing among multiple 3LNPCIs, the second degree of control freedom specifically targets the elimination of CCs within each individual 3LNPCI. Despite achieving proportional current sharing by the first degree of control freedom, the inherent issue of CCs within a single inverter persists, necessitating further control measures. To address this, the second degree of control freedom is implemented through the modulation of the switching tube S_5, as depicted in Fig. 3-9. The control mechanism involves monitoring the discrepancy between the positive and negative currents in kth 3LNPCI (denoted as $i_k^+ - i_k^- (= i_{o,k}^+ - i_{o,k}^-)$), which is indicative of the presence of CCs. This current difference is then fed into a trio of controllers tasked with adjusting the duty cycle of S_5 to mitigate the CCs. The control strategy incorporates the internal model principle [101], which posits that to effectively track or suppress a given signal, the controller must embody the dynamic model of that signal. Adhering to this principle, the control framework comprises three distinct controllers tailored to different components of the current discrepancy:

PI Controller: Aimed at suppressing the DC component of CCs, this controller applies PI control to mitigate steady-state errors. Quasi-PR (QPR) Controllers: Two Quasi-Proportional Resonant controllers are employed to address the AC components of CCs: QPR1: Targets the fundamental-frequency component, effectively eliminating the CCs at the system's primary operating frequency. QPR2: Focuses on the double-frequency component, mitigating the CCs at twice the fundamental frequency.

This multi-controller approach, leveraging the unique capabilities of PI and Quasi-PR controllers, enables precise modulation of S_5 to counteract the various components of the CCs. By dynamically adjusting the operation of S_5 in response to the identified discrepancies, the second degree of control freedom facilitates the effective elimination of CCs within each 3LNPCI, enhancing the system's overall performance and stability. The controller is designed as,

$$\begin{aligned} d_{2,k} &= 1 + [(k_P + \frac{k_I}{s}) + (k_{P1} + \frac{2k_{R1}\omega_c s}{s^2 + 2\omega_c s + \omega_0^2}) \\ &+ (k_{P2} + \frac{2k_{R2}\omega_c s}{s^2 + 2\omega_c s + 4\omega_0^2})](i_k^+ - i_k^-), \end{aligned} \tag{3-15}$$

where $d_{2,k}$ is the modulation value of added tube S_5, k_P and k_I are the proportional and integral gains of the PI controller, respectively, k_{P1}, k_{R1} and k_{P2}, k_{R2} are the proportional gains and resonant gains of QPR1 and QPR2, respectively, ω_0 is the base-frequency and ω_c is the cut-frequency.

The proposed CC suppression strategy for 3LNPCIs distinguishes itself by its efficiency and minimal computational demand. Unlike methods that might not incorporate a dedicated CC suppression approach, this strategy utilizes a streamlined set of controllers consisting of one PI controller, one Quasi-Proportional Resonant controller at the fundamental frequency (QPR1), and another at double frequency (QPR2) to generate the necessary modulation signal offset for CC mitigation. The computational simplicity of this approach is a significant advantage. The PI controller is well-known for its straightforward calculation, requiring only proportional and integral terms to adjust the control signal. The QPR controllers, while slightly more complex, are designed to specifically target and suppress the CCs at selected frequencies without introducing excessive computational overhead. The fact that these three controllers collectively require minimal processing power means that their implementation is well within the capabilities of commonly used digital signal processors (DSPs) in power electronics applications. In summary, the proposed CC suppression method achieves a significant improvement in system performance by effectively mitigating CCs with a minimal addition to computational load.

The principle behind suppressing CCs within a single 3LNPCI hinges on the strategic modulation of switch S_5, as informed by the control methodology detailed in equation (3-15). The operation of S_5 is closely tied to the relationship between two poles' currents within the 3LNPCI, denoted as i_k^+ and i_k^-, respectively. When the duty cycle $d_{2,k}$ is adjusted such that it equals 1 (or exceeds this value), it implies that the negative current i_k^- is either equal to or less than the positive current i_k^+, prompting S_5 to remain ON continuously. This condition ensures a direct path for current flow, maintaining the operational status quo of the inverter. Conversely, should i_k^- exceed i_k^+, $d_{2,k}$ will drop below 1, indicating that S_5 does not remain perpetually ON. In instances where S_5 is turned OFF, an alternate current path is established, linking the negative power line in series with the positive power line via the clamping diode and switches S_2/S_3. This configuration activates the switching states encapsulated within the blue dashed box in Fig. 3-8. The effect of this alternate path is to align two pole's currents, effectively "squeezing out" any excess current from the negative line and redistributing it to other 3LNPCIs where the negative current is less than the positive current. This dynamic adjustment ensures that two poles' currents within each 3LNPCI are balanced, thereby mitigating the internal CCs. This concept, rooted in the specific behavior of S_5 and the corresponding switching states, provides a robust mechanism for CC suppression within the 3LNPCI framework.

Moreover, this suppression technique, by virtue of its underlying principles, has the potential to be adapted and applied to other configurations of IPOP half-bridge inverters, extending its utility beyond the specific case of 3LNPCIs.

3.4 Experimental Tests

To ascertain the efficacy of the proposed enhanced topology and its associated control strategy for 3LNPCIs, experimental validation is essential. The configuration of the experimental apparatus, as depicted in Fig. 10, involves two 3LNPCIs configured in IPOP. This setup is designed to closely replicate real-world conditions, allowing for a comprehensive assessment of the system's performance under various operational scenarios.

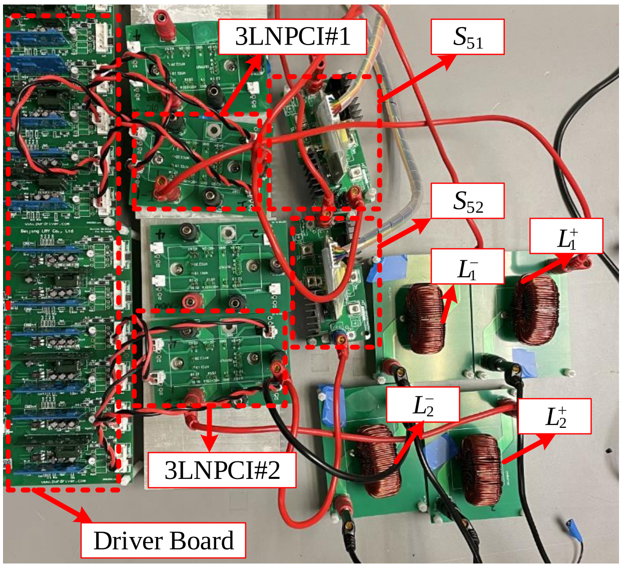

Fig. 3-10. Experimental setup.

The key objectives of these experiments include:

1. *CC Suppression*: Evaluating the system's ability to minimize or eliminate circulating currents within and between the inverters, which is critical for system stability and efficiency.

2. *Proportional Current Distribution*: Assessing the efficacy of the control strategy in distributing the load current proportionally among the inverters, ensuring that each inverter shares the load as intended, according to its capacity and the predefined sharing ratio.

3. *Voltage Balancing*: Verifying the voltage balancing controller's performance in maintaining equilibrium between the voltages across two different capacitors, which is essential for the proper functioning of the inverters.

The topology of two IPOP 3LNPCIs used in the experiments mirrors the configuration depicted in Fig. 3-7. The system operates with an input DC voltage of 220V, while the output AC voltage of a single phase is rated at an amplitude of 80V with a frequency of 50Hz. The modulation index employed is m = 0.727. On the AC side, the designated load resistance stands at R = 8Ω, equating to a power rating of 400W. The inverters switch at a frequency of 10kHz. To emulate the asymmetry in line resistance parameters, resistances R_{o1}^{+}= 0.1Ω, R_{o1}^{-}= 0.3Ω are utilized. The other system settings are listed in Table 3-2.

Table 3-2. Experimental system parameters

Parameters	Rated Value
C_{dc1}, C_{dc2}	1 mF
L_1^+, L_1^-, L_2^+, L_2^-	3 mH, 3 mH, 3 mH, 4 mH
C_1, C_2	2 μF, 2 μF
R_{o1}^{+}, R_{o1}^{-}, R_{o2}^{+}, R_{o2}^{-}	0.01Ω, 0.01Ω, 0.01Ω, 0.01Ω
Conventional 3LNPCI	10-FZ06NIA075SA-P926F33 (From Vincotech)
S_5	IPW60R070C6 (650V, R_{on} = 63 mΩ)
Parasitic resistance of the inductor	100 mΩ

3.4.1 Equal Power Sharing Ratio

The experimental waveforms depicted in Fig. 3-11 validate the effectiveness of the enhanced topology and its associated control strategy for two IPOP enhanced 3LNPCIs under a balanced power-distribution scenario (0.5:0.5 ratio). The key metrics monitored during the experiment include two poles' output currents of inverter#1 and the CC within inverter#1 ($i_{o1}^{+} - i_{o1}^{-}$), and the positive output current i_{o2}^{+}. The other currents can be deduced through Kirchhoff's Current Law and the monitored values.

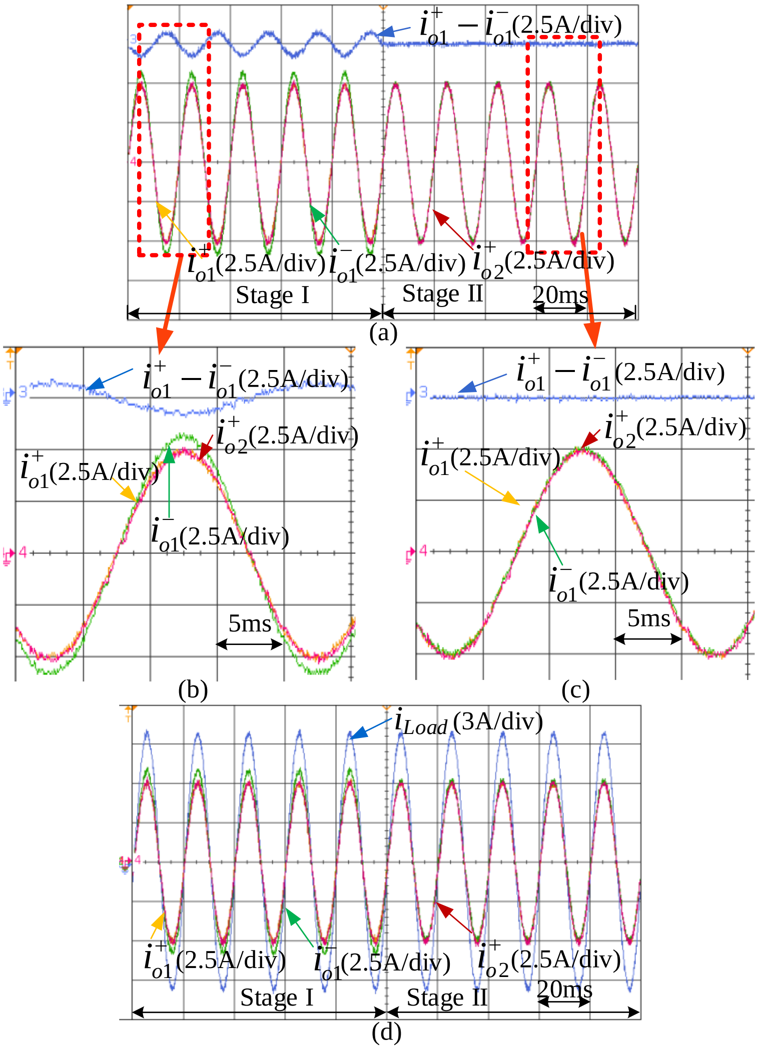

Fig. 3-11. Experimental results with equal power distribution ratio (0.5:0.5). (a) Whole results with different regulating elements are activated. (b) Expanded display of Stage I waveforms. (c) Expanded display of Stage II waveforms. (d) Currents' profiles.

Stage I Analysis (First Degree of Control Freedom Active, S_5 ON): During this initial stage, the control strategy focuses on proportional load sharing between the two inverters. Two poles' currents i_{o1}^{+} and i_{o2}^{+} are observed to be equal, indicating successful power sharing between 3LNPCI#1 and 3LNPCI#2. However, a discrepancy between the positive and negative currents within inverter#1 is noted, with a CC amplitude of approximately 0.75A. A similar CC magnitude is inferred for 3LNPCI#2, adhering to Kirchhoff's law.

Stage II Analysis (Second Control Component Activated, S_5 Modulated): This stage introduces the second control element, targeting the suppression of CC within each 3LNPCI by dynamically modulating S_5. The activation of this control level equalizes two poles' currents within inverter#1, significantly reducing the CC to less than 0.1A, thereby demonstrating effective CC suppression. The enlarged waveforms in Fig. 3-11 (b) and (c) offer a detailed view of the system's response during each control stage, illustrating the impact of the control strategies on current dynamics.

Load Current Profile (Fig. 3-11 (d)): The overall load current profile i_{Load} is consistently equivalent to the aggregate of the positive currents i_{o1}^{+} and i_{o2}^{+}, with an amplitude of 10A throughout the experiment. This consistency underscores the system's ability to maintain stable load current levels despite the dynamic modulation of control strategies. These experimental findings underscore the efficacy of the proposed modified topology and dual-degree control methodology in achieving balanced current sharing and effective CC suppression in IPOP 3LNPCIs.

3.4.2 Unequal Power Sharing Ratio

The experimental waveforms showcased in Fig. 3-12 demonstrate the adaptability and effectiveness of the enhanced topology and associated control strategy for two IPOP 3LNPCIs under an unequal power-distribution scenario (0.3:0.7 ratio). This setup tests the system's capability to manage more complex power distribution requirements.

Stage I (First Degree of Control Freedom Activated with S_5 ON): With only the first degree of control active, the system aims to achieve the targeted power-sharing ratio between the two inverters. The positive currents i_{o1}^{+} andi_{o2}^{+} are measured at 3A and 7A, respectively, aligning with the desired 0.3:0.7 power-sharing ratio, which confirms the effectiveness of the control strategy in managing unequal power distribution. Despite successful power sharing, a significant discrepancy between two poles' currents within inverter#1 is observed, resulting in a CC amplitude of approximately 2.6A, indicating a more pronounced CC issue under unequal power-sharing conditions.

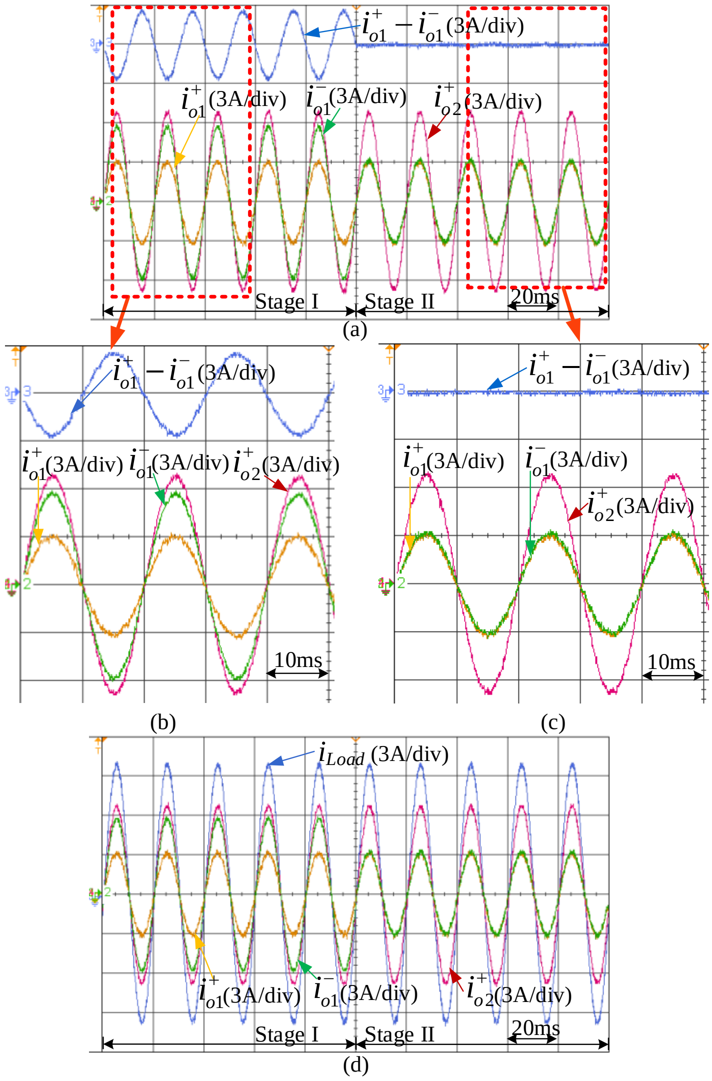

Fig. 3-12. Experimental results with unequal power distribution ratio (0.3:0.7). (a) Whole results with different regulating elements are activated. (b) Expanded display of Stage I waveforms. (c) Expanded display of Stage II waveforms. (d) Currents' profiles.

Stage II (Activation of CC Suppression Control): The second stage introduces the CC suppression control, focusing on minimizing the CC within each inverter by modulating S_5. The activation of this control significantly reduces the CC within 3LNPCI#1 to below 0.1A, demonstrating the control strategy's ability to effectively mitigate CCs even in scenarios of unequal power sharing. The enlarged waveforms in Fig. 3-12 (b) and (c) provide detailed insights into the system's response and the impact of the CC suppression control.

Load Current Profile (Fig. 3-12 (d)): In the whole experimental stage, the total load current profile i_{Load} consistently equals the sum of the positive currents i_{o1}^{+} and i_{o2}^{+}, with a total amplitude of 10A, underscoring the system's capacity to maintain stable load current levels irrespective of the power-sharing ratio and control strategy adjustments.

The performance of the designed control scheme for the enhanced 3LNPCIs is quantitatively summarized in Table 3-3, focusing on its effectiveness at a 400W operational level. Key performance indicators include the suppression of CCs and the total harmonic distortion (THD) of the inverters' currents, both of which are critical metrics for evaluating the efficiency and quality of power electronic systems. Observations from Table 3-3 reveal that the proposed control scheme significantly mitigates CCs within the IPOP 3LNPCIs setup. Moreover, the proposed strategy contributes to a noticeable reduction in the average THD of the output currents. The improvement in THD underscores the proposed control scheme's ability to not only manage CCs but also to enhance the overall quality of the output current.

Table 3-3. Performance of the proposed CC suppression scheme

Power sharing ratio	Without or with proposed scheme	Amplitude of CC	Average THD of output currents
0.5:0.5	Without	0.75A	2.5%
	With	<0.1A	2.0%
0.3:0.7	Without	2.6A	2.7%
	With	<0.1A	2.1%

Based on these experimental findings, it is illustrated that the robustness and flexibility of the proposed modified topology and dual-degree control approach in managing both equal and unequal power-sharing scenarios. The ability to maintain precise control over current sharing and effectively suppress CCs, as evidenced by the experiments, highlights the potential of the proposed solutions for a wide range of applications in power electronics systems, particularly in scenarios demanding intricate power management and high system stability.

3.4.3 Neutral Point Voltage Balance with Proposed Strategy

Maintaining the balance of the neutral point voltage is crucial for the stable and efficient operation of 3LNPCIs. An imbalanced neutral point voltage can lead to uneven voltage stresses on the switching devices, potentially causing premature failure and affecting the overall performance of the inverter. The proposed control scheme addresses this critical aspect by incorporating measures to ensure the neutral point voltage remains balanced, without compromising the inverter's capability to suppress CCs. Fig. 3-13 illustrates the effectiveness of this approach, demonstrating how the neutral point voltage can be maintained within desired thresholds even as the control strategy actively mitigates CCs. The ability to simultaneously balance the neutral point voltage and suppress CCs is a significant advantage of the proposed scheme, highlighting its comprehensive approach to inverter control.

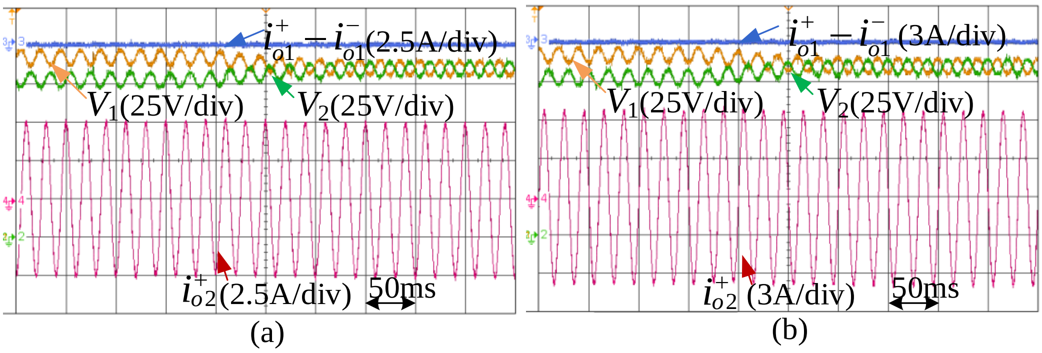

Fig. 3-13. Waveforms of neutral point voltage employing the suggested scheme. (a) Equal power distribution ratio (0.5:0.5). (b) Unequal power distribution ratio (0.3:0.7).

3.4.4 Efficiency Comparison

The efficiency analysis of two parallel conventional 3LNPCIs versus the proposed enhanced ones under varied operational scenarios—including various load capacities and ratios of power distribution—provides insight into the performance trade-offs associated with the modified topology. The overall losses in the parallel inverter system are primarily composed of active switch losses P_{loss_sw} and line losses P_{loss_line}.

Active Switch Losses (P_{loss_sw}): These losses are predominantly influenced by the number and operation of the active switches within the inverter topology. The modified 3LNPCI topology, by virtue of incorporating additional switches (i.e., the bidirectional switch S_5 to enhance control flexibility), inherently faces a disadvantage in terms of switch losses compared to the conventional topology. The extra switches introduce additional conduction and switching losses, which could potentially reduce the whole parallel inverter efficiency.

Line Losses (P_{loss_line}): The line losses are determined by the distribution of two poles' currents through the system and are mathematically related to the line resistance parameters R_{line}^{+}, R_{line}^{-}, and R_n. These losses can be expressed as a function of the current distribution and the resistances encountered by the currents in the circuit, that is, $P_{loss\_line} = (i^{+})^2 R_{line}^{+} + (i^{-})^2 R_{line}^{-} + (i_n)^2 R_n$. The modified 3LNPCI topology, coupled with its control strategy, has the potential to either mitigate or exacerbate these losses depending on the specific operational conditions and the values of the line resistances. The control strategy's ability to balance positive and negative currents and to suppress CCs can lead to a reduction in line losses under certain conditions.

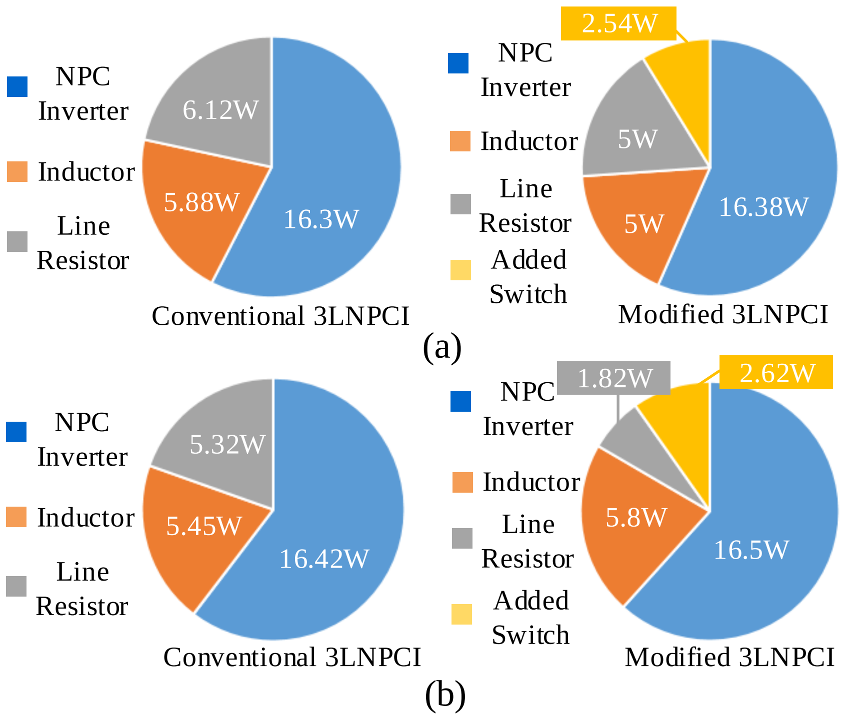

Fig. 3-14. Detailed losses of two IPOP conventional 3LNPCIs and enhanced ones at 400W. (a) Equal power distribution ratio (0.5:0.5). (b) Unequal power distribution ratio (0.3:0.7).

The analysis of detailed losses for two IPOP conventional 3LNPCIs and their enhanced counterparts at a 400W load, alongside various power sharing ratios, provides valuable insights into the efficiency and performance implications of the modified topology. Fig. 3-14, along with Table 3-4 and Table 3-5, offers a detailed comparison of these systems under diverse operational conditions. **Key Observations are as summarized follows.**

- *Reduction in Line Losses:* The data indicate that the modified 3LNPCIs, coupled with the tailored control strategy, can achieve a significant reduction in line losses. This improvement is attributed to the effective suppression of CCs and better current balancing, which directly impacts the line losses calculated based on the distribution of positive and negative currents.
- *Impact of Added Switch Losses:* Although the modified topology introduces additional switches, thereby potentially increasing the switch losses (P_{loss_sw}), this disadvantage is somewhat mitigated by the substantial reduction in line losses (P_{loss_line}). Therefore, the overall impact of the added switch losses on system efficiency is contingent upon the specific operational parameters.
- *Variable Net Effect on System Losses:* The comparison between the aggregation of line losses and switch losses in the enhanced 3LNPCI against the line losses in conventional 3LNPCIs reveals that the net effect on total system losses varies with different load powers and power distribution conditions. In certain scenarios, the efficiency gains from reduced line losses in the modified system may outweigh the additional switch losses, leading to a net reduction in total system losses. Conversely, under different conditions, the added switch losses might eclipse the benefits of reduced line losses, resulting in a net increase in total system losses.

As a result, the whole system loss with the proposed modified 3LNPCIs and the associated control strategy can either increase or decrease in comparison with conventional ones, according to the specific load powers and power distribution ratios. This variability underscores the importance of a nuanced approach to system design and operational planning, where the benefits of enhanced control capabilities and reduced CCs need to be balanced against the potential for increased switch losses.

Table 3-4. Detailed losses under different load powers of two IPOP conventional 3LNPCIs

Load resistor *R*	Power sharing ratio	NPC inverter (W)	Inductor (W)	Line resistor (W)	Total loss (W)
9.2Ω (350W)	0.5:0.5	14.35	4.9	5.6	24.85
	0.3:0.7	15.2	4.8	4.7	24.85
10.6Ω (300W)	0.5:0.5	13.1	3.9	4.8	21.75
	0.3:0.7	13.4	4.2	4.0	21.6
12.8Ω (250W)	0.5:0.5	11.5	3.1	4.3	18.85
	0.3:0.7	11.72	3.55	3.2	18.5
16Ω (200W)	0.5:0.5	9.8	2.4	3.7	15.9
	0.3:0.7	10.1	2.7	2.8	15.4

Table 3-5. Detailed losses under different load powers of two IPOP modified 3LNPCIs

Load resistor *R*	Power sharing ratio	NPC inverter (W)	Inductor (W)	Line resistor (W)	Added switches (W)	Total loss (W)
9.2Ω (350W)	0.5:0.5	14.4	4.6	4.6	2.34	26.12
	0.3:0.7	15.1	5.1	1.58	2.5	24.36
10.6Ω (300W)	0.5:0.5	13.0	3.7	4.3	2.04	23.04
	0.3:0.7	13.5	4.5	1.3	2.2	21.45
12.8Ω (250W)	0.5:0.5	11.3	3.0	3.6	1.85	19.75
	0.3:0.7	11.62	4.0	1.17	1.92	18.75
16Ω (200W)	0.5:0.5	9.8	2.25	3.1	1.55	16.7
	0.3:0.7	10.1	2.8	0.94	1.77	15.6

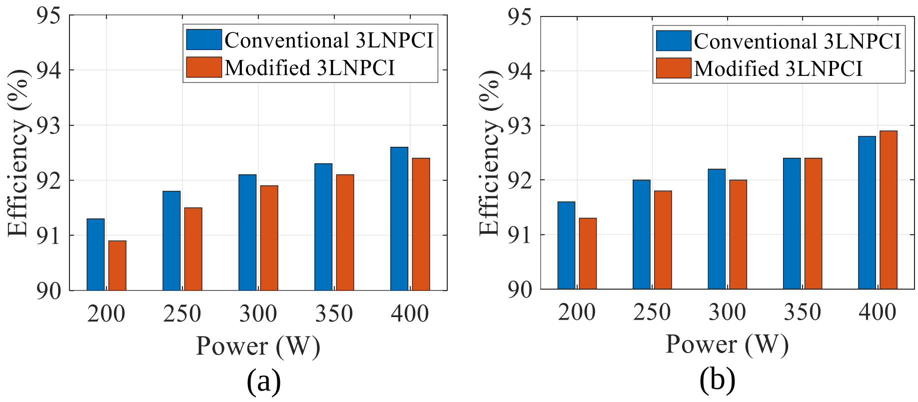

Fig. 3-15. A comparative display of efficiency between the conventional 3LNPCI and its enhanced version across varying load power levels. (a) Equal power distribution ratio (0.5:0.5). (b) Unequal power distribution ratio (0.3:0.7).

The comparative analysis of efficiency between the conventional and modified 3LNPCI topologies under various load power conditions, as summarized in Fig. 3-15, offers insightful findings regarding the practical implications of implementing the proposed modifications and control scheme. The efficiency measurements were conducted in a controlled experimental setup, where both input (P_{in}) and output (P_{out}) powers were meticulously recorded across different load resistances (R), facilitating the calculation of efficiency $\eta = P_o / P_{in}$.

Minimal Efficiency Discrepancy: The experimental results reveal a negligible efficiency difference (less than 0.3%) between the modified and conventional 3LNPCI topologies across the tested operating conditions. This indicates that the modifications introduced to enhance CC suppression capabilities do not significantly detract from the inherent efficiency of the 3LNPCI system.

Slight Efficiency Improvement: Notably, at a load power of 400W and a power-sharing ratio of 0.3:0.7, the aggregate efficiency of the system accompanying the implemented CC suppression scheme exhibits a marginal improvement over the system without CC suppression. This suggests that the optimized control strategy not only effectively mitigates CCs but may also contribute to a slight enhancement in system efficiency under certain conditions.

Implications: The findings from these hardware experiments underscore the feasibility of integrating the proposed CC suppression scheme into 3LNPCI systems without compromising their high-efficiency performance. The ability to maintain, and in some cases slightly improve, system efficiency while effectively addressing CC issues represents a significant advancement in inverter technology, ensuring that the high-efficiency advantage of 3LNPCIs is preserved even with the adoption of advanced control strategies for CC suppression. Therefore, in conclusion, the proposed modifications and control scheme for CC suppression in 3LNPCIs demonstrate a successful balance between enhancing system performance in terms of CC mitigation and maintaining the intrinsic high-efficiency characteristic of the inverters, making it a viable solution for applications requiring both high efficiency and effective CC management.

3.4.5 Discussion

The benefits of the modified 3LNPCIs can be discussed from two aspects.

Firstly, the main advantage of the modified topology is that CCs can be effectively suppressed, which can decrease the stress on active components, maintain high-quality output currents, and avoid system failures as much as possible.

Secondly, although additional switches will add the cost of system hardware, the efficiency gains achieved through CC suppression and improved current balancing will make up for the loss, especially considering long-term operations. Take two IPOP modified 3LNPCIs with unequal power sharing ratio (0.3:0.7) @ 400W as an example, the cost of the additional switches is about 70 HK$, and the efficiency improvement is about 0.1% (i.e., 0.4W). Therefore, after the system has been in operation for more than 13 years, the cost of the additional switches can be recovered. It should be noted that when the system operating power is 400W, lower rating switches can be used, therefore, the cost of additional switches will be significantly reduced and the cost will be made up within shorter time. On the other hand, it is worth emphasizing that the system efficiency improvement depended on multiple parameters, such as system operating power, line impedance parameters, and power sharing ratio, etc. In our small-scale test system, the system operating power is very low, therefore, the efficiency improvement is not obvious, while when the system operating power is high, the efficiency improvement would be more evident and the time to recoup the additional hardware costs will be shorter.

3.5 Conclusion

The chapter presents a novel decentralized control strategy tailored for the modified topology of 3LNPCIs, specifically designed to address CCs in IPOP single-phase 3LNPCIs. The study embarks on an analytical journey by formulating a mathematical model to capture the dynamics of currents in IPOP 3LNPCIs, which facilitates a comprehensive examination of the various factors influencing current behavior and elucidates the dual control objectives inherent to IPOP 3LNPCIs. A critical evaluation of the conventional half-bridge 3LNPCI topology reveals its intrinsic limitations, notably its single degree of modulation freedom, which is inadequate for simultaneously achieving the dual control objectives of CC suppression and proportional current sharing. This insight lays the groundwork for the proposed modified 3LNPCI topology, which introduces an additional degree of modulation freedom, thereby expanding the control capabilities of the system. Leveraging this enhanced topology, a sophisticated control strategy comprising two distinct degrees of control freedom is developed. This approach ingeniously integrates CC suppression with current sharing, ensuring that currents are distributed according to predetermined ratios without compromising on the mitigation of CCs. The practical viability and effectiveness of this proposed solution are substantiated through rigorous experimental validation, demonstrating its potential to significantly improve the performance and reliability of IPOP 3LNPCI systems. In essence, this chapter contributes a comprehensive solution to the challenges posed by CCs in IPOP single-phase half-bridge 3LNPCIs, offering a blend of theoretical innovation and practical applicability that holds promise for advancing the field of power electronics.

Chapter 4 Distributed Fixed-Time Secondary Control for DC Microgrid

4.1 Introduction

DC microgrids offer distinct benefits over their AC counterparts, including reduced complexity and enhanced control efficacy. They support a more seamless incorporation of the increasingly common DC-based energy sources (such as PV) and loads (including computers and electric vehicles), primarily due to the reduced necessity for energy conversion. This attribute significantly boosts the overall efficiency of the system and positions DC microgrids as a more practical option for advancing sustainable and eco-friendly energy distribution. For the effective coordination of integrated DGs and to meet the heightened performance standards anticipated for the entire system, it is imperative to implement an advanced secondary control strategy. This strategy should be characterized by its swift response capabilities and its ability to significantly diminish the need for extensive communication between DGs. Although current research has made commendable progress, the latest findings still require the transmission of two variables to achieve rapid convergence dynamics, necessitating a high communication bandwidth.

To mitigate this issue, this chapter proposes a new distributed fixed-time secondary control strategy that requires the exchange of only a single variable among neighboring DGs [102]. This innovative approach simplifies the control mechanism, reducing the complexity of implementation and minimizing the communication overhead compared to existing latest methods. The effectiveness and efficiency of the proposed control method are substantiated through various simulation results, demonstrating its superiority in terms of simplicity, reduced data transmission requirements, and enhanced system performance. This novel control strategy represents a significant step forward in the evolution of secondary control for DC microgrids, promising improved system responsiveness and stability with less variable transmitted.

4.2 Problem formulation and Control Objectives

The DC microgrid system structure discussed in this chapter, as depicted in Fig. 4-1, showcases a configuration where *N* DGs and *M* loads are interconnected to a shared DC bus. This arrangement is typical of DC microgrid architectures and widely used in industrial applications (such as, more electric aircraft, and all-electric ships [103], etc.), designed to efficiently distribute power generated from various renewable and non-renewable energy sources to a variety of electrical loads. In such a system, the DGs could include a mix of renewable energy sources like solar panels and wind turbines, along with possible energy storage systems such as batteries or supercapacitors, and even conventional diesel generators to ensure reliability and continuous power supply. The loads, on the other hand, represent the various electrical devices and systems that consume the power generated by the DGs, which could range from residential appliances and commercial equipment to industrial machinery. The common DC bus serves as the central electrical conduit that facilitates the distribution of electricity from the DGs to the loads. It is a critical component of the DC microgrid, ensuring that power is efficiently transmitted within the system while maintaining the necessary voltage levels for proper operation of all connected devices. The system structure illustrated in Fig. 4-1 lays the foundation for discussing the operational dynamics, control strategies pertinent to DC microgrids, as explored in the subsequent sections of this chapter.

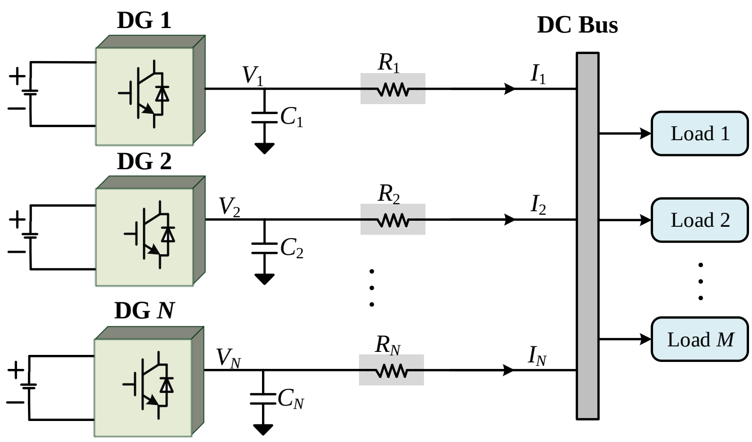

Fig. 4-1. The DC microgrid system.

4.2.1 Control Framework and Objectives

In DC microgrids, a hierarchical control framework is commonly utilized to ensure efficient and reliable operation. This framework typically consists of two levels: primary control and secondary control, each serving distinct functions within the system.

Primary Control Layer: The primary control layer is the first line of defense in maintaining the stability and functionality of the microgrid. It operates locally at each DG without the need for communication with other DGs or a central controller. A widely used approach within this layer is droop control, which is analogous to its AC counterpart and is employed to achieve proportional current sharing among the DGs. This method allows each DG to contribute to the total load demand based on its capacity and predetermined sharing ratio.

For the *i*th DG (i = 1, …, N), where N is the total number of DGs in the microgrid, the voltage reference signal V_{ref_i} can be determined by the droop equation as

$$V_i^{ref} = V^* - r_i I_i, \tag{4-1}$$

where V^* signifies the nominal voltage value of the DC bus, r_i represents the droop coefficient, and I_i denotes the actual output current from DG i.

The droop control essentially adjusts the output voltage of each DG in response to changes in the load current, ensuring that the load is shared proportionally among the DGs according to their droop characteristics. This adjustment is typically achieved by setting the voltage reference V_{ref_i} as a function of the output current I_i and a predefined droop coefficient r_i, which represents the sensitivity of the voltage adjustment to changes in the output current. For every DG in the system, a traditional dual-loop control architecture is employed, featuring an outer-loop dedicated to voltage regulation and an inner-loop focused on current control. This setup aims to adjust the output voltage V_i of each DG i to align with its designated reference value V_i^{ref}, i.e. $V_i = V_i^{ref}$. The coefficients for proportional and integral control pertaining to the voltage and current PI regulators of DG i are represented as K_{VPi}, K_{VIi} and K_{IPi},

K_{IIi}, respectively.

Accounting for the line resistance R_i, the expression for the DC bus voltage V_B can be articulated as

$$V_B = V_i - R_i I_i = V^* - (r_i + R_i) I_i. \tag{4-2}$$

From (4-2), we have

$$(r_i + R_i) I_i = (r_j + R_j) I_j, \ \forall i, j = 1, \ \ldots, \ N, \tag{4-3}$$

and

$$\frac{I_i}{I_j} = \frac{r_j + R_j}{r_i + R_i}, \ \forall i, j = 1, \ \ldots, \ N. \tag{4-4}$$

If r_i is chosen significantly larger than R_i, i.e., $r_i \gg R_i$, it can be derived that $I_i / I_j \approx r_j / r_i$. Hence, by selecting appropriate droop coefficients, the objective of achieving the intended current distribution among the units can be realized. Nonetheless, as inferred from (4-2), a substantial droop coefficient may lead to a significant variance between the actual DC bus voltage V_B and its nominal value V^*. To address this challenge, the implementation of a secondary control mechanism becomes imperative.

Secondary Control Layer: The secondary control layer comes into play to correct these deviations and restore the system voltage V_B to its nominal value V^*. Utilizing the secondary control, we have

$$V_i^{ref} = V^* - r_i I_i + u_i, \tag{4-5}$$

and

$$V_B = V^* - (r_i + R_i) I_i + u_i, \tag{4-6}$$

where u_i denotes the compensation signal generated through the application of the secondary control strategy.

By means of the definition of the 'virtual voltage drop' [88],

$$V_i^d = (r_i + R_i) I_i, \ i = 1, \ \ldots, \ N, \tag{4-7}$$

(4-6) can be rewritten as

$$V_B = V^* - V_i^d + u_i. \tag{4-8}$$

Within the realm of DC microgrid systems, two pivotal control targets are identified: regulation of the DC bus voltage and ensuring proportional load sharing across DGs, i.e.,

$$V_B = V^*, \tag{4-9}$$

and

$$I_i / I_j = r_j / r_i, \ \forall i, j = 1, \ \ldots, \ N. \tag{4-10}$$

1. DC bus voltage regulation: This objective focuses on maintaining the voltage at the DC bus at a specified value, ensuring stable and reliable power supply across the microgrid. Voltage regulation is crucial because fluctuations in the DC bus voltage can affect the performance and longevity of both the power-generating units and the loads. Effective voltage regulation contributes to the overall efficiency and safety of the microgrid, facilitating consistent power delivery even as load demands or generation capacities vary.
2. Proportional current sharing among DGs: This objective ensures that each DG contributes to the total load demand in proportion to its capacity or a predefined sharing ratio. Proportional current sharing is vital for several reasons:

- Optimal Utilization of Resources: By distributing the load according to the capabilities or efficiencies of the DGs, the microgrid can optimize its overall performance, making the best use of available renewable resources like solar and wind.
- Enhanced System Stability: Balanced current sharing helps maintain system stability by preventing large power imbalances that could lead to voltage sags, swells, or other disturbances within the microgrid.

4.2.2 Description of Notation

The symbol $\mathbb{R}^N$ are used to denote all N-dimensional real column vectors. Let $\mathbf{I}_N$ represent the $N \times N$ identity matrix, and $\mathbf{1}_N$ and $\mathbf{0}_N$ represent the N-dimensional column vector with all elements being 1 and 0, respectively. The superscript T denotes transpose of a matrix.

4.2.3 Description of Information Transmission Network

The information exchange channels of the DC microgrid can be described by a graph $\mathcal{G}=(\mathcal{V},\ \mathcal{E},\ \mathcal{A})$, where $\mathcal{V}=\{v_1,\ v_2,\ \ldots,\ v_N\}$ is the vertex set including all DGs, $\mathcal{E}\subseteq\mathcal{V}\times\mathcal{V}$ is the information channel set, and $\mathcal{A}\in\mathbb{R}^{N\times N}$ is the adjacent matrix. The adjacent matrix $\mathcal{A}$ is denoted as $\mathcal{A}=[a_{ij}]$, where the communication weights are set by $a_{ij}=1$ if $(v_j,\ v_i)\in\mathcal{E}$, and $a_{ij}=0$ if $(v_j,\ v_i)\notin\mathcal{E}$. Let $\mathcal{N}_i=\{v_j:(v_j,\ v_i)\in\varepsilon\}$ represents all neighbors of DG i. The Laplacian matrix $\mathcal{L}$ of graph $\mathcal{G}$ is given as $\mathcal{L}=[l_{ij}]\in\mathbb{R}^{N\times N}$, where $l_{ii}=\sum_{j\in\mathcal{N}_i}a_{ij}$, and $l_{ij}=-a_{ij}$ for $i\neq j$.

To meet the control goals outlined in equations (4-9) and (4-10) and to support the establishment of fixed-time convergence in the subsequent section, we present some pre-knowledge.

Assumption 1: The data exchange channel graph $\mathcal{G}$ is undirected and connected.

Assumption 2: The signal $V_i^d(t)$ exhibits a smoothness characteristic, and its derivative complies with

$$|\dot{V}_i^d(t)|\leq k_{Vd},\ i=1,\ 2,\ ...,\ N, \tag{4-11}$$

where k_{Vd} is a positive constant.

Lemma 1: [104] If $\xi_1,\ \xi_2,\ ...,\ \xi_N\geq 0$, then

(1) $\sum_{i=1}^{N}\xi_i^q\geq\left(\sum_{i=1}^{N}\xi_i\right)^q$ for $0<q\leq 1$;

(2) $N^{1-q}\left(\sum_{i=1}^{N}\xi_i\right)^q\leq\sum_{i=1}^{N}\xi_i^q\leq\left(\sum_{i=1}^{N}\xi_i\right)^q$ for $1<q<\infty$.

Lemma 2: [105] For the system $\dot{\mathbf{x}}(t)=f(\mathbf{x}(t)),\ x(0)=x_0$, where $\mathbf{x}=[x_1,...,\ x_N]^T\in\mathbb{R}^N$, and $f:\ \mathbb{R}^N\to\mathbb{R}^N$ is a continuous function on $\mathbb{R}^N$ and $f(0)=0$. If there exists a Lyapunov function $V(\mathbf{x}(t))$ satisfying the following inequation:

$$\dot{V}(\mathbf{x}(t)) \le -a_1 V^p - a_2 V^q, \tag{4-12}$$

with $a_1 > 0$, $a_2 > 0$, $0 < p < 1$, $q > 1$, then $\mathbf{x}(t)$ is the global fixed-time convergence system. Moreover, the convergence time T is bounded by:

$$T \le T_{\max} := \frac{1}{a_1(1-p)} + \frac{1}{a_2(q-1)}. \tag{4-13}$$

Lemma 3: [106] For a undirected connected graph $\mathcal{G}$, the eigenvalues of L satisfy $0 = \lambda_1(L) < \lambda_2(L) \le \ \dots \ \le \lambda_N(L)$. Then, the follows conclusion is valid that $\forall \boldsymbol{x} \in \mathbb{R}^N$, if $1_N^T \boldsymbol{x} = 0$, it has $\boldsymbol{x}^T L\boldsymbol{x} \ge \lambda_2(L)\boldsymbol{x}^T \boldsymbol{x}$.

4.3 Proposed Distributed fixed-time secondary controller

In this section, a distributed fixed-time secondary control method is suggested for DC microgrids. Unlike the approach detailed in [92], which requires the exchange of two variables among neighboring DGs for fixed-time control, the proposed method necessitates the transmission of only a single variable. This key difference has profound implications for the overall efficiency and feasibility of the control strategy in practical applications, i.e., reduced communication traffic, simplified implementation, enhanced reliability.

4.3.1 Distributed Fixed-time Secondary Control

The distributed secondary controller $u_i(t)$ is designed as

$$\begin{cases} u_i(t) = x_i(t) + V_i^d(t), \\ \dot{x}_i(t) = -k_1(w_i(t))^{\alpha} - k_2 \text{sign}(w_i(t)), \\ w_i(t) = \sum_{j \in N_i} (u_i(t) - u_j(t)), \ i = 1, \ \dots, \ N. \end{cases} \tag{4-14}$$

where $k_1 > 0$, $k_2 > 0$ are control gains, α is a positive parameter satisfying $\alpha > 1$.

Remark 1: The distributed controller we designed necessitates the transmission of merely a single variable, u_i, which significantly cuts down on communication traffic, especially when compared to the latest reported approach in [92] that involves the transmission of two variables.

Theorem 1: In accordance with Assumptions 1 and 2, the devised control mechanism, delineated in (4-14), is capable of achieving precise voltage regulation and proportional current distribution simultaneously, within a fixed convergence period.

To lay the groundwork for the subsequent proof, we initially establish the control discrepancy of DG i as

$$e(t) = V_B(t) - V^* = u_i(t) - V_i^d(t), \quad i = 1, \ ..., \ N. \tag{4-15}$$

Summing (4-15) together gives

$$Ne(t) = \sum_{i=1}^{N}(u_i(t) - V_{avg}^d(t)) = \sum_{i=1}^{N}\tilde{e}_i(t), \tag{4-16}$$

where

$$\tilde{e}_i(t) = u_i(t) - V_{avg}^d(t), \tag{4-17}$$

and

$$V_{avg}^d(t) = \frac{1}{N}\sum\nolimits_{i=1}^{N} V_i^d(t). \tag{4-18}$$

Furthermore, we define $\tilde{\mathbf{e}}(t) = [\tilde{e}_1(t), \ \ldots, \ \tilde{e}_N(t)]^T$.

Then, $w_i(t)$ can be expressed as

$$w_i(t) = \sum_{j \in N_i}(u_i(t) - u_j(t)) = \sum_{j \in N_i}(\tilde{e}_i(t) - \tilde{e}_j(t)), \tag{4-19}$$

and we have

$$\sum_{i=1}^{N}(w_i(t))^2 = (L\tilde{\boldsymbol{e}}(t))^T L\tilde{\boldsymbol{e}}(t) = \tilde{\boldsymbol{e}}(t)^T L^2\tilde{\boldsymbol{e}}(t). \tag{4-20}$$

Leveraging *Lemma* 3, we have:

$$\sum_{i=1}^{N}(w_i(t))^2 \geq \lambda_2(L)\tilde{\boldsymbol{e}}^T \boldsymbol{L}\tilde{\boldsymbol{e}}. \tag{4-21}$$

Proof: Choose the Lyapunov function $V = 0.5\tilde{\boldsymbol{e}}^T\boldsymbol{L}\tilde{\boldsymbol{e}}$. Then, it can be obtained that

$$\begin{aligned}
\dot{V} &= \tilde{\boldsymbol{e}}^T\boldsymbol{L}\dot{\tilde{\boldsymbol{e}}} = \sum_{i=1}^{N} w_i\dot{\tilde{e}}_i \\
&= \sum_{i=1}^{N} w_i\dot{\tilde{e}}_i = \sum_{i=1}^{N} w_i(-k_1 w_i^{\alpha} - k_2\text{sign}(w_i) + \dot{V}_i^d - \dot{V}_{avg}^d) \\
&= -k_1\sum_{i=1}^{N} w_i^{\alpha+1} - k_2\sum_{i=1}^{N}|w_i| + \sum_{i=1}^{N} w_i(\dot{V}_i^d - \dot{V}_{avg}^d) \\
&\leq -k_1\sum_{i=1}^{N}(w_i^2)^{\frac{\alpha+1}{2}} - (k_2 - 2k_{vd})\sum_{i=1}^{N}(w_i^2)^{\frac{1}{2}}
\end{aligned} \tag{4-22}$$

Then, k_2 can be aptly chosen to fulfill the condition outlined below:

$$k_2 > 2k_{vd} + k_0,\ i = 1,\ ...,\ N, \tag{4-23}$$

where $k_0 > 0$ is a positive constant.

Then, leveraging *Lemma* 1, (4-21) and (4-23), we have

$$\begin{aligned} \dot{V} &\le -k_1 \sum_{i=1}^{N} (w_i^2)^{\frac{\alpha+1}{2}} - k_0 \sum_{i=1}^{N} (w_i^2)^{\frac{1}{2}} \\ &\le -k_1 N^{\frac{1-\alpha}{2}} \left(\sum_{i=1}^{N} w_i^2 \right)^{\frac{\alpha+1}{2}} - k_0 \left(\sum_{i=1}^{N} (w_i^2) \right)^{\frac{1}{2}} \\ &\le -k_1 N^{\frac{1-\alpha}{2}} (2\lambda_2(L)V)^{\frac{\alpha+1}{2}} - k_0 (2\lambda_2(L)V)^{\frac{1}{2}} \\ &= -k_1 N^{\frac{1-\alpha}{2}} (2\lambda_2(L))^{\frac{\alpha+1}{2}} V^{\frac{\alpha+1}{2}} - k_0 \sqrt{2\lambda_2(L)} V^{\frac{1}{2}}. \end{aligned} \tag{4-24}$$

Then, based on *Lemma* 2, the system error $\tilde{\boldsymbol{e}}$ can get to the stable state within a fixed time, i.e.,

$$\lim_{t \to T^*} \tilde{\boldsymbol{e}}(t) = \mathbf{0}_N \ \ and \ \ \tilde{\boldsymbol{e}}(t) = \mathbf{0}_N,\ \forall t \ge T^*, \tag{4-25}$$

where

$$T^* \le \frac{\sqrt{2}}{k_0 \sqrt{\lambda_2(L)}} + \frac{2}{k_1 N^{\frac{1-\alpha}{2}} \left(2\lambda_2(L)\right)^{\frac{\alpha+1}{2}} (\alpha - 1)}. \tag{4-26}$$

Therefore, from (4-15)-(4-18), we can get that $\lim_{t \to T^*} e(t) = \lim_{t \to T^*} (u_i(t) - V_i^d(t)) = 0$. Then, it can be obtained from (8) that

$$\lim_{t \to T^*} V_B = V^*, \tag{4-27}$$

and the regulation objective (4-9) can be also obtained within the fixed time.

Further, we have

$$\lim_{t \to T^*} V_i^d = \lim_{t \to T^*} V_j^d = V_{avg}^d,\ \forall i, j = 1,\ ...,\ N. \tag{4-28}$$

Taking into account that r_i is selected to be significantly greater than R_i, i.e., $r_i \gg R_i$, it follows from (4-7) and (4-28) that

$$\lim_{t \to T^*} I_i / I_j = r_j / r_i,\ \forall i, j = 1,\ \dots,\ N. \tag{4-29}$$

Consequently, the control objective (4-10) can be also satisfied within a fixed time.

4.4 Case study

The proposed fixed-time control strategy for DC microgrids is validated by an extensive simulation conducted in MATLAB/Simulink, illustrating its robustness and reliability. The simulation environment meticulously recreates an islanded DC microgrid architecture that includes four DGs. Each DG unit is outfitted with a boost converter and a DC voltage source, reflecting a prevalent setup in microgrids powered by renewable energy sources. This configuration is crucial for understanding the dynamics and interactions within a microgrid, especially in scenarios where renewable energy plays a significant role. The boost converters play a pivotal part in regulating the voltage levels, ensuring that the energy generated by the DGs is efficiently utilized and harmonized with the load demands of the microgrid.

In this simulated environment, the efficacy of the control strategy is put to the test under various operating scenarios, like load variations, and communication delay, etc.. The results demonstrate the control scheme's capability to maintain stable voltage levels and ensure required current sharing among the DGs, thereby enhancing the overall resilience and efficiency of the microgrid. This detailed simulation not only underscores the practical applicability of the proposed control strategy but also provides valuable insights into optimizing the performance of DC microgrids, paving the way for more sustainable and reliable energy distribution in the context of increasing reliance on renewable energy sources.

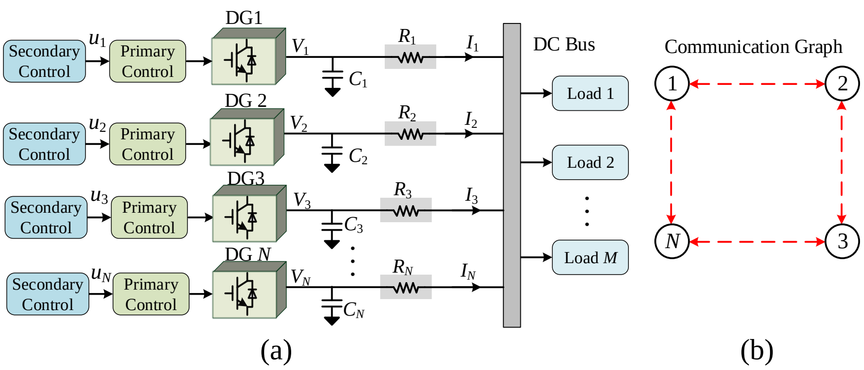

Fig. 4-2. The studied DC microgrid. (a) Physical topology. (b) Data exchange network.

Microgrid Configuration: The DC MG features four DGs that are interconnected in parallel to a shared DC bus, as depicted in Fig. 4-2 (a). This configuration is typical of

DC microgrids, allowing for the aggregation of power generated from multiple sources and its distribution to the loads connected to the DC bus.

Data Exchange Network: Fig. 4-2 (b) illustrates the data transmission network established among the DGs, which is critical for the distributed control scheme. This network enables the exchange of control signals (in this case, the single variable u_i for each DG) necessary for implementing the fixed-time control method.

The specific parameters for the microgrid system and the controllers, including the boost converter specifications, control gains, and other relevant settings, are systematically cataloged in Table 4-1. These parameters are essential for accurately configuring the simulation to reflect realistic operating conditions and control objectives.

Table 4-1 System parameters

		DG 1 ~ DG 4	
DC Voltage Source		V_{DC}	100 V
Rated DC Bus Voltage		V^*	200 V
Switching Frequency		f_{sw}	20 kHz
Filter Inductor		L_f	1 mH
Filter Capacitor		C_f	1 mF
Line Resistance		$R_{1\sim4}$	0.01 Ω
Primary Controller	Droop Gain	r_1=1, r_2=2, r_3=2, r_4=3	
	Voltage Loop	K_{VP}	1.2
		K_{VI}	80
	Current Loop	K_{IP}	0.1
		K_{II}	1
Secondary Controller		k_1	3
		k_2	0.5
		α	2

4.4.1 Case 1: Constant Power Load Step Change

The effectiveness of the proposed fixed-time control method is thoroughly examined through a case study involving constant power load (CPL) variations. The simulation is structured into four distinct stages to assess the control strategy's response to dynamic load changes:

Stage 1 (0-2s): At the onset (t = 0s), a CPL P_{L1} = 2000W is connected to the DC bus, with only the primary droop control activated. This stage assesses the primary control's ability to maintain system stability and load sharing in the presence of a significant load.

Stage 2 (2-4s): The proposed secondary control is activated at t = 2s, introducing the fixed-time control mechanism. This stage evaluates the secondary control's capability to restore the DC bus voltage to its rated value V^* = 200V and adjust the power sharing among the DGs in response to the existing load.

Stage 3 (4-6s): An additional CPL P_{L2} = 1000W is applied to the DC bus at t = 4s, increasing the total load and testing the control system's adaptability to sudden load variations.

Stage 4 (6-8s): The P_{L2} load is disconnected from the DC bus at t = 6s, simulating a reduction in demand. This final stage examines the system's response to decreasing load conditions and its ability to stabilize the DC bus voltage and current sharing among the DGs.

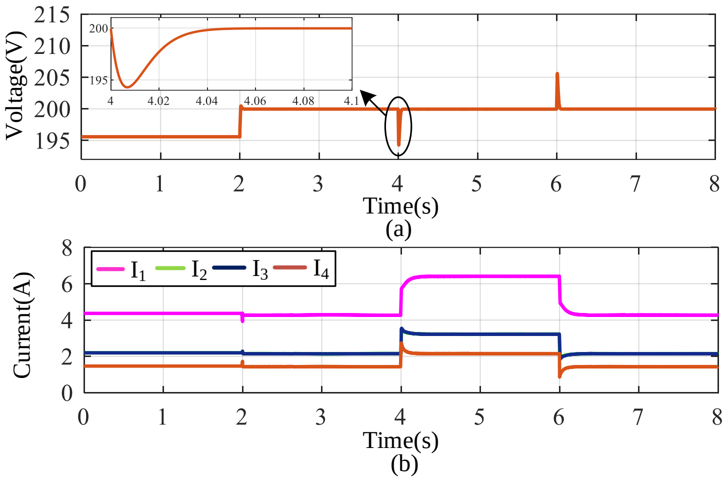

Fig. 4-3. Simulation waveforms under constant power load steps. (a) DC bus voltage. (b) Output currents of four DGs.

The simulation results, presented in Fig. 4-3, provide valuable insights into the control strategy's performance: Fig. 4-3 (a) illustrates the DC bus voltage response. Initially, with only primary control active, a noticeable voltage deviation from the rated value is observed due to the added load. However, upon activation of the proposed secondary control, the DC bus voltage swiftly stabilizes to the rated value, demonstrating the secondary control's effectiveness in voltage regulation despite CPL variations. Fig. 4-3 (b) depicts the proportional current sharing among the four DGs throughout the simulation. The results indicate that the proposed control method ensures proportional load distribution according to the desired ratios, even with the dynamic changes in load conditions. This case study underscores the proposed fixed-time secondary control method's efficacy in managing DC bus voltage regulation and maintaining proportional current sharing among DGs under varying CPL conditions.

4.4.2 Case 2: Plug-and-Play Performance

The plug-and-play capability of the proposed control method for DC microgrids is a critical feature that enhances the system's adaptability and resilience. This capability allows for the seamless integration or removal of DGs without disrupting the overall system stability and performance. The test scenario described involves an initial setup where all primary and secondary controllers are active, with a CPL P_L = 3000W connected to the common DC bus. The focus is on the dynamic response of the system when DG#4 is temporarily disconnected and then reconnected to the DC bus.

Key observations from the test results are:

- *DC bus voltage stability (Fig. 4-4 (a))*: Throughout the simulation, the DC bus voltage remains stable and accurately aligned with its nominal value, indicating effective voltage regulation by the control system. This stability is maintained even during the removal and reconnection of DG#4, showcasing the robustness of the voltage control mechanism.
- *Adaptive Current Sharing (Fig. 4-4 (b))*: Upon the removal of DG#4 at t = 4s, the system automatically adjusts, and the load current is proportionally redistributed among the remaining three DGs according to the predefined sharing ratios. This adjustment ensures that the system continues to operate efficiently without overloading any of the active DGs. When DG#4 is reintegrated into the system at t = 6s, the control method swiftly restores the original proportional current sharing among all four DGs, demonstrating the system's flexibility and the control strategy's ability to accommodate changes in the DG configuration.
- *Implications of Plug-and-Play Performance*: The satisfactory plug-and-play performance of the designed control method has significant implications for the

practical application and scalability of DC microgrids: 1. System Scalability: The ability to easily integrate or remove DGs without compromising system stability or performance is essential for the scalable expansion of microgrids, allowing them to adapt to changing energy demands and resource availability. 2. Enhanced Reliability: The control method's resilience to changes in the DG configuration enhances the reliability of the microgrid, ensuring continuous operation even in the face of component failures or maintenance requirements. 3. Operational Flexibility: The plug-and-play capability provides operators with greater flexibility in managing the microgrid, facilitating optimal resource utilization and maintenance scheduling without disrupting service.

In summary, the designed control method's plug-and-play performance, as demonstrated in the test scenario, underscores its effectiveness in ensuring stable and efficient operation of DC microgrids under dynamic conditions. This capability is crucial for the development of flexible, reliable, and scalable microgrid systems capable of supporting the evolving energy landscape.

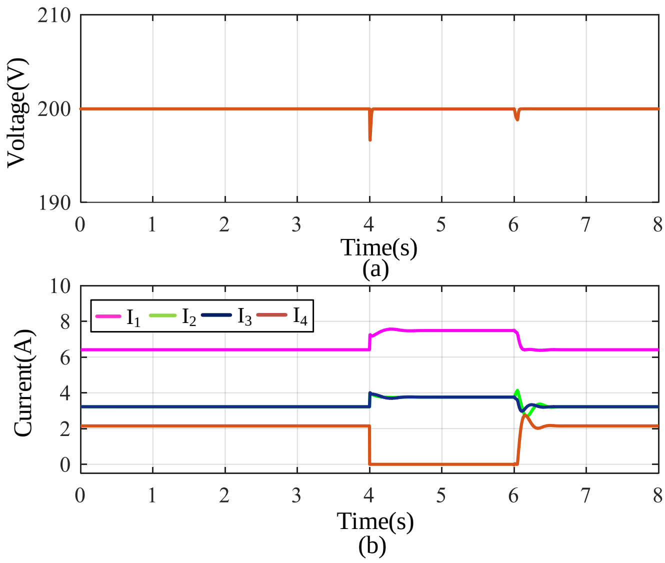

Fig. 4-4. Simulation waveforms with DG plug-and-play. (a) DC bus voltage. (b) Output currents of four DGs.

4.4.3 Case 3: System Performance with Communication Time Delay

The examination of the impact of communication delay on the performance of the designed controller is crucial for understanding the robustness and reliability of the control strategy in real-world DC microgrid applications. In this specific case study, the system's response to varying levels of communication delays T_{delay} is assessed to determine the maximum allowable delay that the system can tolerate without compromising stability and performance. The process mirrors that of Case 1, with the addition of different communication delays: T_{delay} = 10ms, 20ms, and 30ms.

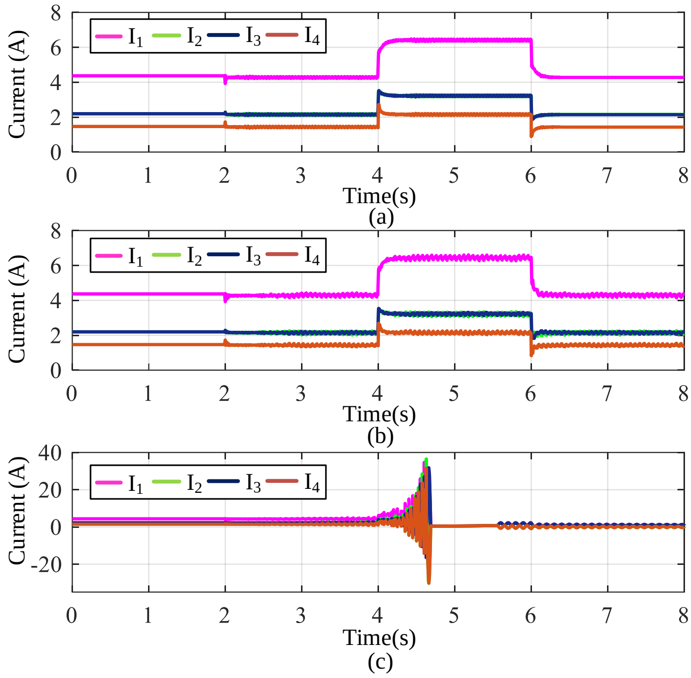

Fig. 4-5. Output currents with different communication time delays T_{delay}. (a) T_{delay} = 10ms. (b) T_{delay} = 20ms. (c) T_{delay} = 30ms.

Key Observations from Fig. 4-5:

- *Stability at Lower Delays*: When the communication delay is set to 10ms and 20ms, the output currents of all DGs remain stable, indicating that the system can maintain its operational integrity and perform as expected under these conditions. The ability to withstand delays up to 20ms while preserving voltage regulation and proportional current sharing demonstrates the designed control method's resilience to communication imperfections.
- *Instability at Higher Delay*: At a communication delay of 30ms, the system exhibits instability, as reflected in the output currents of the DGs. This instability is a clear indication that the control strategy's effectiveness is compromised

when the delay exceeds a certain threshold, in this case, 20ms.

- *Implications of Communication Delay on Control Performance*: The findings highlight the significance of communication timeliness in the distributed control framework of DC microgrids. A few key implications can be drawn: 1. Threshold for Delay Tolerance: The system's ability to sustain stability and performance with communication delays of up to 20ms provides a practical guideline for the design and implementation of communication networks in DC microgrids. Ensuring that the communication infrastructure can support delay times within this threshold is essential for reliable microgrid operation. 2. Need for Robust Communication Solutions: The sensitivity of the system to delays beyond 20ms underscores the importance of robust, high-speed communication solutions that can minimize latency, thereby enhancing the overall reliability and effectiveness of the control strategy. 3. Design Considerations: System designers and operators must consider communication delays in the control strategy development and microgrid architecture to ensure that the system can accommodate inherent communication latencies without sacrificing stability.

To sum up, the case study on communication delays reveals that the proposed secondary control method for DC microgrids can effectively manage voltage regulation and proportional current sharing, provided the communication delay is kept below 20ms. This insight is pivotal for ensuring the successful deployment and operation of distributed control systems in DC microgrids, particularly in scenarios where communication delays are inevitable.

4.4.4 Case 4: Performance Comparison

The comparative analysis presented in this case study elucidates the performance of the proposed distributed fixed-time secondary control method against two other control strategies: the asymptotically stable secondary control method detailed in [88] and the fixed-time secondary control technique from [92]. The evaluation focuses on the system's response to a step increase in CPL from 2000W to 3000W, mirroring the conditions outlined in Case 1.

Key Observations from Fig. 4-6:

- *DC Bus Voltage Response (Fig. 4-6 (a))*: The enlargement of the transient state waveforms reveals that both the proposed control method and the fixed-time control from [92] achieve a significantly faster settling of the DC bus voltage following the CPL increase compared to the asymptotically stable method in [88]. Notably, the proposed method exhibits a marginally quicker convergence to the steady-state voltage than the method in [92], indicating a slight performance edge in voltage regulation speed.
- *DG#4 Output Current Dynamics (Fig. 4-6 (b))*: The focus on DG#4's output current demonstrates that with the proposed controller, the current reaches a steady state more rapidly than with the other two methods. This quicker response underscores the proposed method's effectiveness in ensuring proportional current sharing among DGs in the face of load variations.
- *Advantages of the Proposed Control Strategy*: 1. Enhanced System Convergence Speed: The proposed control method facilitates a faster stabilization of both the DC bus voltage and the DGs' output currents following disturbances, such as CPL changes. This rapid convergence is crucial for maintaining the reliability and stability of the microgrid under dynamic conditions. 2. Reduced Communication Overhead: Unlike the fixed-time control method in [92], which requires the exchange of two variables among DGs, the proposed method achieves its performance improvements while only necessitating the transmission of a single variable. This reduction in the number of variables significantly eases the communication burden, minimizing the risk of network congestion and enhancing the scalability of the control scheme.

In general, the above comparative analysis underscores the superiority of the proposed control strategy in terms of both system convergence speed and communication efficiency. By achieving slightly better performance than the method in [92] with less information exchange, the proposed method presents a compelling solution for managing DC microgrids, particularly in scenarios where rapid response to load changes and communication efficiency are paramount. These attributes make the proposed control strategy highly suitable for modern DC microgrids that prioritize fast dynamics and low communication overhead.

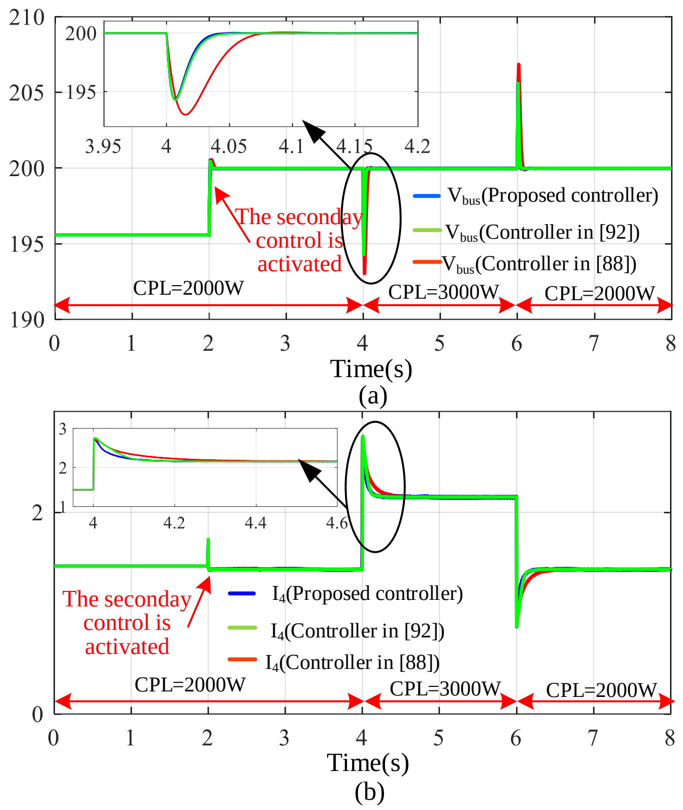

Fig. 4-6. Performance comparison. (a) DC bus voltage. (b) Output current of DG#4.

4.5 Conclusion

The chapter introduces a novel distributed fixed-time secondary control strategy specifically designed for islanded DC microgrids. This control approach stands out for its ability to ensure precise voltage regulation and proportional current distribution among DGs within a predetermined, fixed time frame. Key highlights and contributions of the proposed method include:

1. *Fixed-Time Control*: Unlike asymptotic methods that only guarantee stability over an indefinite period, the proposed strategy ensures that both voltage restoration and current sharing objectives are met within a fixed settling time, enhancing the predictability and responsiveness of the microgrid's control system.

2. *Reduced Communication Overhead*: The method requires the transmission of only a single variable between neighboring DGs, significantly reducing the

communication load compared to methods that necessitate multiple variables. This streamlined communication protocol contributes to a more efficient and scalable control architecture, particularly beneficial for larger microgrid systems with numerous nodes.

3. *Independence from DC Bus Voltage Information*: A distinctive feature of the proposed control strategy is its operational independence from direct DC bus voltage measurements. This eliminates the need for bus voltage sensors, thereby reducing system complexity, lowering costs, and enhancing overall reliability by removing a potential point of failure.

4. *Stability Analysis*: The stability and effectiveness of the proposed control method are rigorously validated using Lyapunov stability theory. This theoretical foundation ensures that the system remains stable under the proposed control, even in the face of disturbances or operational variances.

5. *Performance Validation*: Comparative simulations demonstrate that the proposed control strategy outperforms existing methods in terms of dynamic response and efficiency. The system exhibits faster voltage and current stabilization following disturbances, with significantly fewer data transmissions required for control coordination.

The proposed distributed fixed-time secondary control strategy represents a significant advancement in the management of islanded DC microgrids. By combining rapid dynamic response with reduced communication requirements and enhanced system reliability, the method addresses critical challenges in microgrid control, paving the way for more resilient and efficient energy distribution in off-grid and remote applications.

Chapter 5 Distributed Event-Triggered Fixed-Time Secondary Control for DC Microgrids Without Continuous Signal Transmission

5.1 Introduction

Although the method proposed in Chapter 4 can reduce the number of transmitted variables, it requires the continuous periodical signal transmission. To fully eliminate the continuous communication, this chapter proposes a novel distributed event-triggered fixed-time secondary control strategy, which is distinguished by rapid convergence speed, reduced communication burden, and non-reliance on DC bus voltage measurement [108]. The significant advancements made in this chapter can be itemized below:

1. Reduced Communication Variables: Unlike the method in [92], which necessitates the transmission of two variables for achieving fixed-time stability, the proposed strategy simplifies communication by requiring only a single variable to be conveyed to neighboring nodes. This simplification not only eases the implementation process but also substantially diminishes communication traffic, making the system more scalable and less prone to network congestion.

2. Event-Triggered Communication: The proposed method advances the concept of fixed-time distributed control by integrating event-triggered communication, wherein signal transmissions between DGs occur solely upon the fulfillment of specific event-triggering conditions. This approach marks a departure from the continuous periodic communication model utilized in [92], significantly reducing the frequency of data exchanges and, consequently, the overall communication burden on the system. Moreover, unlike the approach in [97], which still relies on continuous communication for triggering conditions, the proposed event-triggered controller achieves fixed-time convergence of system states without any need for continuous data exchange, representing a pioneering advancement in continuous-communication-free event-triggered control for DC microgrids.

3. Stability and Zeno Behavior: The stability of the proposed control strategy is rigorously validated using the Lyapunov stability theorem, ensuring that the system remains stable under the designed control laws. Additionally, the strategy effectively addresses and excludes the possibility of Zeno behavior—a phenomenon where an infinite number of triggering events occur in a finite time, which could potentially destabilize the system or overwhelm the communication network.

By addressing these critical aspects, the proposed distributed event-triggered fixed-time secondary control strategy enhances the operational efficiency, scalability, and reliability of DC microgrids. The reduction in communication variables, coupled with the assurance of system stability and the innovative use of event-triggered control mechanisms, positions this approach as a significant contribution to the ongoing development of advanced control strategies for modern microgrid systems.

Discussion: Compared with the static event-triggering control method proposed in this chapter, the dynamic event-triggering control method can adjust triggering intervals according to the change of system status, thereby further reducing the number of communications. However, although dynamic event-triggering control has been proposed [109], the fixed-time dynamic event-triggering control to speed up the system convergence has seldomly been reported for DC MGs due to the complexity of the controller design. On the other hand, dynamic ETC is very complex to implement and requires high computational performance of the controller. The trade-off between dynamic adjustment of triggering intervals and the complexity of implementation needs to be considered. In summary, the fixed-time event-triggering control is a promising method for DC MGs, but there are not many research results yet. It is still an open problem and deserves further study.

The structure of this chapter provides a systematic exploration of the proposed distributed event-triggered fixed-time secondary control strategy for DC microgrids, from theoretical development to practical validation. Here's a breakdown of this chapter's organization:

For the DC microgrid model and control objectives, since this chapter focuses on the same research object as Chapter 4, detailed descriptions are not repeated here; for specifics, please refer to Section 4.2 of Chapter 4.

In Section 5.2, we delve into the development of the proposed distributed event-triggered fixed-time secondary control strategy. It describes the design of the distributed event-triggered mechanism, which aims to optimize communication efficiency by transmitting signals only when specific conditions are met. The section also includes a comprehensive stability analysis using the Lyapunov stability theorem to prove that the proposed controller ensures fixed-time convergence to the desired state without the occurrence of Zeno behavior.

Section 5.3 presents detailed simulation studies conducted to evaluate the performance of the proposed control strategy under various operational scenarios. The simulations help demonstrate the effectiveness of the control in achieving the microgrid's control objectives, including the impact of event-triggered communication on reducing communication traffic and the system's response to different load conditions.

To validate the practical applicability of the proposed control strategy, Section 5.4 showcases experimental results obtained from a physical microgrid setup. The experiments aim to corroborate the findings from the simulation studies, providing tangible evidence of the control strategy's efficacy in real-world conditions.

In Section 5.5, the key findings and contributions of this chapter are summarized. It highlights the advantages of the proposed distributed event-triggered fixed-time secondary control strategy, particularly its ability to reduce communication requirements while ensuring fast and stable convergence to the desired operational state.

Note: To support the fixed-time stability analysis in the ensuing section, some pre-knowledges are needed. Since they are the same as those given in Part 4.2.3 (i.e., two assumptions and three lemmas), they will not be repeated here.

5.2 Distributed event-triggered fixed-time secondary controller

In this section, we introduce a delicate distributed event-triggered fixed-time secondary control framework specifically designed for DC microgrids. This innovative approach aims to achieve two primary objectives: precise voltage restoration to its nominal values and the implementation of a proportional current distribution among DGs within the microgrid, all within a fixed time. What sets this control strategy apart is its significant reduction of the communication overhead that typically plagues conventional control systems. This is accomplished through the adoption of an event-triggered communication mechanism, which smartly dictates the transmission of information only when certain system-defined events occur, thereby optimizing network traffic and reducing unnecessary information exchange. This method stands in stark contrast to traditional continuous communication strategies, where data is transmitted at fixed intervals regardless of the system's state, leading to inefficiency and increased network load. By integrating the event-triggered mechanism, the proposed controller intelligently balances the need for real-time control with the imperative of minimizing communication demands, thus enhancing the overall efficiency and reliability of the DC microgrid's operation.

The controller $u_i(t)$ with the event-triggered mechanism is designed as follows,

$$\begin{cases} w_i(t) = -k_1 \sum_{j\in N_i} sign\left(\int \hat{h}_i(t)dt - \int \hat{h}_j(t)dt\right) \\ \qquad\quad - k_2 \sum_{j\in N_i} sig^{\beta}\left(\int \hat{h}_i(t)dt - \int \hat{h}_j(t)dt\right) \\ u_i(t) = \int \hat{h}_i(t)dt, \\ \hat{h}_i(t) = w_i(t_k^i) + \dot{V}_i^d(t_k^i),\ t \in [t_k^i, t_{k+1}^i).\ i = 1,\ ...,\ N. \end{cases} \tag{5-1}$$

where k_1 and k_2 are positive constants, t_k^i is the time instant at which $h_i(t)$ is updated and transmitted to its neighboring converters.

To determine when to conduct a signal transmission, the following triggering condition is designed:

$$\begin{cases} e_i = \hat{h}_i(t) - h_i(t) \\ t_{k+1}^i = \inf\left\{ t > t_k^i \,\middle|\, |e_i| > \theta\left(k_1 \bar{N}_i + k_2 \sum_{j\in N_i} \left| \int \hat{h}_i(t)dt - \int \hat{h}_j(t)dt \right|^{\beta} + |\dot{V}_i^d(t)| \right) \right\}, \\ i = 1,\ 2,\ ...,\ N. \end{cases} \tag{5-2}$$

where e_i is the triggering error, and $0 < \theta < 1$ is an adjustable parameter that affects the number of triggering times. $\bar{N}_i$ represents the number of DG i's neighbors.

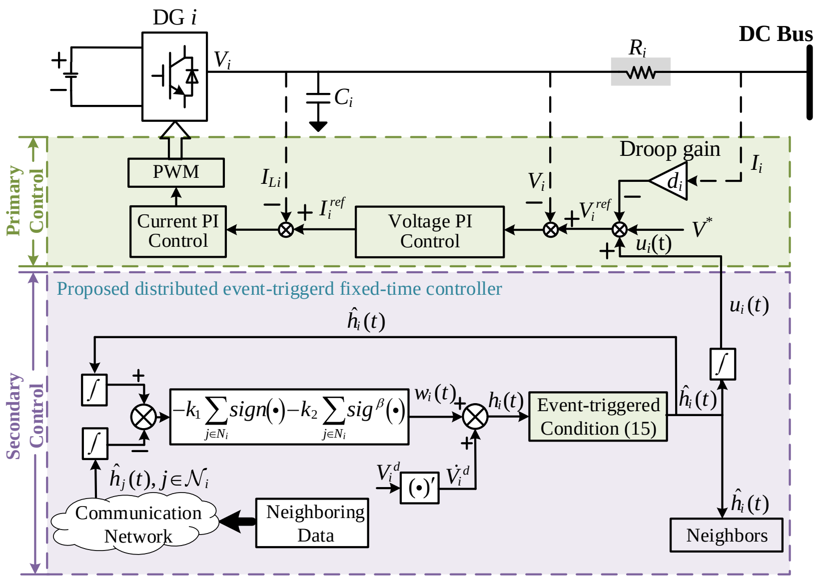

Fig. 5-1. The proposed distributed event-triggered fixed-time secondary control for DG i.

Fig. 5-1 depicts the complete control framework, integrating primary control with the newly introduced distributed event-triggered fixed-time secondary control for DG i.

Next, we give the following Theorems to show how the designed controller in (5-1)and the triggering condition (5-2) can make the DC microgrid system achieve fixed-time convergence.

***Theorem 1*:** Given Assumptions 1 and 2, the proposed event-triggered controller (5-1), complemented by the condition specified in (5-2), can guarantee simultaneous voltage restoration and current sharing within a fixed settling time.

***Theorem 2*:** Under the framework of the proposed event-triggered control scheme for each DG, the occurrence of Zeno behavior, which is defined as the occurrence of an infinite number of event triggers in a finite time interval, making the event-triggered mechanism ineffective and leading to potential system instability, can be effectively eliminated.

To proof the Theorem 1, we firstly define the control error of the ith converter as

$$e_{control}^{i}(t) = V_{bus}(t) - V^* = u_i(t) - V_i^d(t), \quad i = 1, \ldots, N. \tag{5-3}$$

Adding up the error term yields:

$$Ne_{control}^{i}(t)=\sum_{i=1}^{N}(u_i(t)-V_{avg}^{d}(t))=\sum_{i=1}^{N}\tilde{e}_i(t), \tag{5-4}$$

where

$$\tilde{e}_i(t)=u_i(t)-V_{avg}^{d}(t), \tag{5-5}$$

and

$$V_{avg}^{d}(t)=\frac{1}{N}\sum_{i=1}^{N}V_i^{d}(t). \tag{5-6}$$

We define $\tilde{\boldsymbol{e}}=[\tilde{e}_1,\ ...,\ \tilde{e}_N]$.

5.2.1 Proof of Theorem 1

Select the Lyapunov function $V=\frac{1}{2}\tilde{\boldsymbol{e}}^T\tilde{\boldsymbol{e}}$. Then, we have

$$\begin{aligned}
\dot{V}&=\tilde{\boldsymbol{e}}^T\dot{\tilde{\boldsymbol{e}}}=\sum_{i=1}^{N}\tilde{e}_i\dot{\tilde{e}}_i=\sum_{i=1}^{N}\tilde{e}_i(\dot{u}_i-\dot{V}_{avg}^{d})=\sum_{i=1}^{N}\tilde{e}_i\left(\hat{h}_i(t)-\dot{V}_{avg}^{d}\right)\le\sum_{i=1}^{N}\tilde{e}_i\left(\hat{h}_i(t)\right)+\sum_{i=1}^{N}k_{vd}\,|\,\tilde{e}_i\,|\\
&=\sum_{i=1}^{N}\tilde{e}_i\left(h_i(t)+e_i\right)+\sum_{i=1}^{N}k_{vd}\,|\,\tilde{e}_i\,|\\
&=\sum_{i=1}^{N}\tilde{e}_i\left(-k_1\sum_{j\in N_i}sign(\int\hat{h}_i(t)dt-\int\hat{h}_j(t)dt)-k_2\sum_{j\in N_i}sig^{\beta}(\int\hat{h}_i(t)dt-\int\hat{h}_j(t)dt)+\dot{V}_i^{d}+e_i\right)+\sum_{i=1}^{N}k_{vd}\,|\,\tilde{e}_i\,|\\
&=\sum_{i=1}^{N}\tilde{e}_i\left(-k_1\sum_{j\in N_i}sign(u_i-u_j)-k_2\sum_{j\in N_i}sig^{\beta}(u_i-u_j)+\dot{V}_i^{d}+e_i\right)+\sum_{i=1}^{N}k_{vd}\,|\,\tilde{e}_i\,|\\
&\le\sum_{i=1}^{N}\tilde{e}_i\left(-k_1\sum_{j\in N_i}sign(u_i-u_j)-k_2\sum_{j\in N_i}sig^{\beta}(u_i-u_j)\right)+\sum_{i=1}^{N}\tilde{e}_ie_i+\sum_{i=1}^{N}2k_{vd}\,|\,\tilde{e}_i\,|\\
&\le\sum_{i=1}^{N}\tilde{e}_i\left(-k_1\sum_{j\in N_i}sign(u_i-u_j)-k_2\sum_{j\in N_i}sig^{\beta}(u_i-u_j)\right)+\sum_{i=1}^{N}|\,\tilde{e}_i\,|(|\,e_i\,|+2k_{vd})
\end{aligned} \tag{5-7}$$

For the first term on the right side, since $\mathbf{1}_N^T\tilde{\boldsymbol{e}}=0$, based on Lemma 1 and Lemma 3, we have

$$\begin{aligned}
&\sum_{i=1}^{N}\tilde{e}_i\left(-k_1\sum_{j\in N_i}sign(u_i-u_j)-k_2\sum_{j\in N_i}sig^{\beta}(u_i-u_j)\right)\\
&=\sum_{i=1}^{N}\tilde{e}_i\left(-k_1\sum_{j\in N_i}sign((u_i-V_{avg}^{d})-(u_j-V_{avg}^{d}))-k_2\sum_{j\in N_i}sig^{\beta}((u_i-V_{avg}^{d})-(u_j-V_{avg}^{d}))\right)\\
&=-k_1\sum_{i=1}^{N}\tilde{e}_i\sum_{j\in N_i}sign(\tilde{e}_i-\tilde{e}_j)-k_2\sum_{i=1}^{N}\tilde{e}_i\sum_{j\in N_i}sig^{\beta}(\tilde{e}_i-\tilde{e}_j)
\end{aligned}$$

$$
\begin{aligned}
&= -\frac{k_1}{2}\sum_{i=1}^{N}\sum_{j=1}^{N}a_{ij}\,|\,\tilde{e}_i-\tilde{e}_j\,| - \frac{k_2}{2}\sum_{i=1}^{N}\sum_{j=1}^{N}a_{ij}\,|\,\tilde{e}_i-\tilde{e}_j\,|^{\beta+1} \\
&\le -\frac{k_1}{2}\left(\sum_{i=1}^{N}\sum_{j=1}^{N}a_{ij}\,|\,\tilde{e}_i-\tilde{e}_j\,|^2\right)^{\frac{1}{2}} - \frac{k_2}{2}(N(N-1))^{\frac{1-\beta}{2}}\left(\sum_{i=1}^{N}\sum_{j=1}^{N}a_{ij}\,|\,\tilde{e}_i-\tilde{e}_j\,|^2\right)^{\frac{\beta+1}{2}} \\
&= -\frac{k_1}{2}(2\tilde{\boldsymbol{e}}^T L\tilde{\boldsymbol{e}})^{\frac{1}{2}} - \frac{k_2}{2}(N(N-1))^{\frac{1-\beta}{2}}\left(2\tilde{\boldsymbol{e}}^T L\tilde{\boldsymbol{e}}\right)^{\frac{\beta+1}{2}} \\
&\le -\frac{k_1}{2}(2\lambda_2\tilde{\boldsymbol{e}}^T\tilde{\boldsymbol{e}})^{\frac{1}{2}} - \frac{k_2}{2}(N(N-1))^{\frac{1-\beta}{2}}\left(2\lambda_2\tilde{\boldsymbol{e}}^T\tilde{\boldsymbol{e}}\right)^{\frac{\beta+1}{2}} \\
&= -\frac{k_1}{2}(2\lambda_2)^{\frac{1}{2}}(\tilde{\boldsymbol{e}}^T\tilde{\boldsymbol{e}})^{\frac{1}{2}} - \frac{k_2}{2}(N(N-1))^{\frac{1-\beta}{2}}(2\lambda_2)^{\frac{\beta+1}{2}}\left(\tilde{\boldsymbol{e}}^T\tilde{\boldsymbol{e}}\right)^{\frac{\beta+1}{2}} \\
&= -k_1\sqrt{\lambda_2}V^{\frac{1}{2}} - \frac{k_2}{2}(N(N-1))^{\frac{1-\beta}{2}}(4\lambda_2)^{\frac{\beta+1}{2}}V^{\frac{\beta+1}{2}}
\end{aligned}
\tag{5-8}
$$

For the second term on the right side, we have

$$
\begin{aligned}
&\sum_{i=1}^{N}|\tilde{e}_i|(|e_i|+2k_{vd}) < \sum_{i=1}^{N}|\tilde{e}_i|\left(\theta k_1\bar{N}_i+\theta k_2\sum_{j\in N_i}\left|\int\hat{h}_i(t)dt-\int\hat{h}_j(t)dt\right|^{\beta}+\theta|\dot{V}_i^d|+2k_{vd}\right) \\
&\le(\theta k_1\bar{N}^{\max}+2k_{vd})\sum_{i=1}^{N}|\tilde{e}_i|+\theta\sum_{i=1}^{N}|\tilde{e}_i||\dot{V}_i^d|+\theta k_2\sum_{i=1}^{N}|\tilde{e}_i|\sum_{j\in N_i}\left|\int\hat{h}_i(t)dt-\int\hat{h}_j(t)dt\right|^{\beta} \\
&\le(\theta k_1\bar{N}^{\max}+2k_{vd})\sum_{i=1}^{N}|\tilde{e}_i|+\theta k_{vd}\sum_{i=1}^{N}|\tilde{e}_i|+\theta k_2\sqrt{2V}\cdot\sum_{i=1}^{N}\sum_{j\in N_i}\left|\int\hat{h}_i(t)dt-\int\hat{h}_j(t)dt\right|^{\beta} \\
&=(\theta k_1\bar{N}^{\max}+2k_{vd}+\theta k_{vd})\sum_{i=1}^{N}|\tilde{e}_i|+\theta k_2\sqrt{2V}\cdot\sum_{i=1}^{N}\sum_{j\in N_i}\left(\left|\int\hat{h}_i(t)dt-\int\hat{h}_j(t)dt\right|^2\right)^{\frac{\beta}{2}} \\
&=(\theta k_1\bar{N}^{\max}+2k_{vd}+\theta k_{vd})\sum_{i=1}^{N}|\tilde{e}_i|+\theta k_2\sqrt{2V}\cdot\sum_{i=1}^{N}\sum_{j\in N_i}\left(\left|\tilde{e}_i-\tilde{e}_j\right|^2\right)^{\frac{\beta}{2}} \\
&\le(\theta k_1\bar{N}^{\max}+2k_{vd}+\theta k_{vd})\sum_{i=1}^{N}|\tilde{e}_i|+\theta k_2\sqrt{2V}\cdot\left(\sum_{i=1}^{N}\sum_{j=1}^{N}a_{ij}\left|\tilde{e}_i-\tilde{e}_j\right|^2\right)^{\frac{\beta}{2}} \\
&=(\theta k_1\bar{N}^{\max}+2k_{vd}+\theta k_{vd})\sum_{i=1}^{N}|\tilde{e}_i|+\theta k_2\sqrt{2V}\cdot(2\tilde{\boldsymbol{e}}^T L\tilde{\boldsymbol{e}})^{\frac{\beta}{2}} \\
&\le(\theta k_1\bar{N}^{\max}+2k_{vd}+\theta k_{vd})\sum_{i=1}^{N}|\tilde{e}_i|+\theta k_2\lambda_N^{\frac{\beta}{2}}2^{\frac{1+2\beta}{2}}V^{\frac{1+\beta}{2}}
\end{aligned}
\tag{5-9}
$$

where $\bar{N}^{\max}=\max\{\bar{N}_1,\bar{N}_2,\ldots,\bar{N}_N\}$.

According to Cauchy-Schwarz inequality, we have:

$$
(\theta k_1\bar{N}^{\max}+2k_{vd}+\theta k_{vd})\sum_{i=1}^{N}|\,\tilde{e}_i\,|\le\sqrt{2}(\theta k_1\bar{N}^{\max}+2k_{vd}+\theta k_{vd})\sqrt{N}V^{\frac{1}{2}}. \tag{5-10}
$$

Substituting (5-8), (5-9) and (5-10) into (5-7), we have

$$
\begin{aligned}
\dot{V} \le & -k_1\sqrt{\lambda_2}V^{\frac{1}{2}} - \frac{k_2}{2}(N(N-1))^{\frac{1-\beta}{2}}(4\lambda_2)^{\frac{1+\beta}{2}}V^{\frac{1+\beta}{2}} \\
& + \sqrt{2}(\theta k_1\bar{N}^{\max} + 2k_{vd} + \theta k_{vd})\sqrt{N}V^{\frac{1}{2}} \\
& + \theta k_2\lambda_N^{\frac{\beta}{2}}2^{\frac{1+2\beta}{2}}V^{\frac{1+\beta}{2}} \\
= & -\left(k_1\sqrt{\lambda_2} - \sqrt{2}(\theta k_1\bar{N}^{\max} + 2k_{vd} + \theta k_{vd})\sqrt{N}\right)V^{\frac{1}{2}} \\
& -\left(\frac{k_2}{2}(N(N-1))^{\frac{1-\beta}{2}}(4\lambda_2)^{\frac{1+\beta}{2}} - \theta k_2\lambda_N^{\frac{\beta}{2}}2^{\frac{1+2\beta}{2}}\right)V^{\frac{1+\beta}{2}}.
\end{aligned}
\tag{5-11}
$$

From (5-11), there exists a positive constant μ_1 satisfying

$$
\mu_1 = \frac{\sqrt{2N}\left(2k_{vd} + \theta k_{vd}\right)}{\sqrt{\lambda_2} - \sqrt{2N}\theta\bar{N}^{\max}}
\tag{5-12}
$$

where $\theta < \sqrt{\lambda_2} / \left(\sqrt{2N}\bar{N}^{\max}\right)$.

Then, k_1 can be selected as

$$
k_1 = \mu_1 + k_{01},
\tag{5-13}
$$

where $k_{01} > 0$ is an arbitrary positive constant.

To guarantee the coefficient of $V^{\frac{1+\beta}{2}}$ is negative, there should be $k_2>0$ and $\theta < (N(N-1))^{\frac{1-\beta}{2}}(\lambda_2)^{\frac{1+\beta}{2}} / (\sqrt{2}\lambda_N^{\frac{\beta}{2}})$.

In addition, the allowable range of θ has been further restricted to

$$
0 < \theta < \min \{1, \sqrt{\lambda_2} / \left(\sqrt{2N}\bar{N}^{\max}\right), (N(N-1))^{\frac{1-\beta}{2}}(\lambda_2)^{\frac{1+\beta}{2}} / (\sqrt{2}\lambda_N^{\frac{\beta}{2}})\}.
\tag{5-14}
$$

To make the subsequent expressions more concise, we use k_{02} to represent the coefficient of $V^{\frac{1+\beta}{2}}$ with appropriately chosen parameter k_2 and θ. That is,

$$
k_{02} = \frac{k_2}{2}(N(N-1))^{\frac{1-\beta}{2}}(4\lambda_2)^{\frac{1+\beta}{2}} - \theta k_2\lambda_N^{\frac{\beta}{2}}2^{\frac{1+2\beta}{2}}.
\tag{5-15}
$$

Substitute (5-13) and (5-15) into (5-11), we have

$$
\dot{V} \le -k_{01}\left(\sqrt{\lambda_2} - \sqrt{2N}\theta\bar{N}^{\max}\right)V^{\frac{1}{2}} - k_{02}V^{\frac{1+\beta}{2}}.
\tag{5-16}
$$

Then, according to Lemma 2, the system error $\tilde{\boldsymbol{e}}$ is globally fixed-time stable, i.e.,

$$
\lim_{t\to T^*} \tilde{\boldsymbol{e}}(t) = \mathbf{0}_N \ \ and \ \ \tilde{\boldsymbol{e}}(t) = \mathbf{0}_N, \ \forall t \ge T^*,
\tag{5-17}
$$

where

$$T^* \le \frac{2}{k_{01}\left(\sqrt{\lambda_2}-\sqrt{2N}\theta\bar{N}^{\max}\right)}+\frac{2}{k_{02}(\beta-1)}\,. \tag{5-18}$$

Therefore, from (5-3)-(5-6), we have $\lim_{t\to T^*} e(t)=\lim_{t\to T^*}(u_i(t)-V_i^d(t))=0$. Subsequently, it can be deduced from $V_B = V^* - V_i^d + u_i$ that

$$\lim_{t\to T^*} V_B = V^*, \tag{5-19}$$

and the voltage restoration can be fulfilled within the fixed time, satisfying the requirements.

Further, it can be obtained that

$$\lim_{t\to T^*} V_i^d = \lim_{t\to T^*} V_j^d = V_{avg}^d,\ \forall i, j=1,\ ...,\ N. \tag{5-20}$$

Since d_i is set enough larger than R_i, i.e., $d_i \gg R_i$, and based on $V_i^d = (d_i + R_i)I_i,\ i = 1,\ \ldots,\ N,$ and (5-20), we have

$$\lim_{t\to T^*} I_i / I_j = d_j / d_i,\ \forall i, j=1,\ \ldots,\ N. \tag{5-21}$$

Consequently, the fulfillment of current sharing control objective (i.e., $I_i / I_j = d_j / d_i,\ \forall i, j=1,\ \ldots,\ N$) is also attainable in a fixed settling time.

5.2.2 Proof of Theorem 2

In this part, it is proved that the proposed event-triggered controller with event-triggered conditions (5-2) can exclude Zeno behavior.

According to the triggering error in (5-2), it can be derived that

$$|\hat{h}_i(t_k^i)|=|h_i(t)+e_i(t)|\le|h_i(t)|+|e_i(t)|,\quad t>t_k^i. \tag{5-22}$$

Combining the condition $|e_i|>\theta\left(k_1\bar{N}_i+k_2\sum_{j\in N_i}\left|\int\hat{h}_i(t)dt-\int\hat{h}_j(t)dt\right|^{\beta}+|\dot{V}_i^d(t)|\right)\ge\theta|h_i(t)|$ with (5-22), we have

$$|\hat{h}_i(t)|\le(1+\frac{1}{\theta})|e_i(t)| \tag{5-23}$$

During $t\in[t_k^i,\ t_{k+1}^i)$, assuming no neighbor's new information is received, then,

1) When $\int\hat{h}_i(t)dt\ne\int\hat{h}_j(t)dt$:

The following equation can be obtained based on (5-2):

$$\dot{e}_i(t) = -\dot{\hat{h}}_i(t) = -f_i(t), \tag{5-24}$$

where

$$\begin{aligned} f_i(t) = -k_2\beta \bullet sign(\int \hat{h}_i(t)dt - \int \hat{h}_j(t)dt) \bullet \\ \sum_{j \in N_i}\left(\left|\int \hat{h}_i(t)dt - \int \hat{h}_j(t)dt\right|^{\beta-1} |\hat{h}_i(t) - \hat{h}_j(t)|\right) + \ddot{V}_i^d(t). \end{aligned} \tag{5-25}$$

Since $e_i(t_k^i) = 0$, integrating both sides of (5-24) from t_k^i to t, we have

$$e_i(t) = -\int_{t_k^i}^{t} f_i(t)dt\ . \tag{5-26}$$

Furthermore, the proof of the exclusion of Zeno behavior can be divided into two parts:

(1.1) when $e_i(t) \neq 0$ at time instant $t > t_k^i$:

After $t = t_k^i$, when $e_i(t) \neq 0$ at time instant $t > t_k^i$, then, there exists a constant $M \neq 0$, such that (5-26) at time instant t can be rewritten as

$$e_i(t) = -\int_{t_k^i}^{t} Mdt = -M(t - t_k^i) \tag{5-27}$$

where M is a constant.

Combing (5-23) and (5-27), we have

$$(t - t_k^i)|M| \geq \frac{\theta}{1+\theta} |\hat{h}_i(t_k^i)| \tag{5-28}$$

Next, we prove that $\hat{h}_i(t_k^i) \neq 0$.

To verify $\hat{h}_i(t_k^i) \neq 0$, we firstly introduce the following lemma:

***Lemma* 4:** If $\hat{h}_i(t_k^i) = 0$, then, at the last triggering time instant, $\hat{h}_i(t_{k-1}^i)$ is also equal to 0. That is, $\hat{h}_i(t_{k-1}^i) = \hat{h}_i(t_k^i) = 0$.

Next, we prove the above lemma and furthermore show $\hat{h}_i(t_k^i) \neq 0$ by the contradiction method.

Proof: Assume $\hat{h}_i(t_k^i) = 0$ and $\hat{h}_i(t_{k-1}^i) \neq 0$, then, according to (5-2), we have the following inequality:

$$|e_i(t)| = |\hat{h}_i(t_{k-1}^i) - h_i(t)| > \theta |h_i(t)| \tag{5-29}$$

At this point, we can easily conclude that when $h_i(t)$ has not yet reached 0, (5-2) will be triggered and the signal will be transmitted, that is, $\hat{h}_i(t_k^i) \neq 0$, this contradicts the previous assumption that $\hat{h}_i(t_k^i)=0$. Therefore, we have $\hat{h}_i(t_{k-1}^i)=\hat{h}_i(t_k^i)=0$.

Furthermore, if $\hat{h}_i(t_{k-1}^i)=\hat{h}_i(t_k^i)=0$ holds, it means $e_i(t)$=0, then, the triggering condition (5-12) is no longer satisfied, that is, no trigger occurs, this contradicts the assumption that at time instant t_k^i, the $h_i(t)$ is triggered. Therefore, it can be concluded that $\hat{h}_i(t)\neq 0$.

Consequently, it can be obtained from (5-28) that

$$t_{k+1}^i - t_k^i \geq t - t_k^i \geq \frac{\theta}{1+\theta}|\hat{h}_i(t)| > 0, \tag{5-30}$$

which means that Zeno behavior will not occur.

(1.2) when $e_i(t)$ = 0 at time instant $t > t_k^i$:

Since $|h_i(t)|\geq 0$, when $e_i(t)$ = 0, the triggering condition (5-2) will not be satisfied and no trigger occurs. Therefore, when $e_i(t)$ = 0, the Zeno behavior can be excluded.

2) When $\int \hat{h}_i(t)dt = \int \hat{h}_j(t)dt$:

If $\int \hat{h}_i(t)dt = \int \hat{h}_j(t)dt$, it means that the system has reached the steady state, and according to (5-12), the triggering condition will not be satisfied and no signal transmission will occur. This means no Zeno behavior. Furthermore, it shows that the proposed approach can notably decrease communication traffic, particularly in steady-state conditions.

Combining the analysis outlined in parts 1) and 2), it becomes evident that the proposed event-triggered control scheme and the corresponding triggering condition are strategically crafted to eliminate Zeno behavior effectively.

Therefore, the proposed event-triggered control scheme not only enhances communication efficiency and system responsiveness but also ensures the practical viability and stability of the control system by effectively eliminating the risk of Zeno behavior.

5.3 Simulation Case Study

The effectiveness of the proposed event-triggered control method for DC microgrids is thoroughly evaluated through a detailed simulation using

MATLAB/Simulink as shown in Fig. 5-2. The simulation setup models an islanded DC microgrid comprising four DGs, each equipped with a boost converter to emulate power electronic switching behaviors and a DC voltage source to represent the energy source.

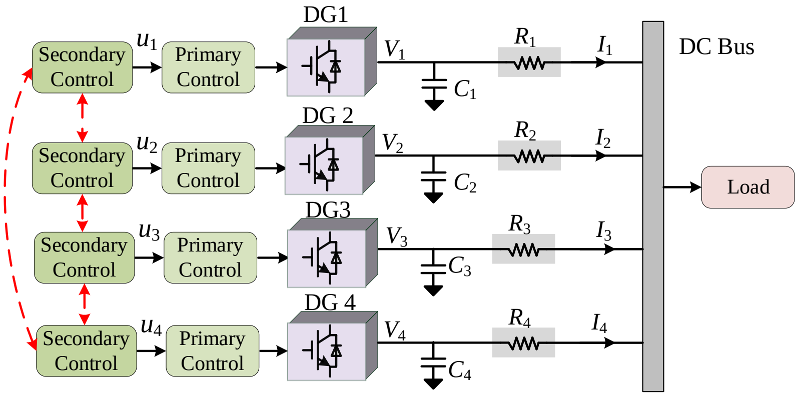

Fig. 5-2. The studied DC microgrid and its communication topology.

Simulation Model Configuration:

DG Configuration: The four DGs are configured in parallel, ensuring a collaborative power supply to the common DC bus. This parallel arrangement is critical for achieving proportional current sharing and voltage stability across the microgrid.

Network Topology: The communication interconnections between the DGs are depicted using red dashed lines. This topology defines how information is exchanged between DGs, enabling coordinated control actions.

A comprehensive list of default parameters for the microgrid system and control strategies is provided in Table 5-1. These parameters include electrical characteristics, control gains, and other system attributes essential for the simulation.

The simulation studies conducted using this MATLAB/Simulink model are designed to validate the performance of the event-triggered control method under various operational scenarios, including load changes, DG plug-and-play actions, and communication delay impacts. By closely replicating the dynamics and interactions within an actual DC microgrid, the simulation provides valuable insights into the practical applicability and benefits of the proposed control strategy, highlighting its potential to enhance microgrid stability, efficiency, and scalability.

Table 5-1 System Parameters

<table>
<tr><td colspan="2"></td><td colspan="2">DG 1 ~ DG 4</td></tr>
<tr><td colspan="2">DC Voltage Source</td><td>V_{DC}</td><td>150 V</td></tr>
<tr><td colspan="2">Rated DC Bus Voltage</td><td>V^*</td><td>300 V</td></tr>
<tr><td colspan="2">Switching Frequency</td><td>f_{sw}</td><td>20 kHz</td></tr>
<tr><td colspan="2">Filter Inductor</td><td>L_f</td><td>2 mH</td></tr>
<tr><td colspan="2">Filter Capacitor</td><td>C_f</td><td>1 mF</td></tr>
<tr><td colspan="2">Line Resistance</td><td>$R_{1\sim4}$</td><td>0.01 Ω</td></tr>
<tr><td rowspan="5">Primary Controller</td><td>Droop Gain</td><td colspan="2">d_1=1, d_2=2, d_3=3, d_4=4</td></tr>
<tr><td rowspan="2">Voltage Loop</td><td>K_{VP}</td><td>0.9</td></tr>
<tr><td>K_{VI}</td><td>130</td></tr>
<tr><td rowspan="2">Current Loop</td><td>K_{IP}</td><td>0.3</td></tr>
<tr><td>K_{II}</td><td>3</td></tr>
<tr><td colspan="2" rowspan="4">Secondary Controller</td><td>k_1</td><td>20</td></tr>
<tr><td>k_2</td><td>5</td></tr>
<tr><td>β</td><td>2</td></tr>
<tr><td>θ</td><td>0.8</td></tr>
</table>

5.3.1 Case 1: Constant Power Load and Resistive Load Step Changes

The control efficacy of the proposed distributed event-triggered fixed-time secondary control strategy for DC microgrids is thoroughly evaluated through a comprehensive simulation scenario encompassing various load conditions. The scenario unfolds in six distinct stages, designed to assess the system's response to both CPL and resistive load variations:

Stage Breakdown:

Stage 1 (0-2s): The simulation begins with the connection of a CPL P_{L1} = 3500W and a resistive load R_1 = 60Ω to the DC bus, with only primary droop control operational from the start.

Stage 2 (2-4s): The secondary control strategy is activated at the 2-second mark to assess its impact on system stability and load management.

Stage 3 (4-6s): An additional CPL P_{L2} = 2000W is introduced to the DC bus at 4 seconds to simulate an increase in load demand.

Stage 4 (6-8s): The P_{L2} load is disconnected at 6 seconds, testing the system's adaptability to decreasing load conditions.

Stage 5 (8-10s): A second resistive load R_2 = 60Ω is added at 8 seconds, further challenging the control strategy's load management capabilities.

Stage 6 (10-12s): The R_2 load is removed at 10 seconds, completing the cycle of load variations.

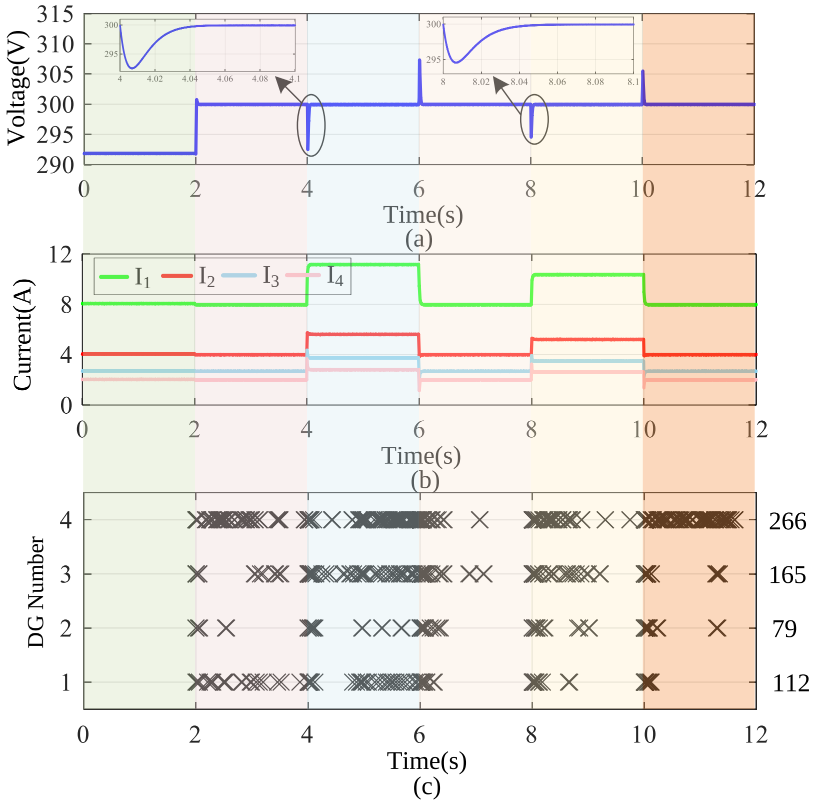

Fig. 5-3. Results under constant power load and resistive load steps. (a) DC bus voltage. (b) Output currents. (c) Triggering time instants.

Simulation Outcomes (Fig. 5-3):

- *DC Bus Voltage Stability (Fig. 5-3 (a))*: Initial operation under primary control exhibits noticeable voltage deviations. However, upon secondary control activation, the DC bus voltage stabilizes at its nominal value, showcasing the secondary control's ability to maintain voltage stability amidst load changes.
- *Proportional Current Sharing (Fig. 5-3 (b))*: The output currents of the four converters are effectively managed, maintaining the desired distribution ratio throughout the simulation, despite the dynamic load conditions.
- *Event-Triggering Instances (Fig. 5-3 (c))*: The triggering instances for event-triggered communication are displayed, highlighting a sparse distribution with an average of 155 triggers over 10 seconds for all DGs. The frequency of triggers is higher during transient states, aligning with theoretical expectations,

but notably decreases as the system approaches a steady state, reflecting the efficiency of the event-triggered mechanism in reducing unnecessary communication.

The simulation results validate the proposed control strategy's effectiveness in managing DC bus voltage stability and achieving proportional current sharing among DGs under varying load conditions. The event-triggered mechanism's performance, particularly in minimizing communication while ensuring timely system responses, underscores the proposed strategy's potential to enhance DC microgrid operations. The successful management of CPL and resistive load steps, combined with the sparse triggering pattern that reduces communication overhead, demonstrates the proposed control scheme's efficacy and practical applicability in dynamic microgrid environments.

5.3.2 Case 2: Comparison with Periodic Communication

The performance comparison between the proposed event-triggered control strategy and the conventional periodic communication-based control approach, as implemented in [92] under three different periodic communication intervals: T = 5ms, 13ms, and 16ms, is conducted to highlight the advantages of the event-triggered mechanism in terms of communication efficiency and system stability. Utilizing the same six-stage scenario as in Case 1, this comparison examines the system's response.

Key Observations from Simulation Results (Fig. 5-4):

- *Stable System Performance at Shorter Intervals (Fig. 5-4 (a) & Fig. 5-4 (b))*: When the periodic communication interval T is set to 5ms or 13ms, the simulation results reveal that the system's performance, particularly the output currents of the four DGs, remains consistent with those observed in Case 1. This indicates that at shorter communication intervals, the periodic communication mechanism can maintain system stability and performance effectively.
- *System Performance at Longer Interval (Fig. 5-4 (c))*: Increasing the communication interval to 16ms leads to noticeable fluctuations in the output currents of the DGs. While the system remains stable, the larger fluctuations

highlight the limitations of the periodic communication mechanism in maintaining optimal system performance at longer intervals.

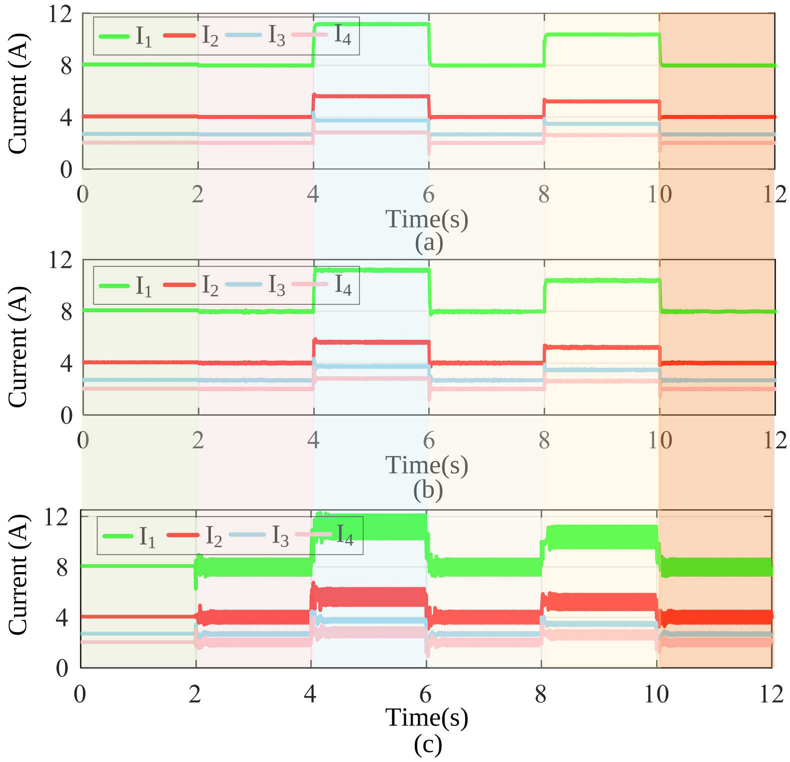

•

• Fig. 5-4. Output currents under the controller in [92] with different periodic communication intervals T. (a) T = 5ms. (b) T = 13ms. (c) T = 16ms.

Comparison of Communication Efficiency:

- *Periodic Communication Demand*: With a periodic communication interval of less than 16ms, each DG engages in more than 625 communications during the [2s, 10s] interval to maintain system stability and performance. This high frequency of communication underscores the significant communication burden associated with the periodic communication mechanism.
- *Event-Triggered Communication Efficiency*: In contrast, the proposed event-triggered control strategy averages 155 communications across all DGs during the same interval. This stark reduction in communication frequency demonstrates the event-triggered method's efficiency in minimizing unnecessary data transmissions while ensuring system performance.

The comparison elucidates the substantial advantages of the proposed event-triggered control strategy over conventional periodic communication methods.

Specifically, the event-triggered approach significantly reduces the number of signal transmissions required to maintain system stability and performance, thereby alleviating the communication burden on the microgrid's control network. This reduction in communication frequency not only enhances the scalability and efficiency of the microgrid system but also contributes to improved reliability and reduced energy consumption associated with communication processes. Consequently, the proposed event-triggered secondary control scheme emerges as a superior alternative, particularly in scenarios where minimizing communication overhead while maintaining desirable system performance is paramount.

5.3.3 Case 3: Performance under Communication Time Delay

This case study meticulously examines the impact of communication delays on the performance of the proposed event-triggered secondary control strategy for a DC microgrid. Following the structured approach of Case 1, the investigation focuses on how different levels of communication delay T_{delay} affect the stability and performance of the microgrid system. Specifically, the delays of 7ms, 12ms, and 17ms are evaluated to understand their influence on the system's dynamic response.

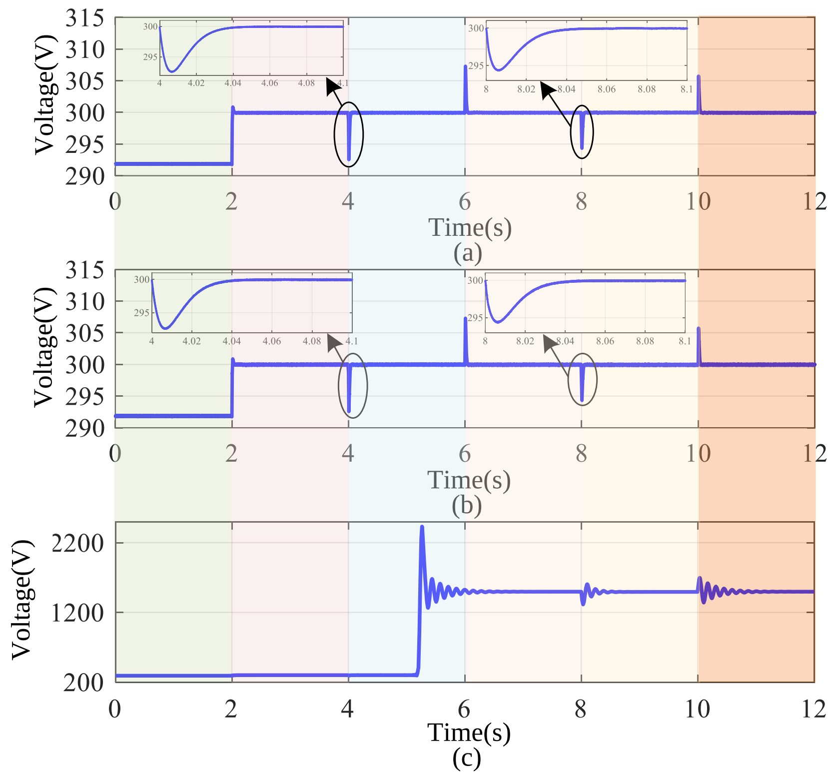

Fig. 5-5. DC bus voltage with different communication time delays T_{delay}. (a) T_{delay} = 7ms. (b) T_{delay} = 12ms. (c) T_{delay} = 17ms.

Observations from DC Bus Voltage Responses (Fig. 5-5):

- *Stability at Delays up to 12ms*: The simulation results indicate that the DC microgrid system maintains stability and exhibits satisfactory performance when the communication delay is kept at 12ms or below. The DC bus voltage responses under these conditions show that the system can effectively manage the delays, ensuring that the control objectives are met without significant deviations from the desired operational state.
- *Destabilization at a Delay of 17ms*: At a communication delay of 17ms, the system exhibits signs of destabilization, as evident from the DC bus voltage response. This instability highlights the sensitivity of the microgrid control system to extended communication delays, underscoring the critical importance of maintaining timely communication between the DGs for effective system regulation.

The findings from this case study underscore the robustness of the proposed event-triggered secondary control strategy within a communication delay threshold of 12ms. This threshold provides a valuable benchmark for the design and implementation of communication networks in DC microgrid systems, ensuring that the control strategy can accommodate inherent delays without compromising system stability.

In summary, the case study confirms the proposed control strategy's effectiveness in managing communication delays, with a notable tolerance up to 12ms.

5.3.4 Case 4: Plug and Play Performance

The plug-and-play functionality of the proposed distributed event-triggered fixed-time secondary control method for DC microgrids is critically assessed in this case study. The system initially operates with both primary and secondary controllers active, managing a CPL P_{CPL} = 5500W and a resistive load R_L = 30Ω on the common DC bus. The droop gains for the four DGs are set as d_1 = 1, d_2 = 3, d_3 = 3, and d_4 = 2, facilitating proportional current sharing based on these values.

Key Observations from Test Results (Fig. 5-6):

- *DC Bus Voltage Stability (Fig. 5-6 (a))*: Throughout the simulation, the DC bus voltage remains at its nominal value, demonstrating the effectiveness of the control strategy in maintaining voltage stability despite the dynamic changes associated with the plug-and-play operations of DGs.

- *Adaptive Current Sharing (Fig. 5-6 (b))*: The system exhibits excellent adaptability to the removal and reconnection of DGs. Specifically, when DG4 is detached at t = 4s, and similarly when DG2 is removed at t = 9s, the remaining DGs automatically adjust their output to maintain the desired current sharing ratio. Upon reconnection of DG4 at t = 6s and DG2 at t = 11s, the system swiftly reinstates the original current distribution among all four DGs, illustrating the seamless plug-and-play capability.

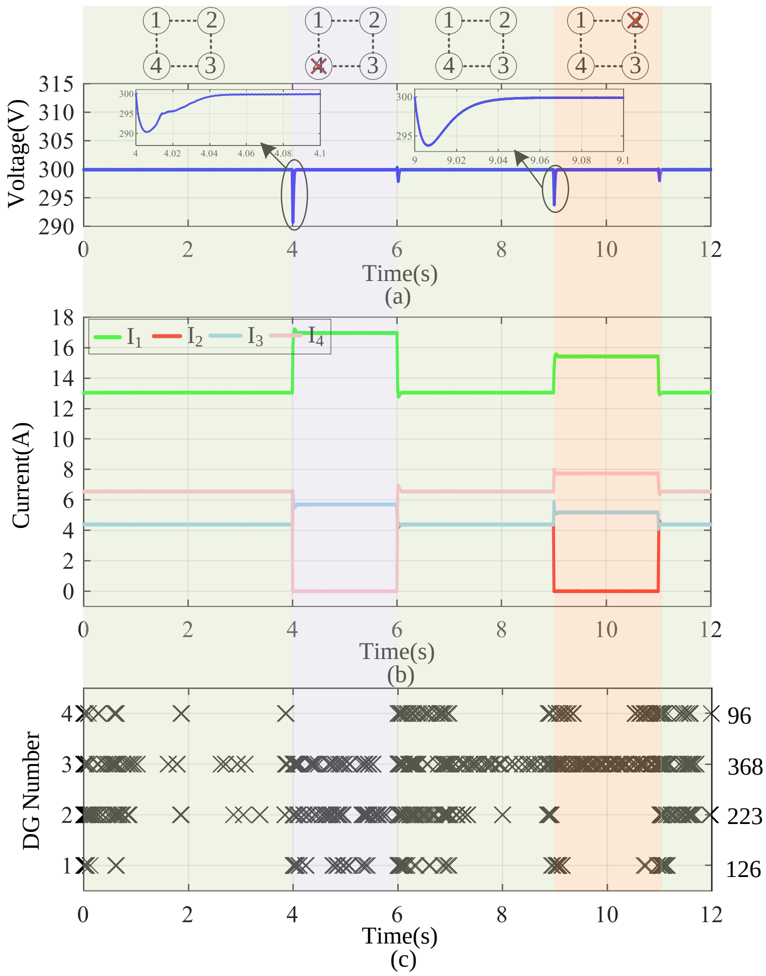

Fig. 5-6. Results under plug-and-play operations. (a) DC bus voltage. (b) Output currents of four DGs. (c) Triggering time instants.

- *Secondary Controller Triggering (Fig. 5-6 (c))*: Notably, the secondary controller for a removed DG (DG4 or DG2) ceases to trigger during its disconnection, eliminating unnecessary control actions. The controller is reactivated upon the DG's reintegration into the DC bus, further emphasizing the control strategy's efficiency and responsiveness to system configuration changes.

The proposed control strategy demonstrates exceptional plug-and-play functionality, a critical feature for modern DC microgrids that require flexibility in accommodating varying numbers of DGs without compromising system performance. The ability to maintain stable bus voltage and achieve proportional current sharing, even as DGs are dynamically added or removed, highlights the strategy's suitability for evolving microgrid environments. Furthermore, the efficient management of secondary controller triggers, aligning with the presence of DGs, underscores the method's practicality and adaptiveness, ensuring that control actions are both relevant and optimized for the current system configuration. This plug-and-play capability, combined with the reduced communication burden inherent in the event-triggered approach, positions the proposed strategy as a robust and efficient solution for the dynamic management of DC microgrids.

5.3.5 Case 5: Resilience to Communication Link Failure

This comprehensive case study explores the robustness and adaptability of the proposed control strategy for DC microgrids, with a particular emphasis on its performance during communication link failures among DGs. By simulating a scenario where the communication infrastructure is compromised, the study meticulously evaluates the resilience of the microgrid system. It focuses on the system's capacity to uphold consistent power sharing ratios and effective voltage regulation in the midst of communication fault disturbances, a critical aspect for the reliability of microgrid operations.

The design of the scenario takes into account various types of communication disruptions, to provide a thorough understanding of the control strategy's effectiveness under different conditions. This analysis is vital for ensuring that the microgrid can operate autonomously and efficiently, even when the normal flow of information between DGs is interrupted. Moreover, the findings aim to demonstrate that, despite the challenges posed by communication link disruptions, the proposed control strategy can maintain a high level of operational integrity, ensuring that the microgrid continues to deliver reliable and stable power to its loads. This resilience is key to advancing microgrid technologies, making them more viable and dependable for widespread use, particularly in areas susceptible to communication uncertainties or in critical applications where continuous power supply is essential.

System Configuration and Event Timeline:

Initial conditions involve connecting a CPL P_{CPL} = 3500W and a resistive load R = 60Ω to the DC bus, with droop gains for the four DGs set as d_1=1, d_2=3, d_3=2, d_4= 4 to ensure differentiated response characteristics.

At t = 2s, the proposed secondary controller is activated, enhancing the system's capability to manage load distribution and voltage stability. Communication link failures are introduced at t = 4s between DG1 and DG4, and subsequently at t = 7s between DG2 and DG3, to simulate potential network disruptions.

Observations from Simulation Results (Fig. 5-7):

- *Power Sharing Stability (Fig. 5-7 (b))*: Despite the breakdown of communication links, the system successfully maintains the predefined power sharing ratio among the DGs. This resilience is attributed to the secondary controller's integrator, which retains the compensating signal $u_i(t)$ just before the disruption, ensuring continuous adherence to the desired distribution. To show the power sharing ratio change, the extra load power disturbances are executed. From Fig. 5-7, it can be seen that when the communication link between DG1 and DG4 is broken, the system communication network is still fully connected. Consequently, even if another CPL P_{CPL}=2000W is added at t=5s and removed at t=6s, the accurate power sharing ratio can still be guaranteed. After the communication link between DG2 and DG3 is also broken, the original communication network is split into two separate ones. The power sharing ratio is not affected during [7s, 8s], since the compensating signal $u_i(t)$ (i = 1, …, 4) prior to the communication link fault is recorded and utilized. After another resistive load R = 60Ω at t = 8s is added, the original power sharing ratio cannot be guaranteed and the load power is reallocated among four DGs according to the new communication network topology. Specifically, DG1 and DG2 share current with ratio 3:1, and DG3 and DG4 share current with ratio 2:1. Therefore, the system's ability to adapt to changes in the communication network's topology is evident. Following the severance of links, the microgrid effectively reconfigures the power sharing arrangement according to the new network structure, showcasing the control strategy's flexibility and adaptability.

- *Robust Voltage Regulation (Fig. 5-7 (a))*: The DC bus voltage remains stable and consistent with its nominal value throughout the simulation, including during periods of communication link failure. This demonstrates the voltage regulation robustness of the proposed control strategy, independent of the communication network's integrity.

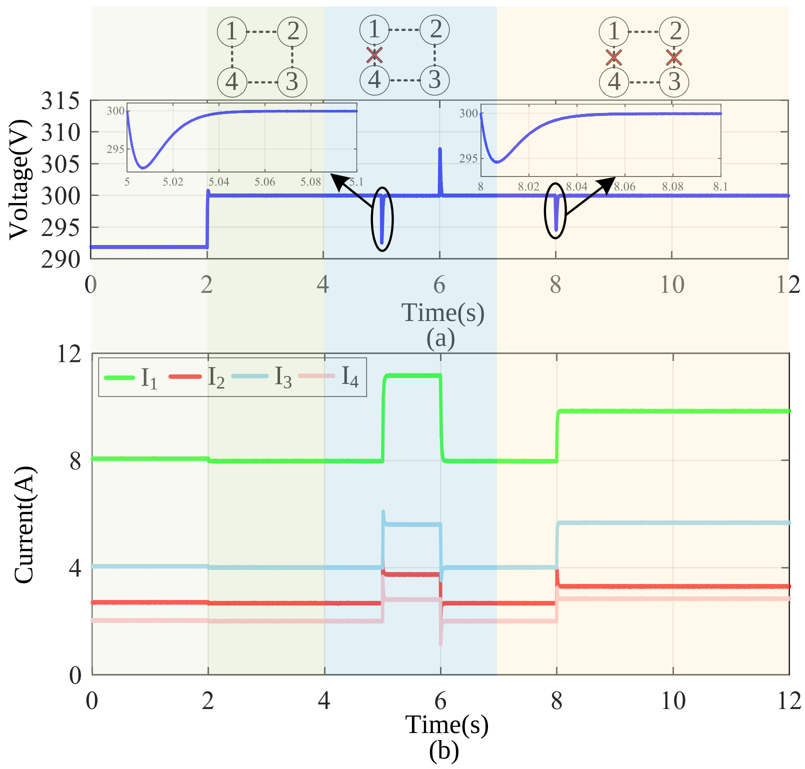

- Fig. 5-7. Resilience to communication link failure. (a) DC bus voltage. (b) Output currents of four DGs.

The case study highlights the proposed event-triggered secondary control strategy's effectiveness in ensuring reliable power sharing and voltage regulation within a DC microgrid, even in the face of communication link failures. The control method's resilience to network disruptions, coupled with its adaptability to changing network topologies, underscores its suitability for real-world microgrid applications where communication uncertainties may be prevalent. This robustness enhances the overall reliability and stability of the microgrid system, making the proposed control strategy a promising solution for managing distributed energy resources in dynamic and uncertain operational environments.

5.3.6 Case 6: Comparison with the State-of-the-Art Control Strategies

In this comparative case study, the performance of the proposed event-triggered control scheme is meticulously evaluated against two notable control strategies: the asymptotically stable event-triggered secondary controller detailed in [95] and the fixed-time secondary controller utilizing periodic communication as presented in [92]. Both of these comparative methods are designed to operate without the need for direct sampling of the bus voltage, aligning them with the proposed strategy in terms of reducing reliance on bus voltage information. For the control method in [95], parameters are configured with α = 20, β = 10, and each DG has an individual triggering threshold ε_i set to 0.05. This setup aims to optimize the performance of the event-triggered asymptotically stable control approach. The parameters for the fixed-time control strategy in [92] are set to α = 15, β = 15, and μ = 2, with a periodic communication interval of 10ms determined to achieve satisfactory control outcomes. The evaluation process adheres to the structured approach established in Case 1, ensuring a consistent basis for comparison across different control strategies. This structured approach facilitates a clear assessment of each method's efficacy in maintaining system stability, regulating bus voltage, and ensuring proportional current sharing among DGs under various operational scenarios.

Key Observations from Simulation Results (Fig. 5-8):

- *Settling Time and Voltage Stability (Fig. 5-8 (a))*: Both the proposed method and the method in [92] exhibit superior performance over the method in [95] concerning the settling time for DC bus voltage regulation. This quicker settling time is crucial for maintaining system stability and ensuring reliable power supply amidst varying load conditions. Moreover, the proposed method and [92] effectively minimize voltage drops or surges during load transitions, demonstrating robust voltage control capabilities.

- *Current Sharing Accuracy (Fig. 5-8 (b))*: The output current of DG1, representing system performance, shows that both the proposed method and the one in [92] achieve precise current sharing among the DGs. This accuracy is vital for equitable load distribution and optimal utilization of generation resources within the microgrid.

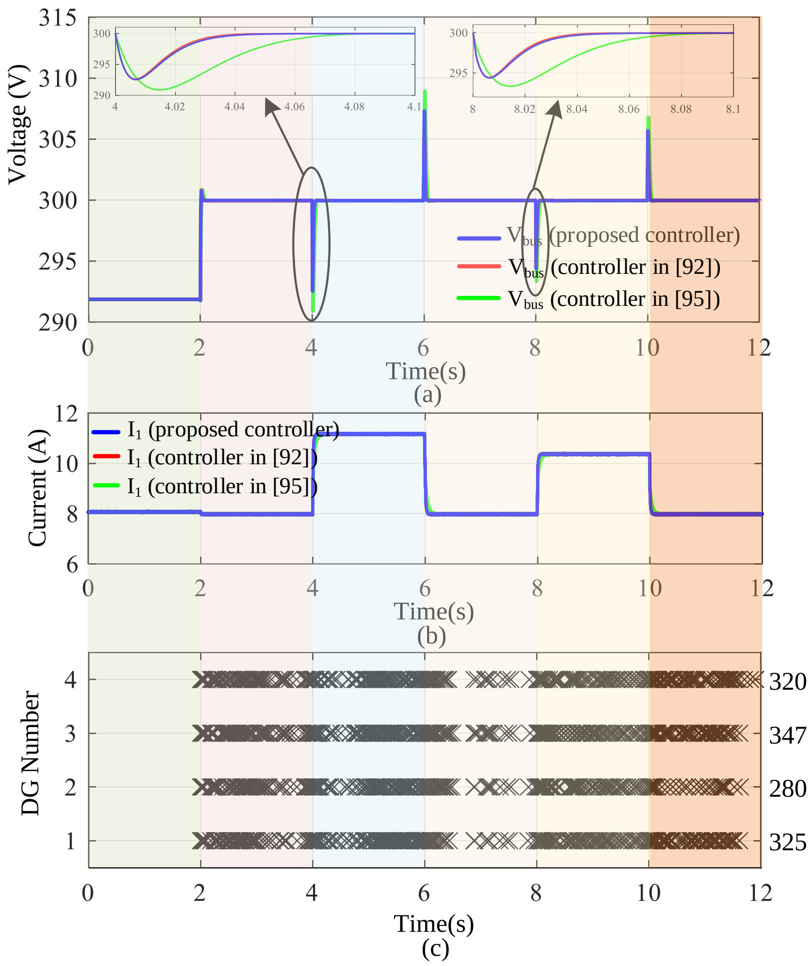

- Fig. 5-8. Performance comparison. (a) DC bus voltage. (b) Output current of DG1. (c) Triggering time instants of the controller in [95].

- *Communication Efficiency (Fig. 5-8 (c))*: While the dynamic and steady-state performances of the proposed method and [92] are comparable, a significant difference lies in their communication requirements. The proposed event-triggered control strategy necessitates an average of 155 communications between DGs during the [2s, 10s] interval, substantially fewer than the 1000 communications required by the periodic communication approach in [92]. The method in [95] falls in between, with an average of 318 triggering instances during the same interval, which is higher than the proposed method.

Consequently, the simulation results affirm the efficacy of the proposed event-triggered fixed-time control strategy in achieving fast and accurate system response with considerably reduced communication traffic. Compared to the control methods in [95] and [92], the proposed method offers a balanced solution that does not compromise on system performance while significantly alleviating the communication burden. This balance is critical for scalable and efficient microgrid operations, especially in larger systems where communication resources are limited. The reduced communication demand not only enhances system scalability but also contributes to improved reliability by minimizing the risk of network congestion and communication-related failures.

5.4 Experimental Results

The experimental validation of the proposed distributed event-triggered fixed-time secondary control strategy marks a pivotal moment in affirming its practicality and efficiency within real-world scenarios. The intricate experimental framework, as depicted in Fig. 5-9, serves as a scaled-down model of a DC microgrid, meticulously crafted to emulate the operational dynamics and complexities encountered in full-scale systems. This scaled model includes multiple DGs and loads, all interconnected to replicate the intricate interactions and dependencies found in actual microgrid environments. The setup is engineered to test the control strategy under a variety of conditions, including fluctuating loads, potential information transmission delays, thereby providing comprehensive insights into its performance and resilience. By closely mirroring the conditions and challenges inherent in larger systems, the experimental model ensures that the findings are both relevant and transferable to real-world applications. This holistic approach to validation underscores the potential of the control strategy to enhance the reliability, efficiency, and sustainability of DC microgrids, paving the way for more widespread adoption and integration of renewable energy sources into the power grid. Through this rigorous experimental validation, the proposed control strategy demonstrates its readiness to contribute to the advancement of smart grid technologies.

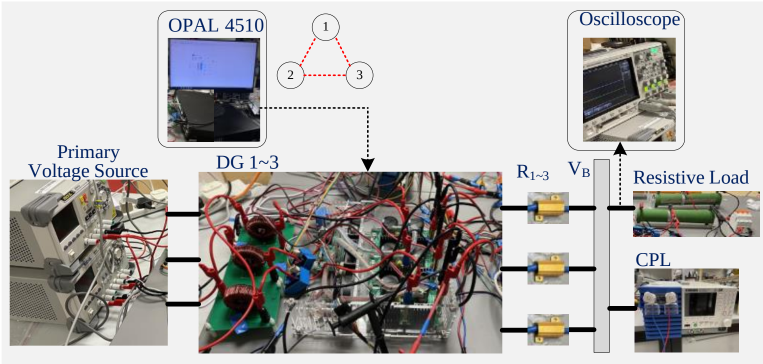

Fig. 5-9. Experimental setup.

Experimental Setup Overview:

DC Microgrid Configuration: The laboratory-scale DC microgrid comprises three boost converters, which are essential components for stepping up the DC voltage to the required levels. These converters represent the DGs in a typical microgrid setup, each equipped with power electronic switching capabilities to manage power flow efficiently.

Communication Network: A ring-based communication network interconnects the converters, facilitating the exchange of control signals and system information. This network topology is chosen for its simplicity and reliability, ensuring robust communication among the converters for coordinated control actions.

Control Implementation: The OPAL 4510, a specialized hardware platform, is employed to execute the control algorithms and generate the necessary pulse-width modulation (PWM) signals for the boost converters. This platform provides the computational power and flexibility needed to implement the proposed control strategy in real-time.

The experimental verification of the proposed control strategy, as detailed in this section, is instrumental in bridging the gap between theoretical research and practical implementation. By demonstrating the control strategy's effectiveness in a laboratory-scale DC microgrid, the experiments provide valuable insights into its potential for broader application in larger, more complex microgrid systems.

The parameters pertaining to the experimental arrangement and primary and secondary controllers are detailed in Table 5-2.

Table 5-2 System parameters in experiment

<table>
<tr><td colspan="2"></td><td colspan="2">DG 1 ~ DG 3</td></tr>
<tr><td colspan="2">DC Voltage Source</td><td>V_{DC}</td><td>24 V</td></tr>
<tr><td colspan="2">Rated DC Bus Voltage</td><td>V^*</td><td>48 V</td></tr>
<tr><td colspan="2">Switching Frequency</td><td>f_{sw}</td><td>20 kHz</td></tr>
<tr><td colspan="2">Filter Inductor</td><td>L_f</td><td>3 mH</td></tr>
<tr><td colspan="2">Filter Capacitor</td><td>C_f</td><td>2 mF</td></tr>
<tr><td colspan="2">Line Resistance</td><td>$R_{1\sim3}$</td><td>0.1 Ω</td></tr>
<tr><td rowspan="5">Primary Controller</td><td>Droop Gain</td><td colspan="2">d_1=4, d_2=4, d_3=8</td></tr>
<tr><td rowspan="2">Voltage Loop</td><td>K_{VP}</td><td>1.1</td></tr>
<tr><td>K_{VI}</td><td>45</td></tr>
<tr><td rowspan="2">Current Loop</td><td>K_{IP}</td><td>0.2</td></tr>
<tr><td>K_{II}</td><td>30</td></tr>
<tr><td colspan="2" rowspan="4">Secondary Controller</td><td>k_1</td><td>30</td></tr>
<tr><td>k_2</td><td>10</td></tr>
<tr><td>β</td><td>2</td></tr>
<tr><td>θ</td><td>0.9</td></tr>
</table>

5.4.1 A. Experimental Results with Resistive Load

In this case, the experimental validation of the proposed distributed event-triggered fixed-time secondary control strategy under resistive load conditions offers critical insights into its practical applicability and effectiveness. The experiment is meticulously designed to assess the controller's performance in maintaining DC bus voltage stability and ensuring appropriate current sharing among DGs in response to load variations.

Experimental Procedure and Observations:

- *Initial Setup*: The experiment begins with the DC microgrid connected to a resistive load of 30Ω, with the primary control mechanism engaged. This initial phase allows for the observation of the system's baseline response to load conditions without secondary control intervention.
- *Voltage Deviation Under Primary Control*: As depicted in Fig. 5-10 (a), the engagement of only the primary control results in the DC bus voltage dropping to approximately 45V, indicating a noticeable deviation from the nominal voltage value V^* = 48V. This deviation underscores the limitations of primary

control in compensating for load-induced voltage changes.

- *Activation of Secondary Control*: The proposed secondary controller is then activated, leading to a rapid restoration of the DC bus voltage to its nominal value. This swift response highlights the secondary control's capability to enhance voltage regulation and stability effectively.
- *Dynamic Load Variation*: The resistive load is subsequently modified from 30Ω to 15Ω and then reverted to 30Ω, simulating dynamic load conditions. Throughout these changes, Fig. 5-10 (a) illustrates that the DC bus voltage is promptly regulated back to V^* = 48V, and the current sharing among DG1 to DG3 is efficiently managed, demonstrating the system's adaptability and robustness under varying loads.
- *Triggering Time Instants*: Fig. 5-10 (b) presents the triggering time instants for DG1 to DG3, indicating the activation of the event-triggered mechanism. The occurrence of triggers in the steady state, attributed to measurement errors and sensor noise, validates the functionality of the event-triggered control in a real-world setting, ensuring communication efficiency without compromising control objectives.
- *Performance Comparison*: To demonstrate the superiority of the proposed method, the zoomed-in view of DC bus voltage dynamic responses with the proposed method, the method in [92] and the method in [95] when the load changes from 30Ω to 15Ω is shown in Fig. 5-10 (c). It can be seen that the settling time with the proposed method and the method in [92] is about 110ms, which is much shorter than that of 175ms with the method in [95]. For the number of triggering communication, we only count the triggers occurring within 2 seconds after the load changes from 30Ω to 15Ω for ease of comparison. From Fig. 5-10 (d), the average communication number of the proposed method is 65 during 2s with only one variable transmitted each time, while that in [92] is 200 during 2s with two variables transmitted each time. For the method in [95], the average triggering number is 97 during 2s, which is larger than the average triggering times in our proposed controller.

The experimental outcomes provide compelling evidence of the proposed secondary controller's efficacy in managing DC bus voltage and current sharing under resistive load conditions. The controller's ability to rapidly adjust to nominal voltage levels following load changes, coupled with its efficient event-triggered communication mechanism, underscores its potential for enhancing the operational stability and efficiency of DC microgrids. The successful experimental validation in a practical setup reinforces the proposed control strategy's viability for broader application in diverse microgrid environments, catering to dynamic operational demands and ensuring system resilience.

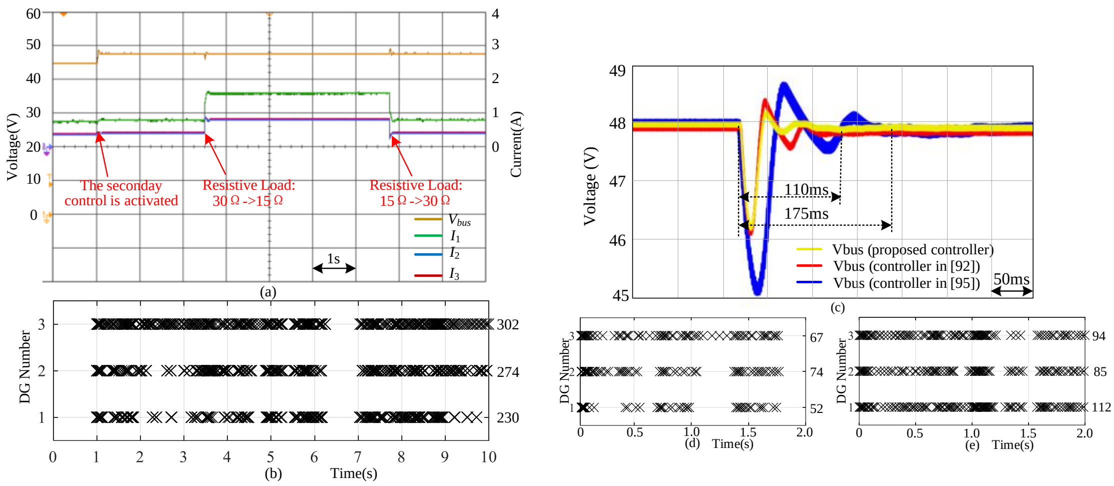

Fig. 5-10. Experiment results with resistive load. (a) DC bus voltage and output current of each DG. (b) The triggering time instants of three DGs. (c) The zoomed-in view of DC bus voltages with different control methods when the load changes from 30Ω to 15Ω. (d) The triggering time instants under the proposed method with the load change from 30Ω to 15Ω. (e) The triggering time instants under the method in [95] with the load change from 30Ω to 15Ω.

5.4.2 B. Experimental Results with CPL

This experiment is designed to test the controller's ability to regulate DC bus voltage and manage current sharing among DGs amidst variations in CPL.

Experimental Procedure and Observations:

- *Initial Conditions*: The experiment commences with the microgrid connected to a 30Ω resistive load and a 50W constant power load, while only the primary droop control is active. This initial phase sets the baseline for assessing the system's response to CPL changes without the intervention of the secondary control.

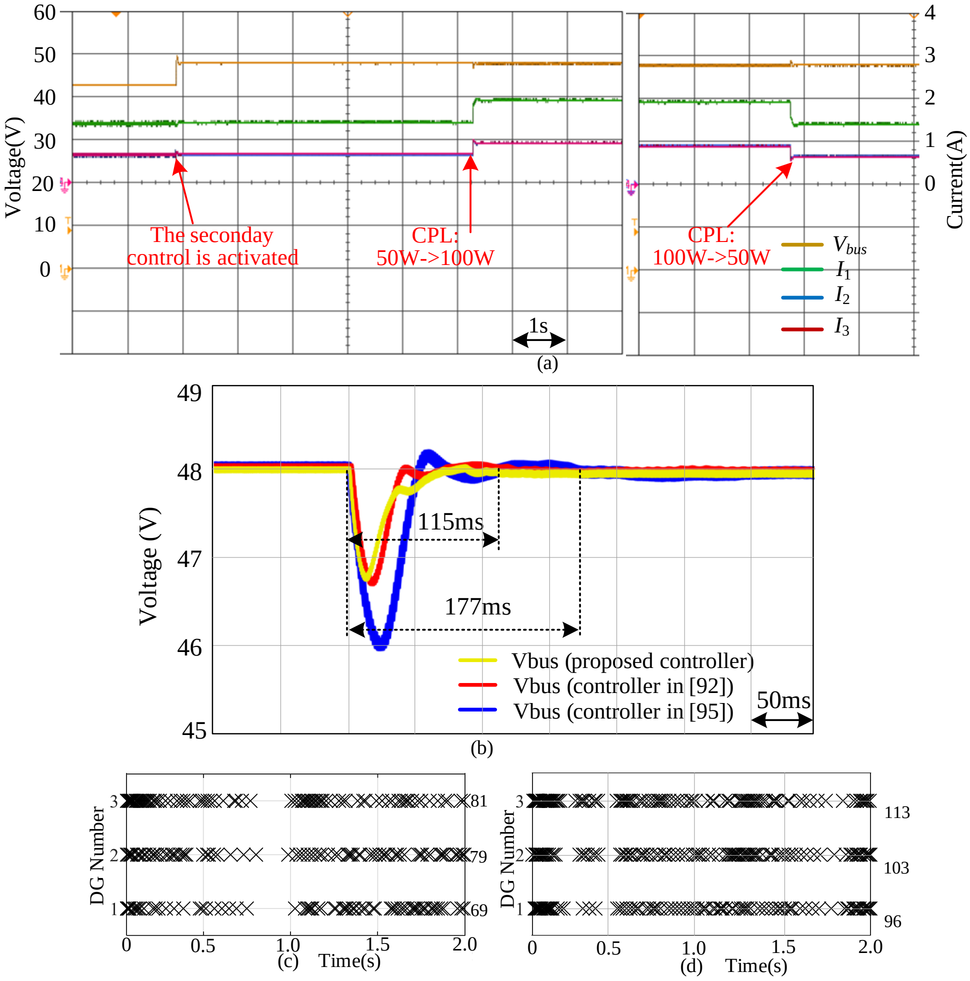

Fig. 5-11. Experimental results with CPLs. (a) DC bus voltage and output current of each DG. (b) The zoomed-in view of DC bus voltages with different control methods when the CPL changes from 50W to 100W. (c) The triggering time instants under the proposed method with the CPL change from 50W to 100W. (d) The triggering time instants under the method in [95] with CPL change from 50W to 100W.

- *Voltage Deviation under Primary Control*: Initially, the DC bus voltage measures approximately 43V, indicating a significant deviation from the desired 48V. This underscores the primary control's limitations in compensating for the effects of CPL on bus voltage.
- *Secondary Control Activation*: Upon activating the proposed secondary control, the DC bus voltage is rapidly regulated back to the nominal 48V, showcasing the secondary control's effectiveness in restoring voltage levels in response to CPL-induced disturbances.

- *CPL Variation*: The constant power load is then adjusted to 100W and subsequently reduced back to 50W, simulating a range of load conditions. Throughout these variations, as depicted in Fig. 5-11, the system successfully maintains voltage stability at 48V and ensures efficient current sharing among the DGs, demonstrating adaptability to changing load dynamics.
- *Performance Comparison*: The enlarged view of DC bus voltage dynamic responses with the proposed method, the method in [92] and the method in [95] when the CPL step increases from 50W to 100W is shown in Fig. 5-11 (b) to demonstrate the advantage of the proposed method. It is observed that the settling time with the proposed method and the method in [92] are about 115ms, which is much shorter than that of 177ms with the method in [95]. For the communication triggering number, only the triggers occurring within 2 seconds after the CPL changes from 50W to 100W are counted to facilitate comparison. From Fig. 5-11 (c), the average communication number of the proposed method is 76 during 2s with only one variable transmitted each time, while that in [92] is 200 during 2s with two variables transmitted each time. For the method in [95], the average triggering number is 104 during 2s from Fig. 5-11 (d), which results in more communication triggering times than our proposed controller.

The experimental results validate the proposed secondary control strategy's capability to effectively manage DC bus voltage and current distribution in the presence of CPL variations. The swift and accurate voltage restoration following CPL changes, coupled with the maintained current sharing, highlights the controller's robustness and reliability.

5.4.3 Experimental Results with Communication Time Delay

The evaluation of the proposed control scheme under varying communication time delays is crucial to understand its robustness and reliability in real-world scenarios where delays are inevitable. This case study specifically investigates the impact of communication delays on the control scheme's ability to manage DC bus voltage and current sharing in a DC microgrid equipped with resistive and CPLs.

Experimental Setup and Procedure:

The experiment commences with the DC microgrid connected to a 30Ω resistive load and a 50W CPL, with the secondary controller already activated to manage the system's response. To simulate a dynamic load environment, the CPL is then increased to 100W, challenging the control scheme's adaptability. Tests are conducted with three different communication delays T_{delay}: 8ms, 10ms, and 12ms, to assess the control scheme's performance under varying levels of communication latency.

Observations from Experimental Results (Fig. 5-12):

- *Performance at T_{delay} = 8ms*: At this communication delay, the control scheme's performance closely mirrors the results observed in part 5.4.2 (without communication delay), indicating that the controller effectively compensates for this level of delay, maintaining near-optimal voltage restoration and current sharing.
- *Impact of Increasing Delays*: As the communication delay is extended to 10ms and further to 12ms, a noticeable degradation in the controller's performance is observed. This is manifested in the form of longer transient settling times and less precise voltage and current regulation, highlighting the sensitivity of the control scheme to communication latencies.
- *Threshold for Communication Delay*: Based on the experimental outcomes, it is inferred that a communication delay threshold of less than 8ms is essential for ensuring the proposed control scheme's satisfactory performance in terms of voltage restoration and current sharing under the given experimental conditions.

The case study underscores the importance of minimizing communication delays in the effective implementation of the proposed secondary control scheme for DC microgrids. While the control scheme shows resilience to delays up to 8ms, further increases in delay time compromise system performance, emphasizing the need for efficient communication strategies to support the real-time operation of advanced control schemes in microgrids. Addressing communication delays is pivotal in enhancing the robustness and reliability of microgrid control systems, ensuring stable operation even in dynamically changing load conditions and communication environments.

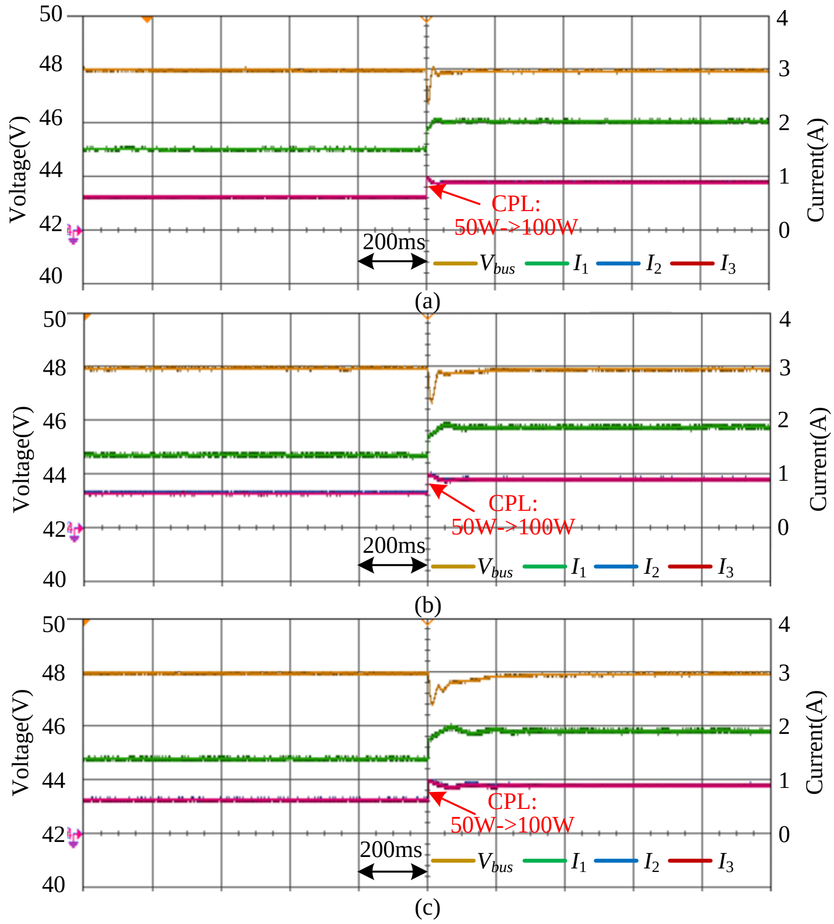

Fig. 5-12. Experimental results with different communication time delays. (a) T_{delay} = 8ms. (b) T_{delay} = 10ms. (c) T_{delay} = 12ms.

5.5 Conclusion

This chapter introduces a novel distributed event-triggered fixed-time secondary control strategy tailored for islanded DC microgrids. The strategy stands out due to its innovative approach to achieving rapid and reliable voltage recovery and current sharing within a predetermined time frame, thereby enhancing the operational stability and efficiency of DC microgrids.

Key Contributions and Findings:

1. *Fixed-Time Stability*: Utilizing fixed-time stability theory, the proposed control scheme guarantees that critical control objectives—voltage recovery and proportional current sharing among DGs—are met within a specified settling time, irrespective of initial conditions.

2. *Event-Triggered Communication*: The implementation of an event-triggered

communication mechanism minimizes the need for continuous signal exchanges between DGs. This approach significantly reduces communication traffic, mitigating the risk of network congestion and enhancing system scalability without compromising control performance.

3. *Independence from DC Bus Voltage Measurement*: A distinctive feature of the proposed strategy is its operational independence from direct DC bus voltage measurements. By eliminating the need for voltage sensors on the DC bus, the control method simplifies system architecture and increases reliability by reducing the dependency on sensor accuracy and availability.

4. *Stability and Zeno Behavior Prevention*: The stability of the proposed controller is rigorously validated using Lyapunov stability theory, ensuring that the system remains stable under the designed control laws. Additionally, the control strategy effectively addresses and prevents the occurrence of Zeno behavior, a critical consideration for the practical implementation of event-triggered systems.

5. *Superior Performance*: Comparative analyses, both through simulation and experimental studies, demonstrate that the proposed control strategy offers a rapid dynamic response and requires fewer information exchanges than existing control methods. This performance advantage is evident in the system's ability to maintain voltage and current regulation under various operational scenarios, including load changes and communication delays.

To sum up, the proposed distributed event-triggered fixed-time secondary control strategy represents a significant advancement in the control of islanded DC microgrids. By combining fixed-time stability with efficient event-triggered communication, the strategy offers a robust solution for enhancing microgrid performance while reducing the operational and communication complexities traditionally associated with microgrid management. The theoretical foundation, coupled with empirical validation, underscores the proposed strategy's potential to improve the resilience, efficiency, and scalability of DC microgrid systems, paving the way for more reliable and sustainable energy distribution networks.

Chapter 6 Conclusions and Future Scope

6.1 Conclusions

The effective use of renewable energy stands as a crucial strategy to combat the dual threats of energy scarcity and climate change. However, the large-scale integration of renewable energy presents new challenges to the existing operational control and grid regulation. In view of this, a series of decentralized and distributed control strategies are proposed for both power converters and microgrids to support renewable energy development in this thesis. Specifically, the thesis focuses on four technical aspects: the circulating current suppression in PV grounding faults, the circulating current suppression between IPOP inverters, the fast-dynamic response of DC microgrids, and the communication overhead reduction in the secondary control of DC microgrids.

The main conclusions are drawn as follows:

1. A comprehensive decentralized control scheme is proposed for grid-connected PV systems to suppress circulating currents caused by the grounding faults in PV modules. The control strategy for mitigating circulating currents on the AC side and DC side of grid-connected PV systems are both deliberately designed, respectively, to achieve the circulating currents suppression in both the steady state and transient state. Through this holistic approach, the adverse effects of PV grounding faults are effectively mitigated, enabling the system to maintain normal operation without isolating the affected sections, even in the event of a grounding fault. The strategy is inherently decentralized and scalable, making it suitable for PV systems with N (N > 2) modules. Finally, the HIL testing is conducted to substantiate the theoretical claims.

2. A wholly decentralized control approach, utilizing an enhanced 3LNPCI topology, is proposed to mitigate circulating currents within IPOP single-phase half-bridge 3LNPCIs. The mathematical model for the currents in IPOP 3LNPCIs, facilitating an extensive examination of the various factors influencing these currents and uncovering the dual control objectives inherent to IPOP 3LNPCIs' operation is

formulated. The deficiencies of traditional half-bridge 3LNPCIs are also highlights. A revised 3LNPCI design featuring dual modulation degrees is proposed and the corresponding control strategies are also designed. With the proposed strategy, the CC suppression and proportional current sharing can be achieved simultaneously. The efficacy of this innovative approach is substantiated through experimental trials, demonstrating the viability of the proposed solution.

3. A distributed fixed-time secondary control approach is proposed for islanded DC microgrids to achieve fast dynamic response and less signal transmissions. The proposed method is capable of concurrently achieving voltage regulation and desired current distribution ratio within a fixed time, demonstrating a fast dynamic response. Distinctively, this method necessitates the transmission of only a single variable among adjacent nodes, in contrast to previous strategies that required two variables. This reduction in communication complexity not only streamlines the control process but also enhances the overall system efficiency. The superiority of this approach is substantiated through comprehensive simulation tests.

4. A distributed event-triggered fixed-time secondary control is proposed to further reduce communication traffic. Compared to the control scheme proposed in Chapter 4, this control strategy can further lessen the communication overhead. The development and execution of an event-triggered communication protocol among DGs have been meticulously undertaken. The stability of the suggested control mechanism is firmly validated, with its practicality underscored through its proven efficacy in averting Zeno phenomena. Exhibiting a swift dynamic performance and a reduction in data exchange relative to existing approaches, the effectiveness of the proposed controller is corroborated by both simulation and experimental findings.

In summary, in response to the practical challenges associated with large-scale development and utilization of renewable energy sources, this thesis has developed a range of decentralized and distributed control strategies from the power converter level and the microgrid level, respectively. *For power converter-level control*, the proposed methods are entirely decentralized, enabling plug-and-play capability that enhances the flexibility and reliability of renewable energy generation systems.

Compared with the existing methods, the proposed approaches can effectively address issues such as overcurrent and system instability caused by PV grounding faults and circulating currents within input-parallel-output-parallel systems, avoiding the possible downtime, and thus enabling the maximum utilization of renewable energy sources. Moreover, the proposed methods can be extended to different power converter topologies and provide a general framework for addressing problems such as PV grounding faults and circulating currents in renewable energy generation systems. *For microgrid-level control*, different from existing methods, the proposed distributed control approaches can significantly reduce signal transmission and communication traffic while ensuring rapid dynamic response of the system, simplifying the system's communication infrastructures and facilitating implementation. Consequently, the proposed methods can substantially lower communication costs, supporting the future large-scale and low-cost utilization of renewable energy resources.

6.2 Future Scope

Based on the achievements made in this research, several directions for further research can be suggested as below:

1. To demonstrate the instability phenomena of PV systems under grounding faults, only the qualitative analysis of the circulating currents caused by PV grounding faults is carried out. This is not conducive to the in-depth study of the generation mechanism and influencing factors of circulating currents. Therefore, the detailed modeling and quantitative analysis of circulating currents are of importance to delve into the impact of grounding faults.

2. To increase the modulation degree of the conventional 3LNPCI, the modified 3LNPCI topology needs extra switches, which will increase the hardware costs. How to design a new inverter topology that has enough modulation freedom to suppress the CCs generated in IPOP structure, has fewer switches, and retains the characteristics of three-level inverter is worth studying.

3. As the scale of microgrids expands and system performance requirements become more stringent, the rapidity of convergence emerges as one of the crucial metrics for evaluating distributed secondary control methodologies. In this context, the evolution of distributed control algorithms within microgrid secondary control has progressed from achieving asymptotical convergence, to finite-time convergence, and further to fixed-time convergence. However, the upper bound of the convergence time of the fixed-time algorithm depends on multiple parameters and is difficult to calculate. Therefore, the predefined-time control, whose convergence time depends on only one pre-specified time parameter, simplifying the convergence time design, is worth investigating in DC microgrids.

4. The event triggering conditions in the proposed event-triggered fixed-time secondary control strategy is static. It means that the signal transmission intervals cannot vary along with the varying system state variables. To further reduce the data transmission, the dynamic event-triggered control is worth consideration. This method can adjust the triggering instants based on changes in system states, thereby further reducing the number of communications. Therefore, how to design a dynamic event-triggered fixed-time secondary control strategy needs further study.

References

[1] T. B. Johansson, K. McCormick, L. Neij, and W. C. Turkenburg, “The potentials of renewable energy,” in *Renewable Energy: Routledge*, 2012, pp. 43-75.

[2] M. Liserre, T. Sauter, and J. Y. Hung, “Future Energy Systems: Integrating Renewable Energy Sources into the Smart Power Grid Through Industrial Electronics,” *IEEE Ind. Electron. Mag.*, vol. 4, no. 1, pp. 18–37, Mar. 2010.

[3] F. Z. Peng, C.-C. Liu, Y. Li, A. K. Jain, and D. Vinnikov, “Envisioning the Future Renewable and Resilient Energy Grids—A Power Grid Revolution Enabled by Renewables, Energy Storage, and Energy Electronics,” *IEEE J. Emerg. Sel. Top. Ind. Electron.*, vol. 5, no. 1, pp. 8–26, Jan. 2024.

[4] H. Xie, S. Zheng, and M. Ni, “Microgrid Development in China: A method for renewable energy and energy storage capacity configuration in a megawatt-level isolated microgrid,” *IEEE Electrification Mag.*, vol. 5, no. 2, pp. 28–35, Jun. 2017.

[5] D. T. Ton and M. A. Smith, “The U.S. Department of Energy’s Microgrid Initiative,” *Electr. J.*, vol. 25, no. 8, pp. 84–94, Oct. 2012.

[6] “Renewable capacity statistics 2023,”. Available: https://www.irena.org/Publications/2023/Mar/Renewable-capacity-statistics-2023.

[7] Z. Liu, “Global energy interconnection,” *China Electr. Power Press*, 2015.

[8] W. Li and X. He, “Review of Nonisolated High-Step-Up DC/DC Converters in Photovoltaic Grid-Connected Applications,” *IEEE Trans. Ind. Electron.*, vol. 58, no. 4, pp. 1239–1250, Apr. 2011.

[9] Y. Shen, D. Zakzewski, A. Hasnain, R. Resalayyan, and A. Khaligh, “Sensorless Control for DC-Parallel Active Power Decoupling in PV Microinverters,” *IEEE Trans. Power Electron.*, vol. 38, no. 11, pp. 14628–14637, Nov. 2023.

[10] X. Zhou, C. Pang, X. Zeng, L. Jiang, and Y. Chen, “A Short-Term Power Prediction Method Based on Temporal Convolutional Network in Virtual Power Plant Photovoltaic System,” *IEEE Trans. Instrum. Meas.*, vol. 72, pp. 1–10, 2023.

[11] S. Chakraborty, G. Modi, B. Singh, and B. K. Panigrahi, “Control of a Grid-Tied Battery-Less Two-Stage Solar PV System With Seamless Transition and Autonomous Dispatch Capability,” *IEEE Trans. Ind. Appl.*, vol. 59, no. 6, pp. 7669–7680, Nov. 2023.

[12] A. Iovine, M. J. Carrizosa, G. Damm, and P. Alou, “Nonlinear Control for DC Microgrids Enabling Efficient Renewable Power Integration and Ancillary Services for AC Grids,” *IEEE Trans. Power Syst.*, vol. 34, no. 6, pp. 5136–5146, Nov. 2019.

[13] M. G. M. Abdolrasol, M. A. Hannan, A. Mohamed, U. A. U. Amiruldin, I. B. Z. Abidin, and M. N. Uddin, “An Optimal Scheduling Controller for Virtual Power Plant and Microgrid Integration Using the Binary Backtracking Search Algorithm,” *IEEE Trans. Ind. Appl.*, vol. 54, no. 3, pp. 2834–2844, May 2018.

[14] S. Parhizi, H. Lotfi, A. Khodaei, and S. Bahramirad, “State of the Art in Research on Microgrids: A Review,” *IEEE Access*, vol. 3, pp. 890–925, 2015.

[15] A. Hirsch, Y. Parag, and J. Guerrero, “Microgrids: A review of technologies, key drivers, and outstanding issues,” *Renew. Sustain. Energy Rev.*, vol. 90, pp. 402–411, Jul. 2018.

[16] M. M. A. Abdelaziz and H. E. Farag, “An Enhanced Supervisory Control for Islanded Microgrid Systems,” *IEEE Trans. Smart Grid*, vol. 7, no. 4, pp. 1941–1943, Jul. 2016.

[17] M. Zolfaghari, M. Abedi, and G. B. Gharehpetian, “Power Flow Control of Interconnected AC–DC Microgrids in Grid-Connected Hybrid Microgrids Using Modified UIPC,” *IEEE Trans. Smart*

Grid, vol. 10, no. 6, pp. 6298–6307, Nov. 2019.

[18] A. A. Eajal *et al.*, “A Bayesian Approach to the Reliability Analysis of Renewables-Dominated Islanded DC Microgrids,” *IEEE Trans. Power Syst.*, vol. 36, no. 5, pp. 4296–4309, Sep. 2021.

[19] A. Bani-Ahmed, M. Rashidi, A. Nasiri, and H. Hosseini, “Reliability Analysis of a Decentralized Microgrid Control Architecture,” *IEEE Trans. Smart Grid*, vol. 10, no. 4, pp. 3910–3918, Jul. 2019.

[20] S. T. Cady, A. D. Domínguez-García, and C. N. Hadjicostis, “A Distributed Generation Control Architecture for Islanded AC Microgrids,” *IEEE Trans. Control Syst. Technol.*, vol. 23, no. 5, pp. 1717–1735, Sep. 2015.

[21] H. Kirchhoff and K. Strunz, “Control and Stability of Modular DC Swarm Microgrids,” *IEEE J. Emerg. Sel. Top. Power Electron.*, vol. 10, no. 5, pp. 6274–6292, Oct. 2022.

[22] H. Abdelgabir, M. N. B. Shaheed, A. Elrayyah, and Y. Sozer, “A Complete Small-Signal Modelling and Adaptive Stability Analysis of Nonlinear Droop-Controlled Microgrids,” *IEEE Trans. Ind. Appl.*, vol. 58, no. 6, pp. 7620–7633, Nov. 2022.

[23] Y. Zhou, P. Zhang, and M. Yue, “Reachable Dynamics of Networked Microgrids With Large Disturbances,” *IEEE Trans. Power Syst.*, vol. 36, no. 3, pp. 2416–2427, May 2021.

[24] L. Che, M. Shahidehpour, A. Alabdulwahab, and Y. Al-Turki, “Hierarchical Coordination of a Community Microgrid With AC and DC Microgrids,” *IEEE Trans. Smart Grid*, vol. 6, no. 6, pp. 3042–3051, Nov. 2015.

[25] K. P. Schneider *et al.*, “Improving Primary Frequency Response to Support Networked Microgrid Operations,” *IEEE Trans. Power Syst.*, vol. 34, no. 1, pp. 659–667, Jan. 2019.

[26] J. W. Simpson-Porco, Q. Shafiee, F. Dörfler, J. C. Vasquez, J. M. Guerrero, and F. Bullo, “Secondary Frequency and Voltage Control of Islanded Microgrids via Distributed Averaging,” *IEEE Trans. Ind. Electron.*, vol. 62, no. 11, pp. 7025–7038, Nov. 2015.

[27] S. Moayedi and A. Davoudi, “Distributed Tertiary Control of DC Microgrid Clusters,” *IEEE Trans. Power Electron.*, vol. 31, no. 2, pp. 1717–1733, Feb. 2016.

[28] H. Xin, Z. Qu, J. Seuss, and A. Maknouninejad, “A self-organizing strategy for power flow control of photovoltaic generators in a distribution network,” *IEEE Trans Power Syst*, vol. 26, no. 3, pp. 1462-1473, Aug. 2011.

[29] K. Kawabe and K. Tanaka, “Impact of dynamic behavior of photovoltaic power generation systems on short-term voltage stability,” *IEEE Trans Power Syst*, vol. 30, no. 6, pp. 3416-3424, Nov. 2015.

[30] N. Kumar, I. Hussain, B. Singh, and B. K. Panigrahi, “Framework of maximum power extraction from solar PV panel using self predictive perturb and observe algorithm,” *IEEE Trans Sustain Energy*, vol. 9, no. 2, pp. 895-903, Apr. 2018.

[31] M. R. Jafari, M. Parniani, and M. H. Ravanji, “Decentralized Control of OLTC and PV Inverters for Voltage Regulation in Radial Distribution Networks With High PV Penetration,” *IEEE Trans. Power Deliv.*, vol. 37, no. 6, pp. 4827–4837, Dec. 2022.

[32] L. Wang, T. Wang, G. Huang, K. Wang, R. Yan, and Y. Zhang, “Softly Collaborated Voltage Control in PV Rich Distribution Systems with Heterogeneous Devices,” *IEEE Trans. Power Syst.*, pp. 1–12, 2023.

[33] D. Yang, H. Zhang, C. Liu, Z. Pei, L. Lin, and X. Song, “Novel High-Frequency Isolated Cascade PV Inverter Topology Based on Multibus DC Collection,” *IEEE J. Emerg. Sel. Top. Power Electron.*, vol. 9, no. 2, pp. 2122–2135, Apr. 2021.

[34] N. Tak and S. K. Chattopadhyay, “Two-Stage Three-Phase Transformerless Hybrid Multilevel Inverter for Solar PV Application,” *IEEE Trans. Ind. Electron.*, vol. 71, no. 6, pp. 5386–5398, Jun. 2024.

[35] S. Chakraborty, G. Modi, B. Singh, and B. K. Panigrahi, “Control of a Grid-Tied Battery-Less Two-Stage Solar PV System With Seamless Transition and Autonomous Dispatch Capability,” *IEEE Trans. Ind. Appl.*, vol. 59, no. 6, pp. 7669–7680, Nov. 2023.

[36] J. M. S. Callegari, A. F. Cupertino, V. de N. Ferreira, and H. A. Pereira, “Minimum DC-Link Voltage Control for Efficiency and Reliability Improvement in PV Inverters,” *IEEE Trans. Power Electron.*, vol. 36, no. 5, pp. 5512–5520, May 2021.

[37] J. W. Zapata, S. Kouro, G. Carrasco, H. Renaudineau, and T. A. Meynard, “Analysis of Partial Power DC–DC Converters for Two-Stage Photovoltaic Systems,” *IEEE J Emerg Sel Top. Power Electron*, vol. 7, no. 1, pp. 591-603, Mar. 2019.

[38] X. Xiong, C. K. Tse, and X. Ruan, “Bifurcation analysis of stand-alone photovoltaic-battery hybrid power system,” *IEEE Trans Circuits Syst Reg Pap.*, vol. 60, no. 5, pp. 1354-1365, May 2013.

[39] G.-S. Seo, J.-W. Shin, B.-H. Cho, and K.-C. Lee, “Digitally controlled current sensorless photovoltaic micro-converter for DC distribution,” *IEEE Trans Ind Informat*, vol. 10, no. 1, pp. 117-126, Feb. 2014.

[40] E. Mamarelis, G. Petrone, and G. Spagnuolo, “An hybrid digital-analog sliding mode controller for photovoltaic applications,” *IEEE Trans Ind Informat*, vol. 9, no. 2, pp. 1094-1103, May 2013.

[41] A. Urtasun and D. D. Lu, “Control of a Single-Switch Two-Input Buck Converter for MPPT of Two PV Strings,” *IEEE Trans Ind Electron*, vol. 62, no. 11, pp. 7051-7060, Nov. 2015.

[42] A. F. Murtaza, M. Bilal, R. Ahmad, and H. A. Sher, “A Circuit Analysis-Based Fault Finding Algorithm for Photovoltaic Array Under L–L/L–G Faults,” *IEEE J Emerg Sel Top. Power Electron*, vol. 8, no. 3, pp. 3067-3076, Sep. 2020.

[43] Y. Hu, “Online Two-Section PV Array Fault Diagnosis With Optimized Voltage Sensor Locations,” *IEEE Trans Ind Electron*, vol. 62, no. 11, pp. 7237-7246, Nov. 2015.

[44] Z. Yi and A. H. Etemadi, “Fault Detection for Photovoltaic Systems Based on Multi-Resolution Signal Decomposition and Fuzzy Inference Systems,” *IEEE Trans Smart Grid*, vol. 8, no. 3, pp. 1274-1283, May 2017.

[45] B.-H. C. K. A. Kim G. S. Seo and P. T. Krein, “Photovoltaic Hot-Spot Detection for Solar Panel Substrings Using AC Parameter Characterization,” *IEEE Trans Power Electron*, vol. 31, no. 2, pp. 1121-1130, Feb. 2016.

[46] S. Yang, K. Itako, T. Kudoh, K. Koh, and Q. Ge, “Monitoring and Suppression of the Typical Hot-Spot Phenomenon Resulting From Low-Resistance Defects in a PV String,” *IEEE J Photovolt*, vol. 8, no. 6, pp. 1809-1817, Nov. 2018.

[47] N. L. Georgijevic, M. V. Jankovic, S. Srdic, and Z. Radakovic, “The Detection of Series Arc Fault in Photovoltaic Systems Based on the Arc Current Entropy,” *IEEE Trans Power Electron*, vol. 31, no. 8, pp. 5917-5930, Aug. 2016.

[48] M. Ahmadi, H. Samet, and T. Ghanbari, “A New Method for Detecting Series Arc Fault in Photovoltaic Systems Based on the Blind-Source Separation,” *IEEE Trans Ind Electron*, vol. 67, no. 6, pp. 5041-5049, Jun. 2020.

[49] M. Ahmadi, H. Samet, and T. Ghanbari, “Series Arc Fault Detection in Photovoltaic Systems Based on Signal-to-Noise Ratio Characteristics Using Cross-Correlation Function,” *IEEE Trans*

Ind Inf., vol. 16, no. 5, pp. 3198-3209, May 2020.

[50] Y. Zhao, R. Ball, J. Mosesian, J. Palma, and B. Lehman, “Graph-Based Semi-supervised Learning for Fault Detection and Classification in Solar Photovoltaic Arrays,” *IEEE Trans Power Electron*, vol. 30, no. 5, pp. 2848-2858, May 2015.

[51] M. S. Agamy, M. Harfman-Todorovic, and A. Elasser, “Ground fault and insulation degradation detection and localization in PV plants,” *2013 IEEE 39th Photovoltaic Specialists Conference (PVSC*, 2013, pp. 2840–2844.

[52] F. Grimaccia, S. Leva, A. Dolara, and M. Aghaei, “Survey on PV Modules’ Common Faults After an O&M Flight Extensive Campaign Over Different Plants in Italy,” *IEEE J Photovolt.*, vol. 7, no. 3, pp. 810-816, May 2017.

[53] M. K. Alam, F. Khan, J. Johnson, and J. Flicker, “A comprehensive review of catastrophic faults in PV arrays: Types, detection, and mitigation techniques,” *IEEE J Photovolt*, vol. 5, no. 3, pp. 982-997, May 2015.

[54] R. Araneo, M. Maccioni, S. Lauria, and S. Celozzi, “Analysis of the lightning transient response of the earthing system of large-scale groundmounted PV plants,” in *Proc. IEEE Manchester PowerTech*, Manchester, U.K, 2017, pp. 1–6.

[55] I. U. Khalil, “Comparative Analysis of Photovoltaic Faults and Performance Evaluation of its Detection Techniques,” *IEEE Access*, vol. 8, pp. 26676-26700, 2020.

[56] S. A. Saleh, A. S. Aljankawey, B. Alsayid, and M. S. Abu-Khaizaran, “Influences of power electronic converters on voltage–current behaviors during faults in DGUs—Part II: Photovoltaic systems,” *IEEE Trans Ind Appl*, vol. 51, no. 4, pp. 2832-2845, Aug. 2015.

[57] C. Kuo, J. Chen, S. Chen, C. Kao, H. Yau, and C. Lin, “Photovoltaic Energy Conversion System Fault Detection Using Fractional-Order Color Relation Classifier in Microdistribution Systems,” *IEEE Trans Smart Grid*, vol. 8, no. 3, pp. 1163-1172, May 2017.

[58] B. P. Kumar, D. S. Pillai, N. Rajasekar, M. Chakkarapani, and G. S. Ilango, “Identification and Localization of Array Faults With Optimized Placement of Voltage Sensors in a PV System,” *IEEE Trans Ind Electron*, vol. 68, no. 7, pp. 5921-5931, Jul. 2021.

[59] S. Roy, M. K. Alam, F. Khan, J. Johnson, and J. Flicker, “An Irradiance-Independent, Robust Ground-Fault Detection Scheme for PV Arrays Based on Spread Spectrum Time-Domain Reflectometry (SSTDR,” *IEEE Trans Power Electron*, vol. 33, no. 8, pp. 7046-7057, Aug. 2018.

[60] M. K. Alam, F. Khan, J. Johnson, and J. Flicker, “PV ground-fault detection using spread spectrum time domain reflectometry (SSTDR,” in *Proc. IEEE Energy Convers. Congr*, Denver, CO, USA, 2013, pp. 1015–1020.

[61] K. A. Saleh, A. Hooshyar, E. F. El-Saadany, and H. H. Zeineldin, “Voltage-Based Protection Scheme for Faults Within Utility-Scale Photovoltaic Arrays,” *IEEE Trans Smart Grid*, vol. 9, no. 5, pp. 4367-4382, Sep. 2018.

[62] L. Zhou, F. Gao, and T. Xu, “A Family of Neutral-Point-Clamped Circuits of Single-Phase PV Inverters: Generalized Principle and Implementation,” *IEEE Trans Power Electron*, vol. 32, no. 6, pp. 4307-4319, Jun. 2017.

[63] Y. Yang, F. Blaabjerg, and H. Wang, “Low-voltage ride-through of single-phase transformerless photovoltaic inverters,” *IEEE Trans Ind Appl*, vol. 50, no. 3, pp. 1942-1952, 2014.

[64] A. A. Khan, U. A. Khan, H. F. Ahmed, H. Cha, and S. Ahmed, “Improved NPC Inverters without Short-Circuit and Dead-Time Issues,” *IEEE Trans Power Electron*, vol. 37, no. 2, pp. 2180-2190, Feb. 2022.

[65] L. Ma, T. Kerekes, P. Rodriguez, X. Jin, R. Teodorescu, and M. Liserre, “A new PWM strategy for grid-connected half-bridge active NPC converters with losses distribution balancing mechanism,” *IEEE Trans Power Electron*, vol. 30, no. 9, pp. 5331-5340, Sep. 2015.

[66] H. Xiao and S. Xie, “Leakage current analytical model and application in single-phase transformerless photovoltaic grid-connected inverter,” *IEEE Trans Electromagn Compat*, vol. 52, no. 4, pp. 902-913, Nov. 2010.

[67] X. Xing, C. Zhang, A. Chen, H. Geng, and C. Qin, “Deadbeat Control Strategy for Circulating Current Suppression in Multiparalleled Three-Level Inverters,” *IEEE Trans Ind Electron*, vol. 65, no. 8, pp. 6239-6249, Aug. 2018.

[68] T. Liu, A. Chen, and Y. Huang, “Multi-Vector Model Predictive Current Control for Paralleled Three-Level T-Type Inverters With Circulating Current Elimination,” *IEEE Trans Ind Electron*, Aug. 2022.

[69] X. Xing, Z. Zhang, C. Zhang, J. He, and A. Chen, “Space Vector Modulation for Circulating Current Suppression Using Deadbeat Control Strategy in Parallel Three-Level Neutral-Clamped Inverters,” *IEEE Trans Ind Electron*, vol. 64, no. 2, pp. 977-987, Feb. 2017.

[70] K. Sun, X. Lin, Y. Li, Y. Gao, and L. Zhang, “Improved Modulation Mechanism of Parallel-Operated T-Type Three-Level PWM Rectifiers for Neutral-Point Potential Balancing and Circulating Current Suppression,” *IEEE Trans Power Electron*, vol. 33, no. 9, pp. 7466-7479, Sep. 2018.

[71] T. Jin, Y. Huang, Y. Lin, and M. N. D. Legrand, “Model predictive current control based on virtual voltage vector method for parallel three-level inverters,” *IEEE J Emerg Sel Top Power Electron*, vol. 9, no. 5, pp. 6049-6058, Oct. 2021.

[72] Z. Shao, X. Zhang, F. Wang, and R. Cao, “Modeling and elimination of zero-sequence circulating currents in parallel three-level T-type grid-connected inverters,” *IEEE Trans Power Electron*, vol. 30, no. 2, pp. 1050-1063, Feb. 2015.

[73] A. Chen, Z. Zhang, X. Xing, K. Li, C. Du, and C. Zhang, “Modeling and suppression of circulating currents for multi-paralleled three-level T-type inverters,” *IEEE Trans Ind Appl*, vol. 55, no. 4, pp. 3978-3988, Jul. 2019.

[74] C. B. Jacobina, E. C. D. Santos, N. Rocha, and E. L. L. Fabrício, “Single-phase to three-phase drive system using two parallel single-phase rectifiers,” *IEEE Trans Power Electron*, vol. 25, no. 5, pp. 1285-1295, 2010.

[75] C. B. Jacobina, E. C. D. Santos, B. D. S. Gouveia, and E. R. C. Silva, “Reversible ac drive systems based on parallel ac-ac dc-link converters,” *Conf Rec - IAS Annu Meet IEEE Ind Appl Soc*, 2008.

[76] E. C. D. Santos, N. Rocha, and C. B. Jacobina, “Suitable single-phase to three-phase AC-DC-AC power conversion system,” *IEEE Trans Power Electron*, vol. 30, no. 2, pp. 860-870, Feb. 2015.

[77] H. Cai, R. Zhao, and H. Yang, “Study on ideal operation status of parallel inverters,” *IEEE Trans Power Electron*, vol. 23, no. 6, pp. 2964-2969, 2008.

[78] Y. H. Liao, H. C. Chen, H. C. Cheng, Y. L. Ke, and Y. T. Li, “A novel control strategy of circulating currents in paralleled single-phase boost converters with different power sharing for microgrid applications,” *IEEE Trans Ind Appl*, vol. 50, no. 2, pp. 1304-1312, 2014.

[79] Y. H. Liao and H. C. Chen, “Simplified PWM with Switching Constraint Method to Prevent Circulating Currents for Paralleled Bidirectional AC/DC Converters in Grid-Tied System Using Graphic Analysis,” *IEEE Trans Ind Electron*, vol. 62, no. 7, pp. 4573-4586, Jul. 2015.

[80] C. Zhang, Z. Wang, X. Xing, X. Li, and X. Liu, "Modeling and Suppression of Circulating Currents Among Parallel Single-Phase Three-Level Grid-Tied Inverters," *IEEE Trans Ind Electron*, vol. 69, no. 12, pp. 12967-12979, Dec. 2022.

[81] J. M. Guerrero, J. C. Vasquez, J. Matas, L. G. Vicuña, and M. Castilla, "Hierarchical control of droop-controlled AC and DC microgrids - A general approach toward standardization," *IEEE Trans Ind Electron*, vol. 58, no. 1, pp. 158-172, Jan. 2011.

[82] Q. Yang, L. Jiang, H. Zhao, and H. Zeng, "Autonomous voltage regulation and current sharing in islanded multi-inverter DC Microgrid," *IEEE Trans Smart Grid*, vol. 9, no. 6, pp. 6429-6437, Nov. 2018.

[83] S. Anand, B. G. Fernandes, and J. M. Guerrero, "Distributed control to ensure proportional load sharing and improve voltage regulation in low-voltage DC microgrids," *IEEE Trans Power Electron*, vol. 28, no. 4, pp. 1900-1913, Apr. 2013.

[84] A. Tah and D. Das, "An Enhanced Droop Control Method for Accurate Load Sharing and Voltage Improvement of Isolated and Interconnected DC Microgrids," *IEEE Trans Sustain Energy*, vol. 7, no. 3, pp. 1194-1204, Jul. 2016.

[85] M. Saleh, Y. Esa, and A. Mohamed, "Impact of Communication Latency on the Bus Voltage of Centrally Controlled DC Microgrids during Islanding," *IEEE Trans Sustain Energy*, vol. 10, no. 4, pp. 1844-1856, Oct. 2019.

[86] L. Meng, T. Dragicevic, J. Roldán-Pérez, J. C. Vasquez, and J. M. Guerrero, "Modeling and Sensitivity Study of Consensus Algorithm-Based Distributed Hierarchical Control for DC Microgrids," *IEEE Trans Smart Grid*, vol. 7, no. 3, pp. 1504-1515, May 2016.

[87] F. Guo, Q. Xu, C. Wen, L. Wang, and P. Wang, "Distributed Secondary Control for Power Allocation and Voltage Restoration in Islanded DC Microgrids," *IEEE Trans Sustain Energy*, vol. 9, no. 4, pp. 1857-1869, Oct. 2018.

[88] L. Xing, "Distributed Secondary Control for Current Sharing and Voltage Restoration in DC Microgrid," *IEEE Trans Smart Grid*, vol. 11, no. 3, pp. 2487-2497, 2020.

[89] S. Sahoo and S. Mishra, "A Distributed Finite-Time Secondary Average Voltage Regulation and Current Sharing Controller for DC Microgrids," *IEEE Trans Smart Grid*, vol. 10, no. 1, pp. 282-292, Jan. 2019.

[90] Y. Li, P. Dong, M. Liu, and G. Yang, "A distributed coordination control based on finite-time consensus algorithm for a cluster of dc microgrids," *IEEE Trans Power Syst*, vol. 34, no. 3, pp. 2205-2215, May 2019.

[91] P. Wang, R. Huang, M. Zaery, W. Wang, and D. Xu, "A Fully Distributed Fixed-Time Secondary Controller for DC Microgrids," *IEEE Trans Ind Appl*, vol. 56, no. 6, pp. 6586-6597, Nov. 2020.

[92] Q. F. Yuan, Y. W. Wang, X. K. Liu, and Y. Lei, "Distributed Fixed-Time Secondary Control for DC Microgrid Via Dynamic Average Consensus," *IEEE Trans Sustain Energy*, vol. 12, no. 4, pp. 2008-2018, Oct. 2021.

[93] J. Zhou, Y. Xu, H. Sun, L. Wang, and M. Y. Chow, "Distributed Event-Triggered H∞ Consensus Based Current Sharing Control of DC Microgrids Considering Uncertainties," *IEEE Trans Ind Inform.*, vol. 16, no. 12, pp. 7413-7425, Dec. 2020.

[94] F. Guo, L. Wang, C. Wen, D. Zhang, and Q. Xu, "Distributed Voltage Restoration and Current Sharing Control in Islanded DC Microgrid Systems without Continuous Communication," *IEEE Trans Ind Electron*, vol. 67, no. 4, pp. 3043-3053, Apr. 2020.

[95] L. Xing, Q. Xu, F. Guo, Z. G. Wu, and M. Liu, "Distributed secondary control for DC microgrid

with event-triggered signal transmissions,” *IEEE Trans Sustain Energy*, vol. 12, no. 3, pp. 1801-1810, Jul. 2021.

[96] J. C. S. I. H. A. Bidram, “Distributed Finite-Time Event-Triggered Frequency and Voltage Control of AC Microgrids,” *IEEE Trans Power Syst*, vol. 37, no. 3, pp. 1979-1994, 2022.

[97] Z. Wang, “Distributed Event-Triggered Fixed-Time Fault-Tolerant Secondary Control of Islanded AC Microgrid,” *IEEE Trans Power Syst*, vol. 37, no. 5, pp. 4078-4093, Jan. 2022.

[98] J. Chai, M. Wang, Y. He, Z. Li, Z. Xu and S. Li, "Decentralized Suppression Strategy of Common Ground Circulating Current Caused by Grounding Fault in PV Modules in Single-Phase PV Grid-Connected Systems," *IEEE J. Emerg. Sel. Topics Circuits Syst.*, vol. 12, no. 1, pp. 220-231, March 2022.

[99] J. L. Chen, C. Kuo, and S. Chen, “DC-side fault detection for photovoltaic energy conversion system using fractional-order dynamic-error-based fuzzy Petri net integrated with intelligent meters”,” *IET Renew Power Gener*, vol. 10, no. 9, pp. 1318-1327, Dec. 2016.

[100] J. Chai, M. Wang, Z. Xu and K. W. E. Cheng, "Suppression of Circulating Currents Among IPOP Single-Phase Three-Level Inverters," *IEEE Trans. Ind. Electron.*, vol. 71, no. 9, pp. 10533-10545, Sept. 2024.

[101] S. Galeani, L. Menini, and A. Potini, “Robust trajectory tracking for a class of hybrid systems: An internal model principle approach,” *IEEE Trans Autom. Contr*, vol. 57, no. 2, pp. 344-359, Feb. 2012.

[102] J. Chai, X. Lyu, M. Wang and Z. Xu, "Distributed Fixed-Time Secondary Control for DC Microgrid with Less Information Exchange," *8th International Conference on Power and Renewable Energy (ICPRE)*, Shanghai, China, 2023, pp. 652-657.

[103] Z. Tu, W. Zhang, and W. Liu, “Deep Reinforcement Learning-Based Optimal Control of DC Shipboard Power Systems for Pulsed Power Load Accommodation,” *IEEE Trans Smart Grid*, vol. 14, no. 1, pp. 29-40, Jan. 2023.

[104] Z. Zuo, “Nonsingular fixed-time consensus tracking for second-order multi-agent networks,” *Automatica*, vol. 54, pp. 305-309, Apr. 2015.

[105] A. Polyakov, “Nonlinear feedback design for fixed-time stabilization of linear control systems,” *IEEE Trans Autom. Contr*, vol. 57, no. 8, pp. 2106-2110, 2012.

[106] R. Olfati-Saber and R. M. Murray, “Consensus problems in networks of agents with switching topology and time-delays,” *IEEE Trans Autom Control*, vol. 49, no. 9, pp. 1520-1533, Sep. 2004.

[107] A. Polyakov, “Nonlinear feedback design for fixed-time stabilization of linear control systems,” *IEEE Trans Autom. Contr*, vol. 57, no. 8, pp. 2106-2110, 2012.

[108] J. Chai, M. Wang and Z. Xu, "A Distributed Event-Triggered Fixed-Time Secondary Control for DC Microgrids Without Continuous Signal Transmission," *IEEE Journal of Emerging and Selected Topics in Power Electronics*, doi: 10.1109/JESTPE.2024.3435755.

[109] J. Lu, X. Zhang, B. Zhang, X. Hou and P. Wang, "Distributed Dynamic Event-Triggered Control for Voltage Restoration and Current Sharing in DC Microgrids," *IEEE Trans Sustain Energy*, vol. 13, no. 1, pp. 619-628, Jan. 2022.